

UNIVERSITY OF STUTTGART
INSTITUTE OF AIRCRAFT DESIGN

Master Thesis

Academic Year 2009-2010

Muhammad Rehan Nasib

**Testing and Numerical Prediction of
Failure in Aluminium Alloy Sheet Metal**

Supervisor: Dr. A.K. Pickett

Acknowledgements

This Master thesis is presented in the fulfillment of the requirement for the degree of Master of Science. The research presented in this Master thesis was initiated by Dr. A. K. Pickett at the Institute of Aircraft Design (Institut für Flugzeugbau) at the University of Stuttgart.

I would especially like to express my deepest thankfulness and admiration to Dr. A. K. Pickett for his support and guidance throughout the course of this project. His invaluable advice, guidance and enthusiasm have been great inspiration for me.

A special thanks to Dipl.-Ing. Sebastian Fischer. It was with his cooperation and guidance that the experimental study was conducted at the composites laboratory. Many thanks to the staff of the workshop for preparing test specimens.

Finally, I would like to thank my parents and family members for their emotional and moral support throughout my academic career. They have always been a constant source of inspiration and encouragement for me.

Abstract

The introduction of aluminium alloy in the automotive industry helped automotive manufactures to produce fuel efficient and environment friendly vehicles. This has been only possible because of aluminium alloy certain material properties which reduce weight of the vehicle structure without compromising strength. Much lighter vehicles are produced these days by using aluminum alloy within the frame and body parts than was previously possible with steel. It has also become important for automotive manufactures to improve the crashworthiness of the vehicles to ensure passenger and pedestrian safety. During manufacturing of aluminium body panels different defects are developed which are critical for crashworthiness of vehicle. To investigate how these aluminium alloy body panels behave during crash, different crash tests are done.

In order to avoid expensive crash testing of aluminium alloy body panels a valid simulation and predictive failure model of material is required. The aim of this research study is to use numerical simulations in combination with experimental investigations for prediction of failure and crack development in aluminium alloy sheet. The experimental investigation of different notch specimens helped in generating set of test data. These experimental findings are verified by means of Finite Element analysis. Micro-mechanical failure models are used to develop numerical simulations which are analyzed using explicit Finite Element code PAM-CRASH™. Numerical simulation results are compared with experimental findings in order to validate micro-mechanical failure models.

Table of Contents

List of Figures.....	vii
Chapter 1 : Introduction	1
1.1 Background:	1
1.2 Benefits of using aluminium alloys in Automotive Industry.	2
1.3 Applications of aluminium alloys in vehicles	3
1.4 Aluminium sheet forming	4
Chapter 2 : Aims and Objectives.....	5
Chapter 3 : Literature Review.....	6
3.1 Metal forming	6
3.1.1 Sheet metal forming Processes	6
3.1.2 Deep drawing.....	7
3.1.3 Bending.....	7
3.1.4 Punching and Blanking.....	7
3.2 Mechanics of sheet metal forming.....	8
3.2.1 Anisotropy.....	9
3.2.2 Isotropic yielding criteria.....	9
3.2.3 Plastic anisotropic yielding criteria.....	11
3.2.4 Work hardening hypothesis	13
3.2.5 Forming limit diagram (FLD).....	14
3.3 Fracture mechanics	16
3.3.1 Linear elastic fracture mechanics (LEFM)	17
3.3.2 Modes of loading	18
3.3.3 Deformation and fracture of metals	18

3.4	Mathematical models	20
3.4.1	The Gurson model.....	20
3.4.2	The Gologanu damage model	22
3.4.3	The Lemaitre ductile damage model.....	22
3.4.4	Wilkins fracture model	23
3.4.5	Implementation in numerical simulation	25
3.5	Overview of explicit and implicit finite element methods.....	26
Chapter 4 : Experimental Investigation		29
4.1	Preparation of specimens	29
4.2	Test procedure.....	32
4.3	Optical strain measurement.....	33
4.4	Test procedure.....	34
Chapter 5 : Finite Element Model.....		36
5.1	Model formulation	36
5.1.1	Geometric model.....	36
5.1.2	Assumptions.....	37
5.1.3	Material properties	37
5.1.4	Boundary conditions	37
5.2.5	Loading conditions.....	38
Chapter 6 : Finite Element Analysis and Simulation		39
6.1	Shell elements simulation	39
6.1.1	Methodology	39
6.1.2	Mesh size	40
6.1.3	Boundary Conditions	41
6.1.4	Shell material card	41

6.2 Simulation results.....	44
6.2.1 Notched specimens	46
6.2.2 Holes in plate specimen	52
6.3 Solid element simulation.....	54
6.3.1 Methodology	54
6.3.2 Mesh size and boundary conditions	55
6.3.3 Solid material card	56
6.3.4 True stress-strain curve	60
6.4 Solid element simulation results	61
6.4.1 Notched specimens	63
6.4.2 Holes in plate	67
6.5 Discussion of results:	69
Chapter 7 : Conclusion.....	72
7.1 Scope for future work	73
Chapter 8 : References	75
Appendix 1.....	78
Appendix 2.....	79

List of Figures

Figure 1.1: Resistance forces acting on the vehicle [2].	2
Figure 1.2: Audi A8–spaceframe and semi materials [3].	4
Figure 3.1: Types of forming processes [4].	6
Figure 3.2: Forming limit diagram for plane stress.	14
Figure 3.3: The three modes of loading.	18
Figure 3.4: Fracture due to inclusion and coalescence of voids.	19
Figure 3.5: The continuum assumption for modeling porous medium.	20
Figure 3.6: Spring-mass system.	26
Figure 4.1: Tensile testing machine and U-notched tested specimens	33
Figure 4.2: Test specimens coated with white and black paint.	34
Figure 4.3: Experimental setup of optical strain measurement.	35
Figure 5.1: Boundary and loading conditions used in the FE model.	38
Figure 6.1: Full model of the Parallel specimen.	40
Figure 6.2: Shell elements mesh size for Parallel specimen.	40
Figure 6.3: Boundary conditions for Parallel specimen.	41
Figure 6.4: Forming limit diagram used as failure criterion.	43
Figure 6.5: Shell element material card.	44
Figure 6.6: Comparison of the simulation with the experimental results for the parallel	45
Figure 6.7: Figures of max plastic strain and max Von-Mises stress in parallel specimen	45
Figure 6.8: Comparison of the simulation with the experimental results for 1mm	46
Figure 6.9: Figures of max plastic strain and max Von-Mises stress in the 1mm slit	46
Figure 6.10: Comparison of the simulation with the experimental results for	47

Figure 6.11: Figures of max plastic strain and max Von Mises-stress in the 4mm diameter.....	47
Figure 6.12: Comparison of the simulation with the experimental results for	48
Figure 6.13: Figures of max plastic strain and max Von-Mises stress in the 8mm.....	48
Figure 6.14: Comparison of the simulation with the experimental results for	49
Figure 6.15: Figures of max plastic strain and max Von-Mises stress of.....	49
Figure 6.16: Comparison of the simulation with the experimental results for the	50
Figure 6.17: Figures of max plastic strain and max Von-Mises stress of V-notch.....	50
Figure 6.18: Comparison of the simulation with the experimental results for the	51
Figure 6.19: Figures of max plastic strain and max Von-Mises stress of the offset 42mm.....	51
Figure 6.20: Comparison of the simulation with the experimental results for the	52
Figure 6.21: Figures of max plastic strain and max Von-Mises stress of hole in plate specimen	52
Figure 6.22: Comparison of the simulation with the experimental results for the	53
Figure 6.23: Figures of max plastic strain and max Von-Mises stress of hole in plate	53
Figure 6.24: Solid elements with nodes and local coordinates system [22]......	54
Figure 6.25: Isometric and front view of the half solid and half shell elements.....	55
Figure 6.26: Boundary conditions of solid element model and parametric view.	56
Figure 6.27: EWK solid element material card	58
Figure 6.28: Relationship between damage function (failure criteria).	59
Figure 6.29: Elastic-plastic solid element material card.....	60
Figure 6.30: True stress-strain curve obtained from optical strain testing.	61
Figure 6.31: Comparison of the simulation solid element with the experimental results.....	62
Figure 6.32: Figures of max plastic strain and max Von-Mises stress in parallel specimen.....	63
Figure 6.33: Comparison of the simulation with the experimental results for 1mm	63

Figure 6.34: Figures of max plastic strain and max Von-Mises stress in 1mm dia-slit specimen	63
Figure 6.35: Comparison of the simulation with the experimental results for 4mm	64
Figure 6.36: Figures of max plastic strain and max Von-Mises stress in	64
Figure 6.37: Comparison of the simulation with the experimental results for 8mm	65
Figure 6.38: Figures of max plastic strain and max Von-Mises stress in the	65
Figure 6.39: Comparison of the simulation with the experimental results for offset	66
Figure 6.40: Figures of max plastic strain and max Von-Mises stress in the	66
Figure 6.41: Comparison of the simulation with the experimental results for the 16 mm	67
Figure 6.42: Figures of max plastic strain and max Von-Mises stress in	67
Figure 6.43: Comparison of the simulation with the experimental results for the 32 mm	68
Figure 6.44: Figures of max plastic strain and max Von-Mises stress in the	68
Figure 6.45: Diffuse and localized necking	69
Figure A1.0.1: True stress-strain curve	78

Chapter 1 : Introduction

1.1 Background:

Aluminium alloy is known for its low weight, corrosion resistance and good formability, due to these properties, it has for many years been indispensable in the aerospace industry. With the advancement in technology and realization of its great versatility and unique properties, aluminium has become material choice for many industries. It is now used in the production of cars, buses, trains, ships and bicycles.

The increasing demand in fossil fuels and rapidly depleting world oil resources has led to higher fuel prices. This has triggered the need to develop more fuel efficient and environmentally cleaner means of transport. Automotive manufactures in collaboration with other industries are developing new technologies in order to meet customer demand for fuel efficiency, improved safety, comfort and strict environmental legislation.

The above mentioned customer and environmental targets are achieved by introducing alternative fuels, replacing the traditional gasoline engine with hybrid propulsion system and reducing the curb weight of the vehicle to improve fuel consumption. The steadily growing interest in aluminum alloys in vehicles is connected with the unique set of their properties, predominately light weight. It is used for single parts or chassis parts, and has been used for entire aluminum alloy body structures. The use of aluminium in the structure of automobiles is hindered by two factors; namely, the high cost of aluminium alloys which is twice that of steel, and the difficulties in manufacturing car bodies under the conditions of modern large-scale production. However, the efficiency of a structure should not be evaluated only in terms of the cost of the material without taking into account other means that provide this efficiency, i.e., organizational, operational, manufacturing, and design ones. With the reduced weight of the vehicle, the higher cost is offset by the significant saving in terms of fuel costs over the life time of the vehicle [1].

Studies have been conducted and shown that aluminium alloy offers greater recycling possibilities with 95% of the material being recoverable. It requires only 5% of the total energy

to recycle aluminium than to produce the primary metal. Furthermore the quality of the recycled aluminium is not lost during this process.

1.2 Benefits of using aluminium alloys in Automotive Industry.

Weight reduction directly reduces the energy consumption because the energy required to drive a vehicle is, except for aerodynamic resistance, directly proportional to its mass. The effect of mass on the different resistance forces is illustrated in the following figure.

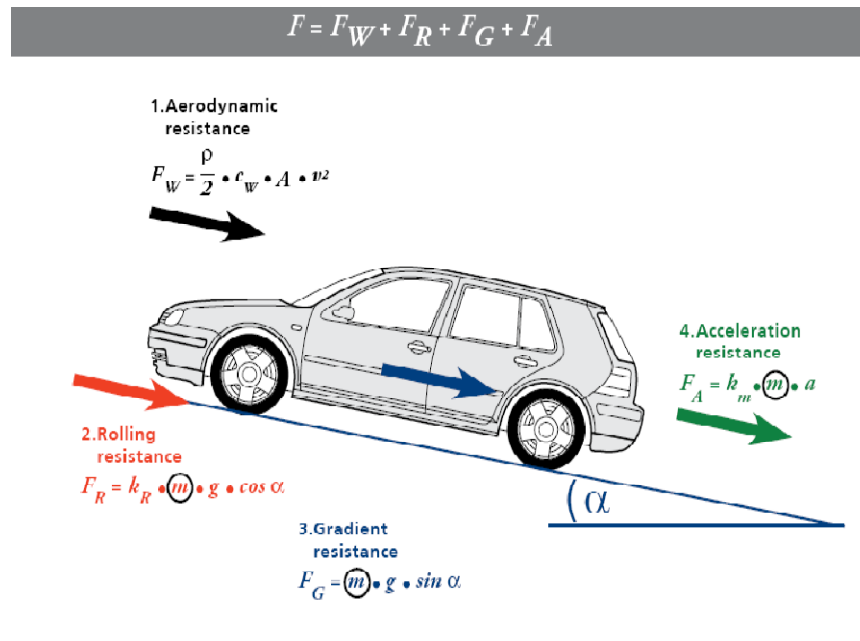


Figure 1.1: Resistance forces acting on the vehicle [2].

On average with 100kg mass reduction on the passenger vehicle saves 0.35 liters of fuel per 100km and 9 grams of CO₂ per km at the exhaust of the vehicle. It is estimated that by using light weight materials up to 300kg of weight can be reduced in a medium size vehicle. Thus during the total life period of the vehicle (150,000km) about 1600 liters of fuel can be saved. Weight reduction also improves the acceleration of the vehicle, as it is influenced by power-to-weight ratio. Keeping braking power constant, light-weighting shortens braking distance.

Road handling is improved by reducing weight in many different ways; for instance, handling of lighter vehicle is easy in critical situations and reducing body weight lowers the centre of gravity improving the vehicle's stability and reducing the risk of roll-over. The optimal

weight distribution between front and rear axle being 50:50 but the front axle being usually overloaded, using lightweight aluminium components for the front parts of cars is particularly beneficial. Saving weight on unsuspended parts like wheels increases driving comfort [2].

1.3 Applications of aluminium alloys in vehicles

Today, aluminium has become the material of choice for many automotive applications such as chassis, engine block, auto-body and many structural components. Different alloys are customized by variation in the chemical composition and processing to best fit the desired application. Studies show that the highest volumes of components in vehicles are casting, such as engine blocks, cylinder heads, and chassis parts. Non-heat treated aluminium-magnesium alloys gives excellent protection against inter crystalline corrosion and high strength, becoming continuous substitution of cast iron engine blocks. Another wide field of aluminium solutions and applications is opened by making use of the well established technology of aluminium extrusions. Examples are; chassis parts, bumper beams, and air bags housing.

Aluminium sheet for automobile body application have been used since the early days of car and aluminium production. But due to mass production and low cost priorities, steel has taken the lead. But increasing fuel prices, CO₂ regulations and additional comfort and equipment loads has lead to a revival of aluminium alloy for body panels. The two main types of aluminium alloy classes used in sheet application are non heat treatable Al-Mg alloy and the heat treatable Al-Mg-Si alloy. Both alloys are used in abundance depending upon the application, but Al-Mg-Si alloys are being used worldwide because the requirements for the material properties now include not only strength and formability, but also corrosion resistance, hemming formability, surface characteristics and weldability.

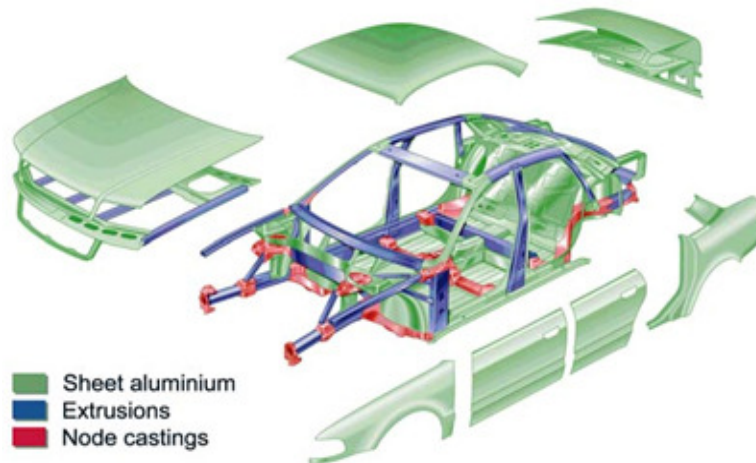


Figure 1.2: Audi A8–spaceframe and semi materials [3].

1.4 Aluminium sheet forming

Aluminium alloy sheets are generally less formable than steel because of their lower strain to failure. Similar to metals, wrinkling, cracking and spring back of aluminium alloy sheets occur during forming process. When compared to steel sheets, aluminum alloy sheets exhibit proof stress and tensile strengths almost equivalent to those of mild-steel, however, their elongations are usually smaller.

The major problem with aluminium alloy sheets has been difficulty of using traditional forming techniques used for making steel sheets. Steps have been taken to improve the formability issues related to stretchability, drawing formability and wrinkling sensitivity of aluminium alloy sheets, for instance hot-blow forming, low temperature forming and using solid lubricants during press forming.

Defects that are inherited during the forming process of aluminium alloy panels, degrade the ability of the panels to absorb kinetic energy during crash. Notches and cracks are source of local deformation which may result in the fracture of aluminium panels.

Chapter 2 : Aims and Objectives

Following are the aims and scope of the project:

- Studying and reviewing of literature relevant to the project. Brief explanation of theories and concepts involved in the project.
- Performing and investigation of tensile test of the series of aluminium alloy test specimens with defects. This includes specimens with u-notches, v-notches and plates with offset holes.
- Experimental evaluation of stress-strain curves for the specimens using an optical strain measurement technique.
- Creation of CAD geometry of the test specimens and pre-processing to generate a series of meshes to represent the exact geometry.
- Use of different meshing elements; shell and solid elements.
- Creation of Finite element model. Investigation of required boundary conditions to simulate testing conditions.
- Forming limit diagram failure criteria to be used for shell elements (FE models).
- Different damage models to be investigated for solid elements (FE models).
- Comparison of shell elements and solid elements results.
- Conclusions and recommendations

Chapter 3 : Literature Review

3.1 Metal forming

Two prominent methods of converting raw material into a product have been metal forming and machining. Metal forming involves changing the shape of the material by permanent plastic deformation. Metal forming is the process of plastically deforming the raw material into product form. It is broadly classified into two classes; namely bulk metal forming and sheet metal forming.

3.1.1 Sheet metal forming Processes

In the bulk metal forming processes the work-piece usually has a high volume to surface area ratio. Examples of such processes are rolling, wire drawing, extrusion, forging and others. On the other hand in sheet metal forming processes the work-piece sheet usually has a low volume to surface area ratio. The sheets usually have a thickness less than 6 mm. In sheet metal working, the change in thickness during plastic deformation is not desirable. Examples of sheet metal forming processes are drawing, deep drawing, stretch forming, bending, spinning etc. The following tabular figure illustrates the vast branches of forming. A few of the many forming process are briefly explained below.

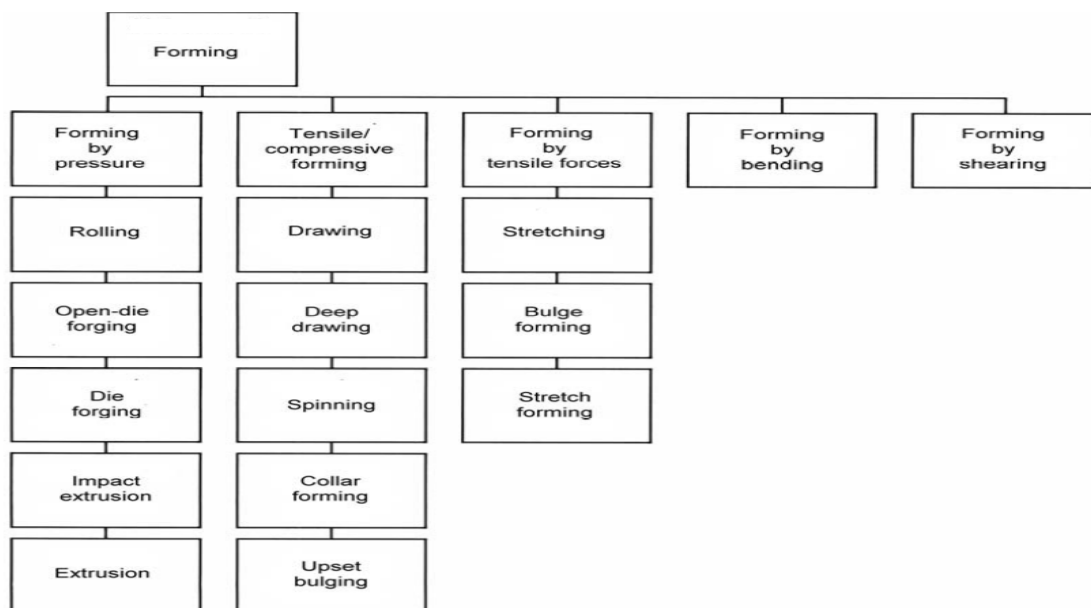


Figure 3.1: Types of forming processes [4].

3.1.2 Deep drawing

In the deep drawing process, a flat sheet metal blank is formed into a cylindrical or box-shaped part by means of a punch, which presses the blank into a die cavity. The blank is held in place with a blank-holder or a hold-down ring with a certain force. When the punch moves down, the portion beneath the blank holder is subjected to radial tensile stresses. These radial tensile stresses lead to compressive hoop stresses in that portion. Thus, the portion beneath the blank holder elongates in the radial direction and compresses in the hoop direction.

Compression in the hoop direction may cause wrinkling of the flange during drawing. To avoid this, the blank-holder should apply a sufficient amount of holding pressure. If precise control of the thickness is desired, the clearance between the punch and die should be less than the thickness. Anisotropy plays an important role in the performance of deep drawing processes.

3.1.3 Bending

Bending is the process by which a straight length is transformed to a curved length. Bending of sheets is called 'sheet bending', whereas bending of tubes is called 'tube bending'. During bending the inner fibers are subjected to compressive strain and the outer fibers are subjected to tensile strain. In between, there are fibers, which have zero strain. The fibers of zero strain in the plane of bending are called the neutral axis. The bendability of a sheet can be improved by heating, applying hydrostatic pressure, or by applying compressive forces in the plane of bending. In bending, proper allowance must be given to the elastic recovery, which follows plastic deformation. This recovery is called 'springback'.

3.1.4 Punching and Blanking

Both punching and blanking are shearing processes. In these processes, a portion of the sheet is removed from the rest of the part by shear. In punching, the objective is to make a hole; therefore, the material which is removed from the sheet is scrap. In blanking, the portion which is removed from the sheet is the desired product. Strictly speaking, the shearing process is not a metal forming process, but is a metal removing process. However, it is different from a dominant class of metal removing processes, i.e., machining, in the sense that the material is not removed in the form of chips [4].

3.2 Mechanics of sheet metal forming

Sheet metal parts are produced in large quantities using special tooling and high-volume production techniques. Most processes are tensile in nature and deformation in one stage is limited by the onset of tensile instability, necking and tearing. Because of the compressive stress in some part of thin sheet membrane, wrinkling and buckling may also occur. This makes very important to understand the mechanics of the forming process, knowledge of failure analysis and considerable experience in manufacturing.

A common feature of many sheet forming processes is that the stress perpendicular to surface of the sheet is less, compared to the stresses in the plane of the sheet (membrane stress). By making assumption that normal stress is zero, plane stress deformation and theory of yielding is developed. There are some cases in which through thickness or normal stress cannot be neglected, and then the theory of yield in three dimensions is required. Various phenomena, affect the strength of the formed sheet metal part due to large deformation with time. These are briefly described below:

- *Strain hardening* In most metals, plastic deformation at room temperature causes an increase in strength known as strain or work-hardening. The hardening rate tends to be higher in soft materials and diminishes as the material becomes stronger. Tensile instability is controlled mainly by the strain-hardening behavior of the sheet metal. So the most important phenomenon in studying sheet metal processes is strain-hardening.
- *Recovery and recrystallization* Material that have been strengthened by strain-hardening, may be softened by heating to a temperature high enough to cause recrystallization, or by holding the material at a temperature below recrystallization for sufficient time for recovery annealing.
- *Ageing* Certain materials harden with time in the absence of deformation. Ageing takes several forms, sometimes influencing only the stress level at which the elastic to plastic transition occurs and in other materials changing their whole response to flow.
- *Damage* Plastic flow implies deformation without loss of integrity or strength. In real material this is not always achieved and when material elements deform under a

positive or tensile hydrostatic stress state, damage processes occur within the structure that eventually lead to a serious loss in strength.

3.2.1 Anisotropy

Material in which the same properties are measured in any direction is termed isotropic, but most industrial sheets show a difference in properties measured in test-pieces aligned, for example, with the rolling, transverse and 45 ° directions of the coil. This variation is known as planar anisotropy. In addition, there can be a difference between the average of properties in the plane of the sheet and those in the through-thickness direction. Two important types of anisotropic materials are

- *Transversal isotropic* Those materials are called transversally isotropic where the rotation of the material about a line does not change the properties of the material. The plane that is perpendicular to this line is called the plane of isotropy.
- *Orthotropic* These materials have three orthogonal planes of elastic symmetry and are defined by nine independent moduli.

3.2.2 Isotropic yielding criteria

The stresses required to yield a material element under plane stress will depend on the current hardness or strength of the sheet and the stress ratio α . The usual way to define the strength of the sheet is in terms of the current flow stress σ_f . The stress ratio α and strain ratio β for plane stress conditions are given by:

$$\varepsilon_1; \quad \varepsilon_2 = \beta \varepsilon_1; \quad \varepsilon_3 = -(1 + \beta) \varepsilon_1 ; \quad (3.1)$$

$$\sigma_1; \quad \sigma_2 = \alpha \sigma_1; \quad \sigma_3 = 0 ;$$

The constant volume condition is used to obtain the third principal strain, giving the condition the sum of the natural strains is zero.

$$\varepsilon_1 + \varepsilon_2 + \varepsilon_3 = 0 \quad (3.2)$$

The flow stress is the stress at which the material would yield in simple tension, i.e. if $\alpha = 0$. So the σ_f depends on the deformation to which the element has been subjected and will change

during the process. Most common yield theories are developed for the knowledge of plastic deformation in metals. Metals are polycrystalline and plastic flow occurs by slip on crystal lattice planes when shear stress reaches a critical value. So the slip associated with dislocations in the lattice is not influenced by normal stress on the slip plane. Yielding will only be anticipated by the shear stress not the average stress or pressure. Considering the single crystal lattice element, the three maximum shear stresses for the element are given by:

$$\tau_1 = \frac{\sigma_1 - \sigma_2}{2}; \quad \tau_2 = \frac{\sigma_2 - \sigma_3}{2}; \quad \tau_3 = \frac{\sigma_3 - \sigma_1}{2} \quad (3.3)$$

As discussed, yield would be dependent on the shear stresses in an element and the current value of the flow stress, yield condition can be expressed as:

$$f(\tau_1, \tau_2, \tau_3) = \sigma_f$$

1. Tresca yield criterion

This hypothesis states that the yielding would occur when the greatest maximum shear stress reaches a critical value. In simple tensile test the maximum shear stress has the value $\tau_{crit} = \sigma_f/2$, so yielding in any process becomes:

$$\frac{\sigma_{max} - \sigma_{min}}{2} = \frac{\sigma_f}{2}$$

$$|\sigma_{max} - \sigma_{min}| = \sigma_f \quad (3.4)$$

In plane stress σ_1 will be the maximum stress and $\sigma_3 = 0$ is the through thickness stress.

2. Von Mises yield criterion

The other widely used criterion is that the yield will occur when the root-mean square value of the maximum shear stresses reaches a critical value and is called the von Mises yield criterion. This is given by:

$$\sqrt{\frac{\tau_1^2 + \tau_2^2 + \tau_3^2}{3}} = \sqrt{\frac{2(\sigma_f)^2}{3}}$$

or $\sqrt{2(\tau_1^2 + \tau_2^2 + \tau_3^2)} = \sigma_f \quad (3.5)$

Substituting the principle stresses for the maximum shear and using the plane stress condition the yield condition can be written as

$$\sqrt{\sigma_1^2 - \sigma_1\sigma_2 + \sigma_2^2} = (\sqrt{1 - \alpha + \alpha^2})\sigma_1 = \sigma_f \quad (3.6)$$

This equation represents an ellipse in plane stress space.

Both the presented theories are for isotropic material and they provide a reasonable approximation to experimental observations.

3.2.3 Plastic anisotropic yielding criteria

Due to the polycrystalline structure of metals, the crystal grains tend to assume preferred orientation during plastic deformation. These preferred orientations of the grains will induce a direction dependent behavior of the metals leading to anisotropy. The most obvious effect of anisotropy is observed in forming of sheets that are produced by rolling.

Anisotropy in sheets is characterized by the Lankford parameter [6] or anisotropy coefficient R . This is defined as the ratio of width strain to thickness strain and is measured in the simple tension test:

$$R = \frac{\varepsilon_w}{\varepsilon_t} = \frac{\ln \frac{w_1}{w_0}}{\ln \frac{t_1}{t_0}} \quad (3.7)$$

For most metals the value of R changes with longitudinal strain and by convention a longitudinal strain of 20% is used for comparison purposes. As R values changes with orientation of the specimen with respect to the rolling direction, three R -values obtained from the specimen in the rolling direction, transverse, and 45° to it. It is called normal anisotropy.

$$R_n = \frac{R_0 + 2R_{45} + R_{90}}{4} \quad (3.8)$$

Variation of the R -value over the plane of the sheet is described by ΔR , the planar anisotropy coefficient.

$$\Delta R = \frac{R_0 + R_{90} - 2R_{45}}{2} \quad (3.9)$$

1. Hill's yielding criterion

Hill's (1948) yield criterion is the oldest anisotropic flow condition proposed by Hill. This criterion neglects the planar anisotropy and assuming the plane stress condition is justified for the sheet forming process, the criterion reads in the principal stress configuration as;

$$\sqrt{\sigma_1^2 - \frac{2R}{R+1}\sigma_1\sigma_2 + \sigma_2^2} = \sigma_f \quad (3.10)$$

For $R = 1$ the standard von Mises ellipse is obtained. For values larger than 1, the ellipse elongates along the major axis whereas it shrinks along the minor axis. Hence, in the case of biaxial tension or biaxial compression larger relative stresses are necessary to initiate plastic flow. Hill's criterion proves to be accurate for steel; however, for aluminium in particular it fails. Several other so called non-quadratic flow criteria have been developed and are used to model forming of aluminium. Hill's 1979 criterion is one of many non-quadratic criteria;

$$|\sigma_1 + \sigma_2|^m + (2R + 1)|\sigma_1 - \sigma_2|^m = (2R + 1)\sigma_f^m \quad (3.11)$$

where m is in range $1.3 \leq m \leq 2.2$. For $m = 2$ the criterion reduces to Hill 1948

2. Barlat's yielding criterion

The six component Barlat criterion [7] is shown in equation 3.12. In this criterion only three components in the sheet plane are used. It is also suitable to describe the yield function in general three dimensional situations, not just for the plane stress state. In the general case, the criterion requires 9 parameters to be determined.

$$\alpha_1|S_2 - S_3|^m + \alpha_2|S_3 - S_1|^m + \alpha_3|S_1 - S_2|^m = 2\sigma_f \quad (3.12)$$

S_1, S_2, S_3 are three Eigen values of S tensor and $\alpha_1, \alpha_2, \alpha_3$ are calculated via transformation to the principal axes of the S tensor from the known values of $\alpha_{11}, \alpha_{22}, \alpha_{33}$ for principal axes of anisotropy:

$$\begin{bmatrix} S_{11} \\ S_{22} \\ S_{33} \\ S_{12} \\ S_{23} \\ S_{31} \end{bmatrix} = \begin{bmatrix} \frac{c_2 + c_3}{3} & -c_3/3 & -c_2/3 & 0 & 0 & 0 \\ -c_3/3 & \frac{c_3 + c_1}{3} & -c_1/3 & 0 & 0 & 0 \\ -c_2/3 & -c_1/3 & \frac{c_1 + c_2}{3} & 0 & 0 & 0 \\ 0 & 0 & 0 & c_4 & 0 & 0 \\ 0 & 0 & 0 & 0 & c_5 & 0 \\ 0 & 0 & 0 & 0 & 0 & c_6 \end{bmatrix} = \begin{bmatrix} \sigma_{11} \\ \sigma_{22} \\ \sigma_{33} \\ \sigma_{12} \\ \sigma_{23} \\ \sigma_{31} \end{bmatrix} \quad (3.13)$$

The Barlat criterion is able to include a real three dimensional stress state and can be seen as a substantial extension of both the Hill's 1948-criterion and the Hill's 1979-criterion.

3.2.4 Work hardening hypothesis

For isotropic material, no matter what the orientation of the fibers or crystals within the material element is, the response to the applied stress state is the same. Strain hardening is an important material characteristic and has prime importance in sheet metal forming. Strain hardening is also assumed to be isotropic hardening which is not dependent on direction in which material has been worked. At a particular instant in a plane stress process during plastic deformation, the representative stress σ is just equal to the flow stress σ_f for an isotropic material. This gives a general relationship between flow stress and representative strain.

$$\sigma_f = f(\varepsilon) \quad (3.14)$$

The stress-strain curve for any proportional deformation process can be obtained by mechanical test and this curve is used to determine the instantaneous strength at a point. In tensile test, a load extension data is obtained and maybe converted to stress-strain diagram. By applying the true stress and stain equations, a curve can be created which shows hardening of the material beyond the maximum load point. This extrapolation of data can be estimated by empirical relations.

- *Power law*

For annealed material, the sharp increase in flow stress at the start of plastic deformation is represented by following equation.

$$\sigma_f = K\varepsilon^n \quad (3.15)$$

where exponent n is the strain- hardening index and K is a constant.

The curve generated by power law, fits extremely well for the stress-strain curve for many soft materials and the exponent n is a convenient indicator of the rate at which the material harden. The only disadvantage of this law is that at zero strain, it predicts zero stress and an infinite slope to the curve.

- *Krupkowsky hardening function*

This function best fits the pre-strained or cold worked materials is given by

$$\sigma_f = K(\varepsilon_0 + \varepsilon)^n \quad (3.16)$$

The material constant ε_0 has been termed as a pre-strain or offset constant. If the material has been hardened in some prior process, this constant indicates shift in the strain axis. An advantage of this function is that there is sharp initial yield stress given by the equation:

$$(\sigma_f)_0 = K\varepsilon_0^n ; \quad (3.17)$$

3.2.5 Forming limit diagram (FLD)

The forming limit diagram (FLD) consists of a curve in the principal in-plane strain space at which either necking starts or fracture is observed. It is basically a material property. Necking is localized in the tension–compression part and is expected to be diffuse in the tension–tension part. The loading line on the left (dashed line) corresponds to a pure shear deformation, the central vertical line to plane strain tension, and the left dashed line to equi-biaxial tension. Uniaxial simple tension is a loading line between the left dashed and the middle vertical lines.

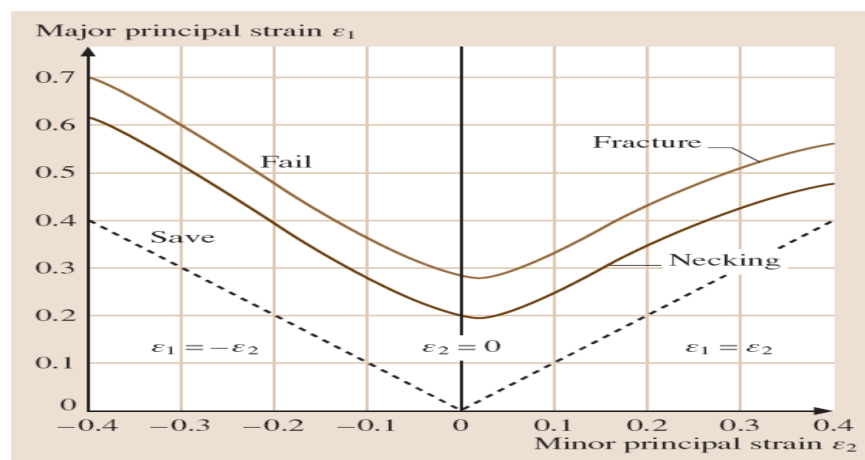


Figure 3.2: Forming limit diagram for plane stress.

The FLD provides an efficient and practical method to assess the formability limits of a sheet metal. It is applied in two different manners.

- *Experimentally* A circular grid pattern is imposed on the sheet either mechanically, photo chemically, or electrochemically. During forming the circles are deformed into ellipses. The principal strains are assumed to be along the major and minor axes of the ellipses. These minor and major radii of the ellipse are measured either manually or automatically by a digital camera. By comparing the measured local strains with the FLD, the range of safety for deep-drawing, the critical zones where necking and/or fracture are most likely to occur, the strain level and the favorable working conditions can be determined, and hence the sheet metal forming process can be improved. In this context a severity index ranging from 0 to 10 is introduced, indicating the distance of the measured strain state from the FLD-curve.
- *Numerically* The analysis of the sheet forming process can be done, for instance, by finite element models a priori to the actual pressing and the computed strains can be compared with the respective FLD and the forming process can be assessed. This application is basic industrial practice today.

FLDs can be measured by various methods such as the uniaxial tensile test using specimens having various dimensions with and without notches, the hydraulic bulge test using elliptical dies, the punch stretching test using strips with various widths and the Marciniak test [8] with hollow punches, etc. Common to all tests is that numerous specimens, or the geometries, have to be used to simulate various principal strain ratios corresponding to various points on the FLD-curve. The experimentally measured FLDs do not completely represent material properties. They depend on various other factors. It is known that the FLD-curve rises with increasing sheet thickness. Furthermore, it has been experimentally noticed that there is strain path dependence of the failure and the grid size used in the experiments effects the measurements. Hence, if a tensile load path (meaning a strain path with positive slope) is followed by a compressive load path (negative slope), the failure strain is lower than the one predicted by the FLD. On the other hand, if a compressive load path is followed by a tensile one, the failure strain is larger than the FLD strain.

3.3 Fracture mechanics

The mechanical design of engineering structures usually involves an analysis of the stress and displacement fields in conjunction with a postulate predicting the event of failure itself. Accurate knowledge of stress states is determined by detailed theoretical analyses of structural geometry and sophisticated methods for determining stress distributions in loaded structures. For complicated structures or loading situations, experimental or numerical methods are preferable. Having performed the stress analysis, a suitable failure criterion is selected, for an assessment of the strength and integrity of the structural component [9].

Load-bearing structures can be classified as ductile or brittle. It is important to note that the material may behave in a ductile or brittle manner, depending on the temperature, rate of loading and other variables. In case of ductile materials, breakage of a structure is preceded by large deformation which occurs over a relatively long time period and may be associated with yielding or plastic flow. The brittle failure, on the other hand, is preceded by small deformation, and is usually sudden. Defects also play a major role in the mechanism of both these types of failure. For ductile failures, which are dominated by yielding before breakage, the important defects (dislocations, grain boundary spacings, interstitial and out-of-size substitutional atoms, precipitates) [9] tend to distort and warp the crystal lattice planes. Brittle fracture, however, which takes place before any appreciable plastic flow occurs, initiates at larger defects such as inclusions, sharp notches, surface scratches or cracks.

The term “fracture mechanics” refers to a vital specialization within solid mechanics in which the presence of a crack is assumed, and quantitative relations between the crack length, the material’s inherent resistance to crack growth and the stress at which the crack propagates are defined [10]. It deals with the behaviour of cracked bodies subjected to stresses and strains. These can arise from primary applied loads or secondary self-equilibrating stress fields. The power of fracture mechanics really lies in the fact that total local crack tip phenomena can, to the first order, be characterized by relatively easily measured global parameters.

In general, fracture mechanics is a set of theories describing the behaviour of solids or structures with geometrical discontinuity at the scale of the structure. The discontinuity features maybe in the form of line discontinuity; in two dimensional media (plates and shells) or surface

discontinuity; in three dimensional media. Fracture mechanics has now evolved into mature discipline of science and engineering. One of the important impacts of fracture mechanics is the establishment of new design philosophy and damage tolerance methodology which have now become an important design criteria in the engineering industries [11].

3.3.1 Linear elastic fracture mechanics (LEFM)

LEFM principles are used to relate the stress magnitude and distribution near crack tip to the remote stresses applied to the crack components, crack size, crack shape and the material properties of the cracked component [12]. The general form of LEFM equation is given as:

$$\sigma_{ij} = \frac{K_I}{\sqrt{2\pi r}} f_{ij}(\theta) + \dots \quad (3.18)$$

where r = distance from the crack tip

K_I = Mode I stress intensity factor (SIF)

$f_{ij}(\theta)$ = function that represents the dependence on θ .

LEFM equation 3.18, shows that a singularity exists at $r = 0$ i.e., when the distance from crack tip is zero, the stresses tends to infinity. As the yield stress is exceeded, material deforms plastically and a plastic zone is formed near the crack tip. The basis of LEFM remains valid if this region of plasticity remains small in relation compared to the overall dimensions of the crack.

The SIF (K) in equation 3.18, defines the magnitude of the local stresses around the crack tip. This factor depends on the loading, crack size and geometry. It can be expressed in a general form given by:

$$K = \sigma \sqrt{\pi a} f\left(\frac{a}{w}\right) \quad (3.19)$$

where σ = remote stress applied to the component

a = crack length

$f(a/w)$ = correction factor that depends on the specimen and crack geometry.

3.3.2 Modes of loading

There are three types of loading modes that a crack can experience and propagates as shown in figure 3.3. These modes are;

- *Mode I* It is called opening mode or tensile mode.
- *Mode II* It corresponds to in-plane shear. The crack face surface tends to slide over each other.
- *Mode III* This mode refers to out-of-plane shear. Here the tearing of two surfaces occurs.

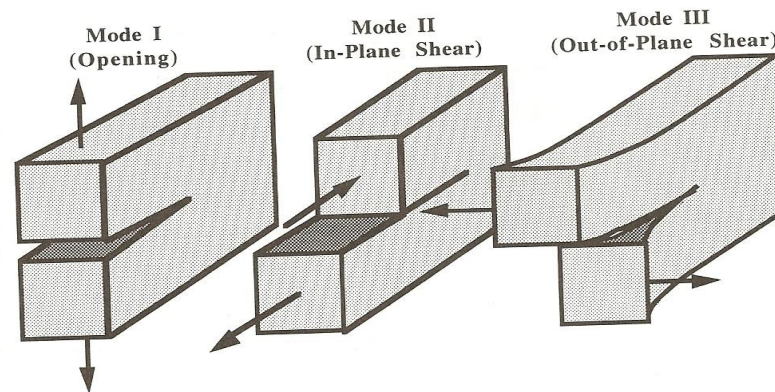


Figure 3.3: The three modes of loading.

In most engineering applications, by far the majority of cracks result from mode I loading. The other two modes often occur in combination with mode I, for instance opening and in-plane shear, or all three modes together. However, if the loading of these modes is in phase, cracks will rapidly choose a direction of growth in which they are subjected to mode I only. Thus, the majority of apparent combined mode cases are reduced to mode I by nature itself, and cracks develop perpendicular to the maximum principal stress.

3.3.3 Deformation and fracture of metals

The microscopic failure mechanism in metals is due to plastic flow accompanied by void nucleation, growth and coalescence of microscopic voids that initiate at inclusions and second phase particles [13]. Metals have polycrystalline micro-structure these crystals are joined with one another along grain boundaries. The grains have anisotropic properties so they differ from

one another also due to segregation, grain boundaries differ from gains. In the microstructure there are defects of different sizes, induced by manufacturing process or inclusion with different material properties. When shear stresses are applied these dislocations start to move and work done during the movement of these dislocations is dissipated as heat. Dislocations movement is restricted at obstacles such as grain boundaries and they stop and start to pile-up at the gain boundaries. Such a pile-up of dislocations is observed as strain hardening with high stress concentration regions [14].

A dislocation pile-up causes not only stress concentrations, it is also a responsible source for the formation of microscopic voids and cavities. The plastic strain and hydro-static stress are responsible for the growth of the individual voids. The coalescence of dislocations leads to the formation and growth of microcavities.

Figure 3.10 illustrates the nucleation, growth and coalescence of micro-voids in ductile metals. A precipitation-hardened aluminium alloy may contain relatively large intermetallic particles, together with a fine dispersion of sub-micron second phase precipitates. These alloys also contain micron-size dispersion particles for grain refinement. Voids form much more readily at the inclusions, but the smaller particles can also contribute.

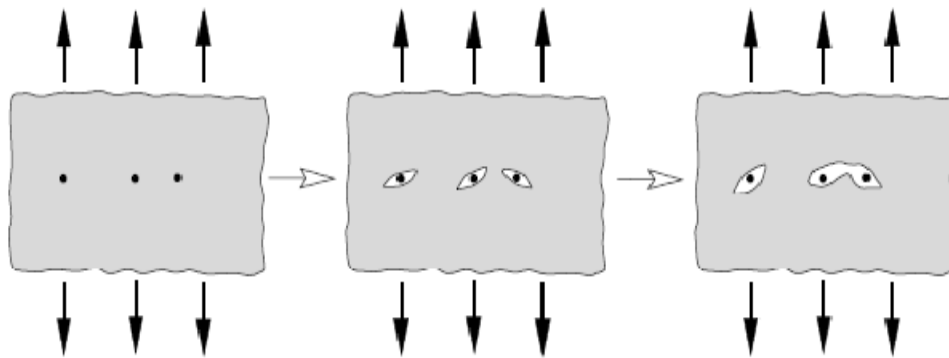


Figure 3.4: Fracture due to inclusion and coalescence of voids.

3.4 Mathematical models

Different micro-mechanical mathematical models have been developed to represent local necking, formation of a crack and crack propagation. These models are implemented in finite element codes to simulate the failure initiation and damage growth; a few of these models are briefly described below.

3.4.1 The Gurson model

The Gurson model analyzes plastic flow in a porous medium by assuming that the material behaves as a continuum. Voids appear in the model indirectly through their influence on the global flow behaviour. The effect of the voids is averaged through the material, which is assumed to be continuous and homogeneous. The main difference between the Gurson model and classical plasticity is that the yield surface in the former exhibits weak hydrostatic stress dependence, while classical plasticity assumes that yielding is independent of hydrostatic stress. This modification to conventional plasticity theory has the effect of introducing a strain softening term [13].

The Gurson model contains a failure criterion. Ductile fracture is assumed to occur as the result of a plastic instability that produces a band of localized deformation. In this model the voids are represented by a single parameter, the void volume fraction. Its evolution equation consists of two terms, namely nucleation and growth.

$$f^{\circ} = f_{growth}^{\circ} + f_{nucleation}^{\circ} \quad (3.20)$$

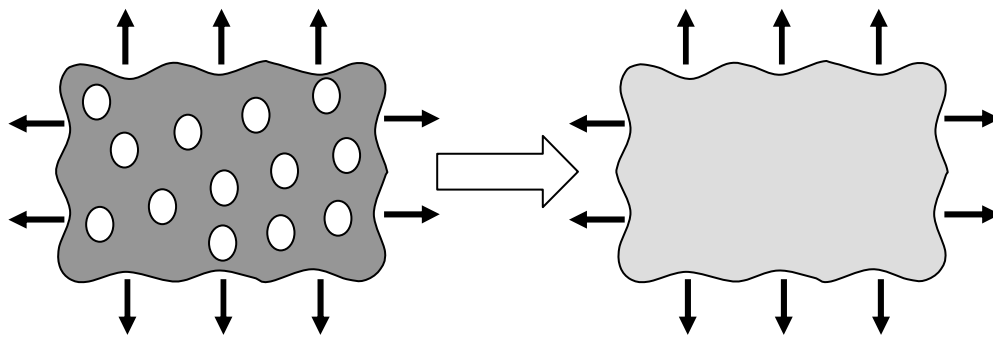


Figure 3.5: The continuum assumption for modeling porous medium.

The void growth rate is proportional to the plastic volume dilatation rate and depends exponentially on stress triaxiality. The nucleation rate can be described by using a strain or stress criterion. The original Gurson model describes the yield surface as follows.

$$\phi = \frac{3}{2} \frac{\sigma'_{ij} \sigma'_{ij}}{\sigma_m^2} + 2f \cosh\left(\frac{3}{2} \frac{\sigma_{kk}}{\sigma_m}\right) - (1 + f^2) = 0; \quad (3.21)$$

where σ_{ij} and σ'_{ij} are the microscopic Cauchy stress and its deviator, respectively. σ_m is the actual flow stress of the matrix material. It is important to note that when $f = 0$, equation 3.21 reduces to the Von Mises yield surface with isotropic hardening.

The original assumption that the micro-voids do not interact is not justified for modeling of final stage of void growth when coalescence of voids by localized internal necking of the intervold matrix occurs, which happens in the real material. Needleman and Tvergaard, therefore, introduced an empirical modification of Gurson's yield function [15].

$$\phi = \frac{3}{2} \frac{\sigma'_{ij} \sigma'_{ij}}{\sigma_m^2} + 2q_1 f^* \cosh\left(\frac{3}{2} \frac{q_2 \sigma_{kk}}{\sigma_m}\right) - \left[1 + (q_1 f^*)^2\right] = 0 \quad (3.22)$$

with f^*

$$f^* = f \quad \text{for } f \leq f_c \quad (3.23)$$

and
$$f^* = f_c + \frac{f_u^* - f_c}{f_f - f_c} \cdot (f - f_c) \quad \text{for } f > f_c ;$$

q_1 and q_2 are two material constants. The modified void volume fraction f^* is introduced to describe the coalescence of voids which occurs after a critical void volume fraction f_c is reached. The constant $f_u^* = 1 / q_1$ is the value of f^* at zero stress. As $f \rightarrow f_i$, $f^* \rightarrow f_u^*$ and the material loses all stress carrying capability. The effect of hydrostatic stress is amplified when $f > f_c$, which accelerates the onset of a plastic instability. A disadvantage of the revised Gurson model is that it contains several new parameters that require calibration.

3.4.2 The Gologanu damage model

The Gologanu model extends the Gurson model by taking into account the changes in microvoid shape that occur during deformation. Indeed, the Gologanu model considers cavities of ellipsoidal form, whose shape and orientation can evolve. The plastic potential is a quadratic formulation which can also be used as a yield function in which σ_M is the elasto-viscoplastic flow stress, q_1 , α_1 and α_2 are material parameters introduced in order to converge the model with full numerical analyses of periodic arrays of voids; f^* is the Tvergaard and Needleman's coalescence function:

$$\Phi = C \frac{\|\sigma' + \eta\sigma_H X\|^2}{\sigma_M^2} - 1 - (q_1 f^*)^2 + 2q_1 f^* \cosh(v) \quad (3.24)$$

where $v = k\sigma_H / \sigma_M$ $\sigma_H = (1-2\alpha_2)\sigma_{11} + \alpha_1\sigma_{11}$

The parameters k , η , C and X depend on the geometry of the ellipsoid void, σ_H is the mean stress. In order to introduce damage due to shearing the damage evolution law is modified to comprise of the sum of the classical law and a new part due to shear loading giving.

$$f^\circ = f_{growth}^\circ + f_{nucleation}^\circ + f_{shear}^\circ \quad (3.25)$$

In pure shear it is commonly accepted that the voids experience a rotation without any change in growth and it appears that nucleation can be generated. Consequently, the damage evolution law due to shearing takes the form of a statistical law with shearing strain and shearing strain rate.

3.4.3 The Lemaitre ductile damage model

In its mechanical sense, damage in solid materials is the presence and growth of microvoids or microcracks, considered continuous at a larger scale. These internal microcracks evolution may lead to a macroscopic complete loss of loading capability of the material, resulting in failure. From a physical point of view, damage is always related to plastic or irreversible strain and more generally to strain dissipation. Therefore, the two dissipative processes, damage and plastic strain, although different in nature, influence each other and should, therefore, be coupled at the constitutive level.

The damage law depends on the damage variable D which evolves between zero and the critical damage value D_c which corresponds to macro-crack initiation. The strain energy density release rate Y ; which is the principle variable governing the phenomenon of damage is expressed by [16].

$$Y = \frac{W_e}{1 - D} \quad (3.26)$$

The strain energy rate W_e is split into shear and hydrostatic parts and leads to the following expression.

$$W_e = \frac{(1 + \nu)}{2E(1 - D)} \langle \sigma_{ij} \rangle \langle \sigma_{ij} \rangle - \frac{\nu}{2E(1 - D)} \langle \sigma_{ij} \rangle^2 \quad (3.27)$$

here E is young's modulus, ν is Poisson's ratio and

$$\langle \sigma_{ij} \rangle = \sigma_{ij} \quad \text{if } \sigma_{ij} \geq 0 \quad \text{and} \quad \langle \sigma_{ij} \rangle = 0 \quad \text{if } \sigma_{ij} < 0.$$

The damage evolution during plastic straining is defined by the following expression [16].

$$D = \left(\frac{Y}{S} \right)^s \varepsilon^p \quad \text{if } \varepsilon^p > \varepsilon_D, \quad (3.28)$$

Where Y is the strain energy density release rate, S and s are material coefficients, ε^p is the effective plastic strain and ε_D is the plastic strain at the damage threshold. The damage evolution and threshold parameters are evaluated in sequence because the damage evolution is localized in the large plastic zone.

3.4.4 Wilkins fracture model

Wilkins et al. [17] proposed a cumulative ductile stain fracture criterion (also known as $D_c R_c$ phenomenological criterion) as an integral function of the equivalent plastic strain ε^p . Two factors encourage strain damage; namely hydrostatic tension and asymmetric shear strain. Hydrostatic tension accounts for the growth of voids in fracture. The voids will ultimately link together to form fracture surfaces. Asymmetric shear strain accounts for the fact that elongation before failure decreases as the shear load increases in fracture tests with combined stress loads.

Mathematically the integral function of equivalent plastic strain is weighted by two terms w_1 and w_2 respectively. The expression is given as;

$$D_w = \int w_1 w_2 d\bar{\epsilon}_p \geq D_c \text{ in } R_c \quad (3.29)$$

where

D_w = damage indicator

$\bar{\epsilon}_p$ = equivalent plastic strain

$w_1 = \left(\frac{1}{1+aP}\right)^\alpha$ hydrostatic-pressure weighting term

$w_2 = (2 - A)^\beta$ asymmetric-strain weighting term

$A = \text{Max}\left(\frac{s_2}{s_3}, \frac{s_2}{s_1}\right), \quad s_1 \geq s_2 \geq s_3$

Here; s_1, s_2, s_3 are the principle stress deviator; the hydrostatic stress is denoted by P ; the material constants a, α, β are found from experimental testing which should cover a wide range of loading conditions ranging from pure hydrostatic to pure shear.

According to the Wilkins criterion, the cumulative ductile fracture occurs when the damage variable D_w exceeds the critical damage value D_c over a critical dimension of the fracture zone, R_c . This critical value is considered to be material characteristics, independent of loading conditions, geometry, or size of a specimen. In addition the fracture occurs if $P \geq P_c$ and $\bar{\epsilon}_p > 0$ where P_c is the critical hydrostatic mean stress, given by [18]

$$P_c = -\frac{1}{\alpha} \quad (3.30)$$

Mathematically, the first term w_1 becomes a complex number if the hydrostatic tensile stress is higher than this absolute value of P_c . Physically, the critical value may correspond to the occurrence of the spalling fracture mode. Spallation is an outstanding failure mode in impact and explosive loading situations [18]. It can also be shown that for a pure shear test (when $P = 0$ and $A = 0$) the equation 3.29 reduces to

$$\bar{\varepsilon}_{pf} = \frac{D_c}{2\beta} \quad (3.31)$$

Similarly, under a restricted loading path of an asymmetric specimen ($A = 1$) subjected to a constant hydrostatic pressure, equation 3.29 could be integrated to give

$$\bar{\varepsilon}_{pf} = D_c(1 + aP)^\alpha = D_c(1 - a\sigma_h)^\alpha \quad , \quad P = -\sigma_h \quad (3.32)$$

3.4.5 Implementation in numerical simulation

Mesh size effect has significant impact on the implementation of failure model in numerical simulations. For example, for sheet metal forming it is important to analyze the initiation of necking zone and the post necking fracture is not of great importance, while in crashworthiness of a structure, the post failure behaviour may be very important. Thus the type and size of element used in meshing has significant importance in order to capture initiation and propagation of cracks.

In the case of the Wilkins model, if the element size is smaller than R_c , the damage D_w centered in the element that breaks first must exceed D_c by an amount that depends on the local damage gradient, the element size, and R_c . If the element size is twice R_c , D_w must equal D_c since the damage is defined in the centre. If the element size exceeds $2R_c$, but is smaller than the distance to the elastic plastic boundary in the direction of crack advance, fracture begins when D_w is smaller than D_c by an amount that again depends on the local damage gradient, the element size and R_c .

3.5 Overview of explicit and implicit finite element methods

The finite element method is a popular computational tool used in engineering research and industrial design. In the field of solid mechanics, and specifically non-linear quasi-static problems, finite element equation solution methods can generally be classed as either implicit or explicit and are solved incrementally. In the implicit approach a solution to the set of finite element equations involves iteration until a convergence criterion is satisfied for each increment. Implicit codes have been used mainly for static problems such as stress and thermal analysis. In explicit analysis time appears in the governing equations permitting the analysis of transient (dynamic) problems including transient thermal analysis, impact problems and in the case of PAM CRASH™ the crashworthiness of automotive structures.

A simple example of spring mass system is used to explain the basis of explicit finite element method. The spring-mass system consisting of a mass (m), a spring with stiffness (k), and an external applied load, $f(t)$. The system has one degree of freedom, where x is the displacement, \dot{x} is the velocity and \ddot{x} is the acceleration of the mass m , figure 3.6.

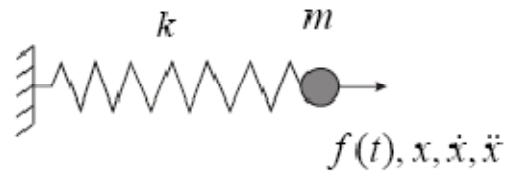


Figure 3.6: Spring-mass system.

The dynamic equation of motion in the equilibrium state is given by:

$$m\ddot{x} + kx = f(t) \quad (3.33)$$

The explicit method uses conventional finite elements to discretise the structure. The problem is formulated as a dynamic one using the linearized equations of motion, from which a solution in the time domain is obtained. The known quantities are the displacement at time t_n , x_n , and the velocity at time $t_{n-1/2}$, $\dot{x}_{n-1/2}$. Dynamic equilibrium equation at time t_n is expressed as:

$$m\ddot{x}_n + kx_n = f(t_n) \quad (3.34)$$

As all the other variables are known in the equation 3.34, so it is possible to find \ddot{x}_n by using explicit forward Euler central difference time integration scheme to solve unknown quantities.

$$\begin{aligned}\ddot{x}_n &= m^{-1}(f(t_n) - kx_n) \\ \dot{x}_{n+1/2} &= \dot{x}_{n-1/2} + \Delta t_n \ddot{x}_n \\ x_{n+1} &= x_n + \Delta t_{n+1/2} \dot{x}_{n+1/2}\end{aligned}\tag{3.35}$$

Explicit methods are conditionally stable and thus require a time step to be smaller than some critical value Δt_{crit} , while implicit method may be unconditionally stable with a certain choice of parameters. Δt_{crit} is related to the smallest time it takes for ‘wave propagation’ across any element or highest ‘frequency’ in the finite element mesh [19]. Critical time step is calculated according to formula:

$$\Delta t_{crit} \leq \frac{L}{c},\tag{3.36}$$

where L – characteristic length of the element;

$$c = \sqrt{\frac{E}{\rho}} \text{ – speed of sound in the material.}$$

From the above equations it can be observed that a stiff or low-density element decreases the critical time step.

The implicit method computes each element’s stiffness, which depends on the element type and the material model, and then assembles the global structure stiffness matrix $[K]$. This matrix provides the relationship between nodal displacements $\{u\}$ and applied nodal forces $\{F\}$ for the structure:

$$\{F\} = [K] \{u\} \quad \text{or} \quad \{u\} = [K]^{-1} \{F\}\tag{3.20}$$

The nodal displacements are then used to compute element stresses and strains. Problems involving contact and non-linear material behaviour yield a non-linear stiffness matrix [K]. In this case a CPU intensive iterative solution is necessary to determine the nodal displacements for a given loading. The implicit method is better for static problems and is unconditionally stable whereas explicit methods are superior for quasi-static problems with careful choice of loading.

PAM-CRASHTM explicit solver is used to solve the finite element numerical simulations, in the research work. Pre-processing and development of the model is done in PAM-MESHTM, the next step is the application of boundary conditions and numerous constraints using VISUAL-PAMTM, the final model is solved with the help of PAM-CRASHTM explicit solver and in the last the results are interpreted in the PAM-VIEWERTM. PAM-CRASHTM uses several models, one of which is the Wilkins cumulative strain damage model.

Chapter 4 : Experimental Investigation

A series of experimental tensile tests were performed on different types of aluminium alloy test specimens, in order to determine the strength, deflection behaviour, and fracture propagation in each type of specimen. Two types of methods were used to measure the displacements and strains in the specimens.


- Displacement transducer
- Optical strain measurement technique

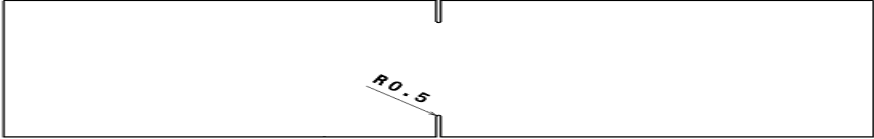
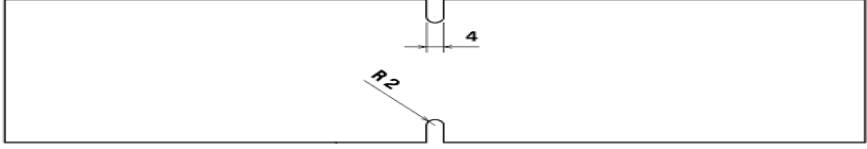
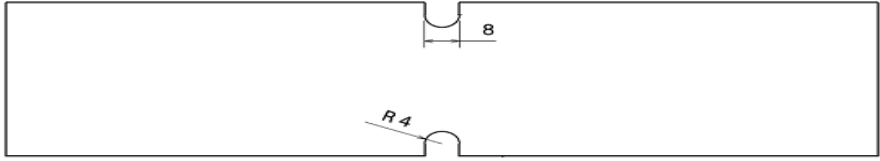
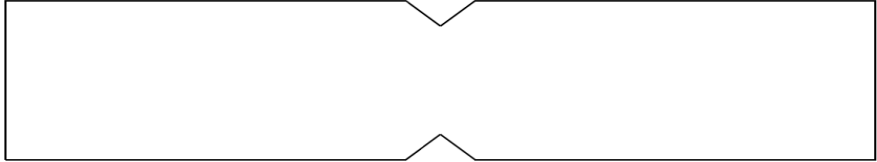
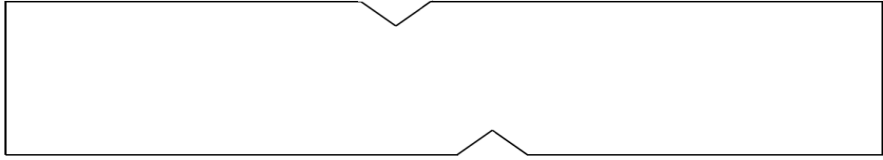
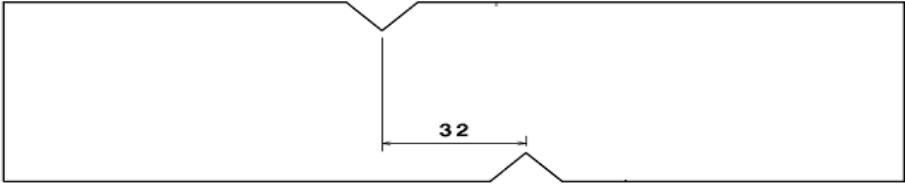
4.1 Preparation of specimens

Macroscopic defects of different types, which lead to the fracture of the automotive structure during crash, were replicated in the test specimens and tensile test was performed on each of the specimen type. The tensile test is used to provide a load displacement curve for the failure of each specimen. The test specimens are divided into two main categories;

- Notched specimens
- Hole in plate specimens

Notched specimens were further divided into U-shaped notched specimens and V-notched specimens. V-notched specimens have aligned and offset notches on the plate to represent the symmetry. Table 4.1 shows the geometry and types of various notched specimens used to gather data.

SR	Specimen type
1	 <p data-bbox="760 1816 1133 1852">Parallel coupon (No notch)</p>

<p>2</p>	 <p>Slit 1mm diameter notch</p>
<p>3</p>	 <p>4mm diameter notch</p>
<p>4</p>	 <p>8mm diameter notch</p>
<p>5</p>	 <p>V- notch aligned</p>
<p>6</p>	 <p>V-notch offset</p>
<p>7</p>	 <p>V-notch offset</p>

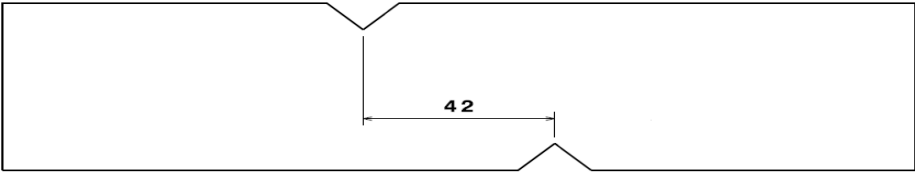
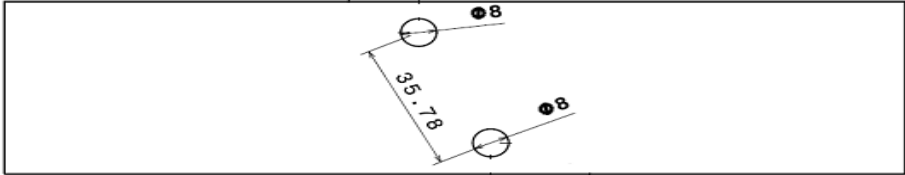
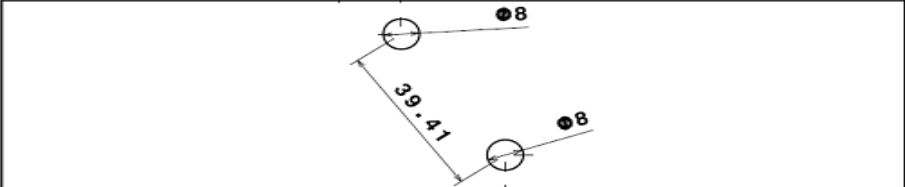
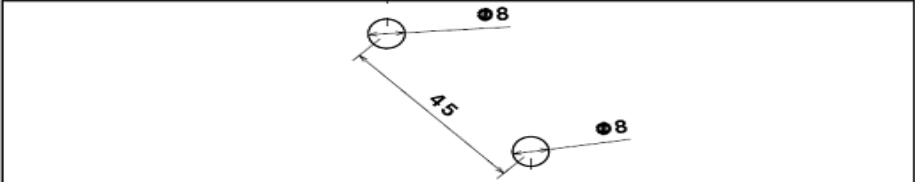
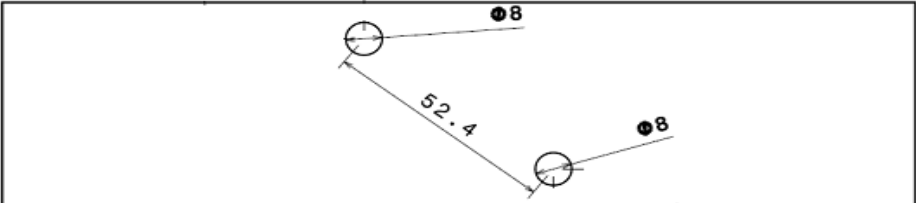
<p>8</p>	 <p>V-notch offset</p>
<p>10</p>	 <p>Holes in plate symmetric around plate axis</p>
<p>11</p>	 <p>Holes in plate symmetric around plate axis</p>
<p>12</p>	 <p>Holes in plate symmetric around plate axis</p>
<p>13</p>	 <p>Holes in plate symmetric around plate axis</p>

Table 4.1: Types of specimen tested

The detailed drawings of the specimens in table 4.1 with dimensions are attached in the appendix at the end. All the specimens are machined in the workshop from aluminium alloy sheet material. Due to the inconsistency in the thickness of the aluminium sheet, multiple samples of a particular specimen have different thickness. Special care has been taken while calculating the stresses and strains of the specimens because of the variation in the thickness. The first batch of coupons of all types has been tested in the conventional tensile testing machine.

4.2 Test procedure

The equipment used in performing the tensile tests are; tensile testing machine, machine control unit, extensometer to measure the displacement, load cell, data processing channel and a personal computer attached to the data channel. The specimen is attached between the lower and upper clamps of the testing machine. The lower clamp of the machine is fixed and extension force is applied on the upper clamp. Both the clamps are operated by hydraulic actuator. The control unit provides the flexibility to change the rate of extension or velocity of the upper clamp and amount of extension force. The vertical movement of the upper part of the machine is also simulated by hydraulic actuator. Load cell and extensometer are attached to the data processing channel, which is connected to the computer by serial port. Software is used to interpret the signals from the data channel and this data is simultaneously stored and shown as a run time load displacement curve.

The following testing conditions were considered in order to perform the tensile test on the specimens;

- All the tests were conducted at room temperature and specimens used for testing were not heat treated.
- Default values of extension hydraulic force used. Load cell attached on upper clamp measured the amount of force on the specimen.
- A constant velocity of 2 mm/min was used to control the movement of upper clamp.
- Same gauge length was used for each specimen in order to get consistent and accurate readings on the extensometer.

Figure 4.1 shows the tensile machine used for performing the tests and U-notched specimens that were tested. In the figure, upper and lower clamps are evident with lower clamp fixed.

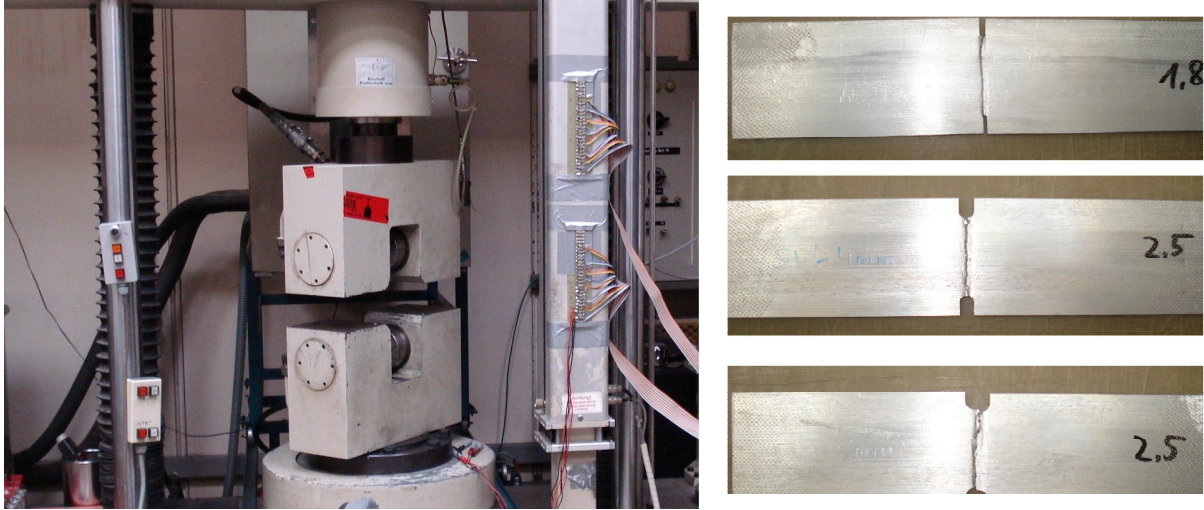


Figure 4.1: Tensile testing machine and U-notched tested specimens

4.3 Optical strain measurement

The second type of testing performed to measure the stresses and strains in test specimens, is the optical strain measurement technique along with tensile testing. In this testing technique, instead of attaching strain gauges on the specimen and then converting the displacements into strains, high speed digital cameras were used to capture the images of the specimen and these images were analyzed in special ARAMIS [20] software to determine stresses and strains during the tensile testing. The accuracy of measuring strains using optical strain measurement technique is better as compared to conventional strain gauges. It also allows the real time monitoring of results at multiple measurement positions on the test object surface. Besides the measurement of strains, optical strain measurement technique was also used for the determination of material properties such as, Young's modulus and verification of Finite Element Analysis.

ARAMIS provides the full-field verification of finite element simulation. It evaluates the strains and helps in comparing the results with the FE-simulation, in this way the finite element simulations can be optimized to get reliable results.

4.4 Test procedure

The main equipment that is used in the test is the tensile machine and optical strain measuring device. Strain measurement device consists of two cameras mounted on the same platform, a data acquisition channel and a processing unit installed with ARAMIS software. Data cables are used to connect the cameras and data acquisition channel which in turn connected with the processing unit. Rate of image capturing is controlled by software and it varies from the nature of test specimen which is being tested. Once the test is completed all the images are stored on the hard drive and later analyzed using the software.

The extensometer, which was used previously for the measurement of displacement in specimen, is not used instead of that cameras serve the purpose to capture the movement of the specimen. Before the start of the tensile test, the equipment is calibrated by the series of predefined calibration tests to make sure that the desired surface area of the test specimen is captured by the cameras and properly used in the estimation of stresses and strains. For this kind of testing, test specimens need special preparation. Smooth or shiny surface is not captured in the images and this severely affects the quality of images, so white powder paint is used to make the surface of specimen coarse and matt. Black paint is sprayed on top of the white dull base, this creates the pattern of spotted surface, as shown in figure 4.2, and used for taking reference points in the ARAMIS software.

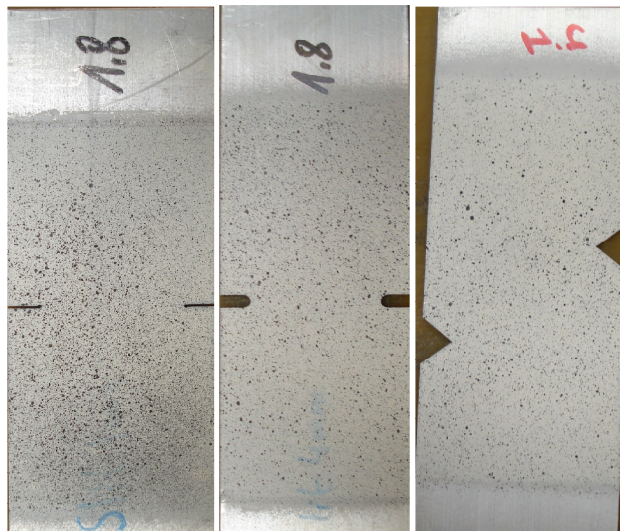


Figure 4.2: Test specimens coated with white and black paint.

The prepared specimens are tested in the tensile testing machine. The test specimen is fixed in the upper and lower clamp of the tensile machine. During the fixing of the specimen, care has been taken to make sure that the critical area, which is to be captured in the images, is directly in range of cameras. All the tests are conducted on room temperature and the paint on the specimens is fully dried. Tensile machine and cameras are triggered simultaneous to reduce error. Default values of extension hydraulic force used with load cell measuring the amount of force on the specimen. All tests are conducted with a constant velocity of 2 mm/min to control the movement of upper clamp. Light plays a vital role in the quality of images, so proper lighting is used all the time in the room. In figure 4.3, left is the tensile machine and cameras to capture the images and right is the runtime images displayed on the screen.

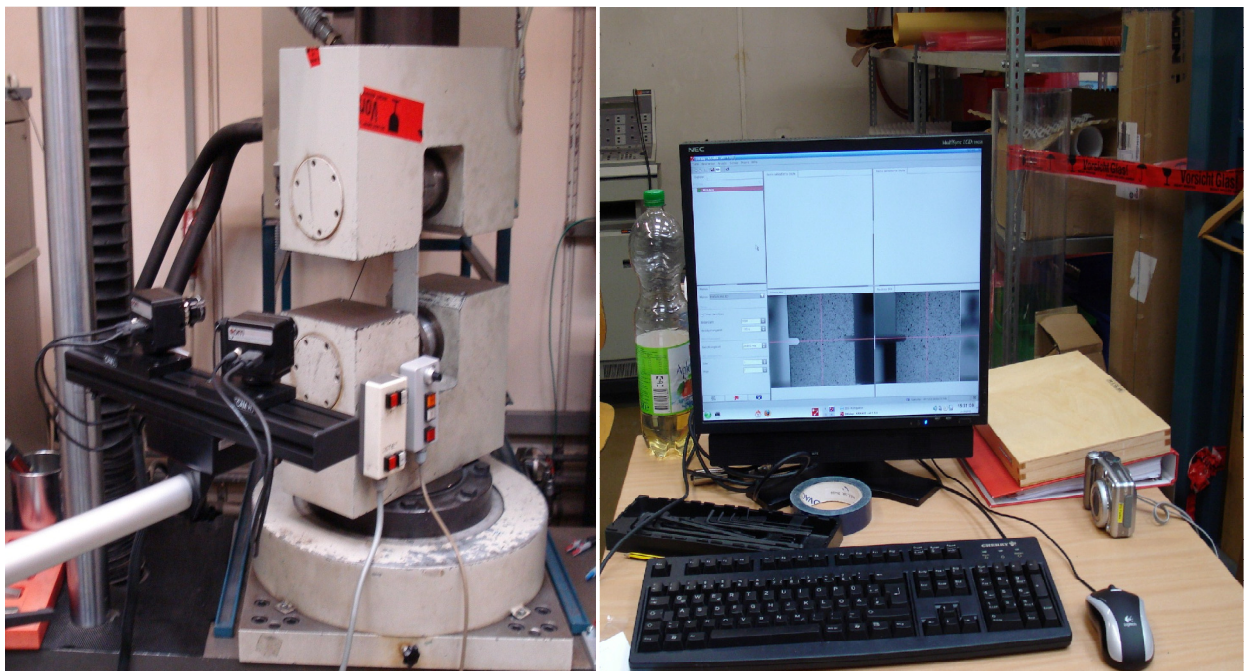


Figure 4.3: Experimental setup of optical strain measurement.

Chapter 5 : Finite Element Model

5.1 Model formulation

Most of the engineering analysis can be performed by using mathematical models which lead to differential equations. These models basically represent certain engineering phenomena. The main purpose of using numerical techniques is to solve complicated problems, which cannot be solved by analytical methods. There are many numerical techniques available such as finite element methods (FEM) and finite difference techniques, but the most widely used is the FEM.

In contrast to analytical methods, where solutions are found that hold over the entire region, in FEM the whole region is divided into a finite number of parts, elements and the approximation is carried out over each element. So in this way, it is easy to estimate the solutions for each element as the approximations are easy.

Although the numerical techniques used in a modern FEM code is solved by the computer, but still the knowledge about basic concepts and theories used in the FEM program is very important for proper understanding of the problem. It is important for the researcher to understand the problem and how to model that problem, what are the assumptions and limitations of a particular FEM code and, finally, interpretation of results that are obtained from the code.

5.1.1 Geometric model

First step in all numerical analysis methods is to develop a finite element (FE) model which includes geometry, set of assumptions and loading conditions used to define the real physical problem. Modeling is clear representation of the parts of an object which is suitable for computer processing. The models for the FEA are created with all the actual dimensions using CATIA [21]. CATIA is parametric, feature-based solid modeling software. The models prepared in CATIA are already illustrated in detail in the previous chapter.

5.1.2 Assumptions

In some of the engineering problems, it is not possible to develop a FE model that can exactly represent the real physical system particularly in case of complex engineering systems. In order to develop a FE model which is close to the reality, the researches have to consider all the aspects of the problem which make the FE model complex and increase the computational time. Certain set of assumptions are consider by the researchers to simplify the complex FE model. The assumptions used in this project are as under;

- Variation in material properties of the specimen, with temperature is not considered.
- Dynamic loading of the specimen is ignored.
- Uni-axial with constant application of force.

5.1.3 Material properties

The specimens are modeled by the liner elastic anisotropic aluminium alloy material with Young's modulus $E = 69$ GPa and poisson's ratio $\nu = 0.3$. Because the specimens are thin with thickness between 1.8mm- 2.5mm, they are modeled using thin shell elements.

5.1.4 Boundary conditions

During a tensile test different loadings are acting on the specimen boundary. In order to simulate the specimen conditions exactly as it was during the tensile test, certain boundary conditions are defined. The purpose of these boundary conditions is to simplify the model without losing a realistic approximation. The set of boundary conditions that are used on the specimen are illustrated in Figure 5.1. The description of these boundary conditions is given as follows.

- The left side boundary of the specimen is fixed so that the displacements in all degree of freedoms (6 DOF) are fixed.
- The right side boundary is fixed in all the degree of freedoms except the x-axis so that the movement is only in the x-direction.

5.2.5 Loading conditions

In tensile test, uni-axial loading was applied with constant extension of the specimen. In the tensile machine default values were used and the specimen was pulled with a constant velocity. This same effect of extension has been implemented in the simulation. The left side of the meshed model is constrained with a forced boundary condition that represents a constant velocity of 0.1 mm/msec and this constant velocity is applied for 10msec. This means that the left side of the model will be pulled with a constant velocity only in the x-direction. Figure 5.1 demonstrates the loading condition used in FE model.

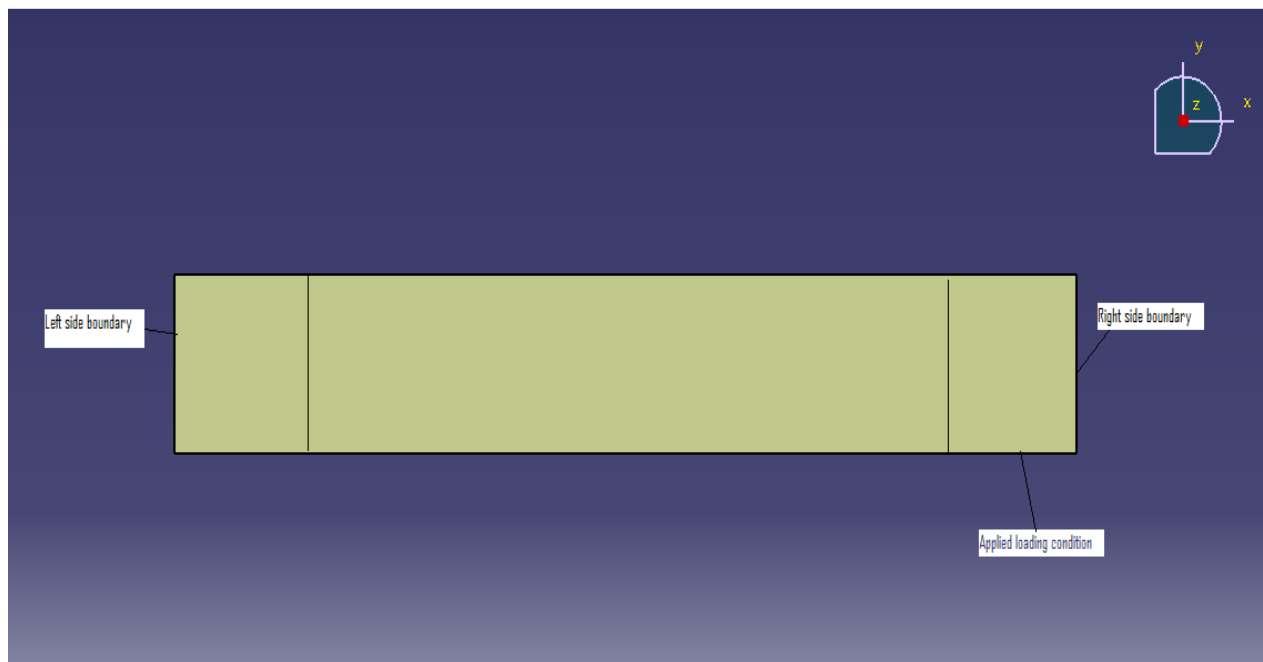


Figure 5.1: Boundary and loading conditions used in the FE model.

Chapter 6 : Finite Element Analysis and Simulation

After the modeling phase, the generated model is analyzed in PAM-CRASH™. Two major analysis approaches have been used and the corresponding simulation results are presented. The main purpose of the numerical simulation is to analyze the variation of stress distribution in the specimens, shape deformation and to compare the failure simulation results with the experimental results.

The FEM model defined in the previous chapter is implemented in PAM-CRASH™. This model is used to run number of simulations, analyze simulations results and refine the model. The two different approaches that have been used to create the PAM-CRASH model are;

- Shell element
- Solid element

Each approach is briefly explained in the following sections.

6.1 Shell elements simulation

Shell elements are characterized as 2-dimensional elements in a plane. So the thickness of the elements are assumed to be negligible. A number of shell element types library is available in PAM-MESH, but only three nodes triangular and four nodes quadrilateral thin elements elements with thickness t are used to mesh the specimen models. Thin shell finite elements are used to discretize the structures made of plates and shells. To predict the stress distributions across the thickness resulting from plastification requires integration in the thickness direction [22].

Usually 3 integration points are sufficient in most cases to integrate bending and membrane effects. To add the precision 4 or 5 points can be added and is typically used in the case of spring back simulation, but this adversely effects the CPU time.

6.1.1 Methodology

The FE model defined in chapter 5 is implemented in PAM-CRASH. First the cad file of parallel specimen is imported in PAM-MESH. Since this cad file represents the 2-dimensional surface of the parallel specimen, so shell elements are used to mesh the specimen. PAM-MESH

has two options for the meshing of cad file. In auto meshing process, the program chooses the most optimal configurations and meshes the surface, the mesh quality is controlled and those elements which do not satisfy quality are removed automatically. The other method uses surface meshing options which are input by the user. The produced mesh is checked for quality and poor elements. The full scale model of shell elements is produced for the parallel specimen, as shown in the figure 6.1.

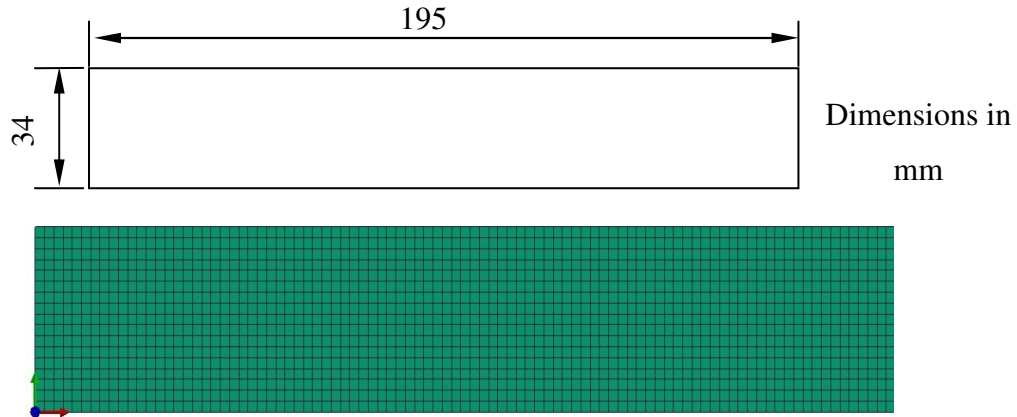


Figure 6.1: Full model of the Parallel specimen.

6.1.2 Mesh size

Mesh size has direct affect on the CPU time and result accuracy. Large mesh size means that the numbers of elements are few and small number of iterations, which reduces CPU time. Mesh size is initially kept large to control the CPU time and after running few simulations it is adjusted to a level which is shown in figure 6.1.

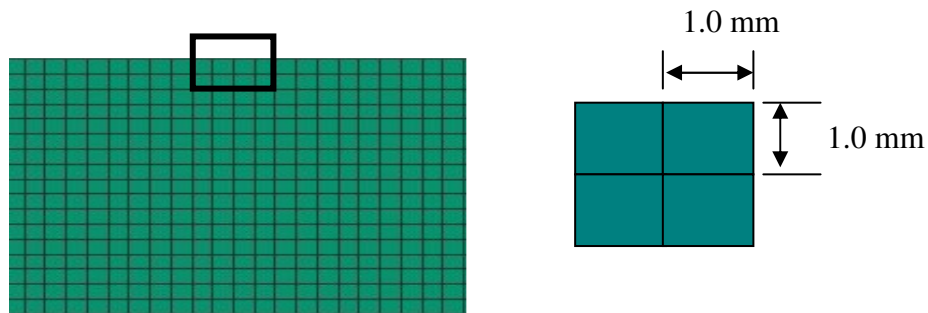


Figure 6.2: Shell elements mesh size for Parallel specimen.

6.1.3 Boundary Conditions

Boundary conditions are essentially the same for shell and solid element models. Since full models are used for the analysis of all types of specimens, no modification is needed in the boundary conditions otherwise required for half model. Figure 6.3 shows the boundary conditions for the parallel specimens. These boundary conditions are same for all types of specimens tested during the tensile testing.

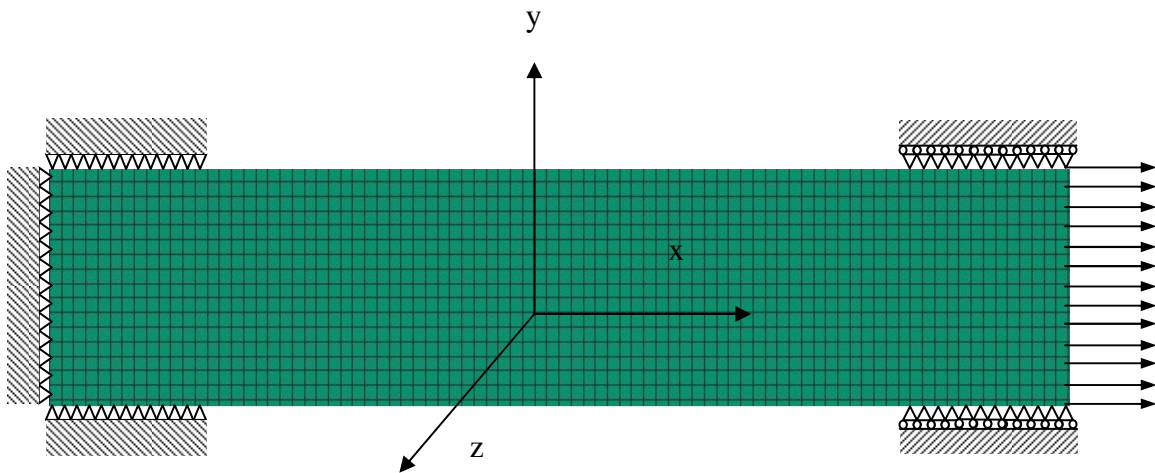


Figure 6.3: Boundary conditions for Parallel specimen.

The nodes at the left end of the specimen have been fully restrained. No movement is allowed in the x , y or z directions. On right end of the specimen, a constant extension force is applied, in the positive x direction. In order to simulate the clamping force applied on the specimen by the clamp of the tensile machine, the corresponding area has been restrained in the y and z directions.

6.1.4 Shell material card

The critical areas of failure for specimens are the notches. It is important that the model is properly modeled in this area. In order to simulate these effects, a combination of boundary conditions and material modeling had to be used. There are wide varieties of material models available in the PAM-CRASH library. These material models are divided into shell and solid material models. Shell material models are for shell elements types and solid material models are

for solid elements types. After careful interpretation of the problem, an appropriate material model is chosen.

From the material model library in PAM-CRASH, a material model 109 [22] has been used to represent the specimen material. Material type 109 corresponds to anisotropic elastic-plastic shell material with enhanced non quadratic Hill's 1990 and Barlat's yield surface function instead of quadratic Hill's 1948 yield surface function. This material type has been chosen because it reflects the sheet metal stamping process where the material is anisotropic in nature as in the case of aluminium sheet metal. The material has been further divided into four material phenomena:

- Elastic behaviour
- Elastic-plastic behaviour
- Anisotropic plastic behaviour
- Failure criterion

The elastic behaviour of the material is considered by; elastic modulus, shear modulus, Poisson's ratio and thickness t . In addition to that, classical membrane stiffness and bending stiffness are also included. Elastic-plastic behaviour can be simulated in multiple forms by;

- Defining bilinear material via the yield stress curves.
- Specifying pairs of plastic tangent modulus and the effective plastic stress.
- Power rule definition, specifying parameters a , b and n for the function;

$$\sigma(\varepsilon) = a + b \varepsilon_p^n \tag{6.1}$$

where ε_p is the effective plastic strain.

- Krupkowsky hardening function with parameters k , ε_0 , and n

$$\sigma(\varepsilon) = k(\varepsilon + \varepsilon_0)^n \tag{6.2}$$

where ε is effective plastic strain.

Special testing techniques required to calculate the parameters of Krupkowsky hardening function and that of power rule. Instead of these functions, true stress-strains curves are used to simulate the elastic-plastic behaviour. The anisotropic plastic behaviour is defined by in-plane orthotropic Barlat's plasticity function. There are seven parameters which are required to initiate

Barlat's plasticity model and these parameters are unique for every material. In this case these parameters have been provided by Audi.

Shell elements are eliminated by a failure criterion. According to this failure criterion, if the plastic strain maximum for an element exceeds the specified maximum plastic strain, ϵ_{pmax} , or if the time step calculated for an element of this type falls below the specified minimum allowed time step, Δt_{min} , then its material resistance is removed from the calculations, while its mass is conserved.

Instead of defining the single value of maximum plastic strain it is also possible to define a curve, called the Forming Limit Diagram FLD. In that case the element will be eliminated if principal strains for this element exceed the specified Forming Limit Diagram [22]. Figure 6.4 shows the FLD that has been used to define the failure criterion of the shell elements; this curve is also provided by Audi. A detailed description of the Forming Limit Diagram and how it is produced has been previously given in section 3.2.5.

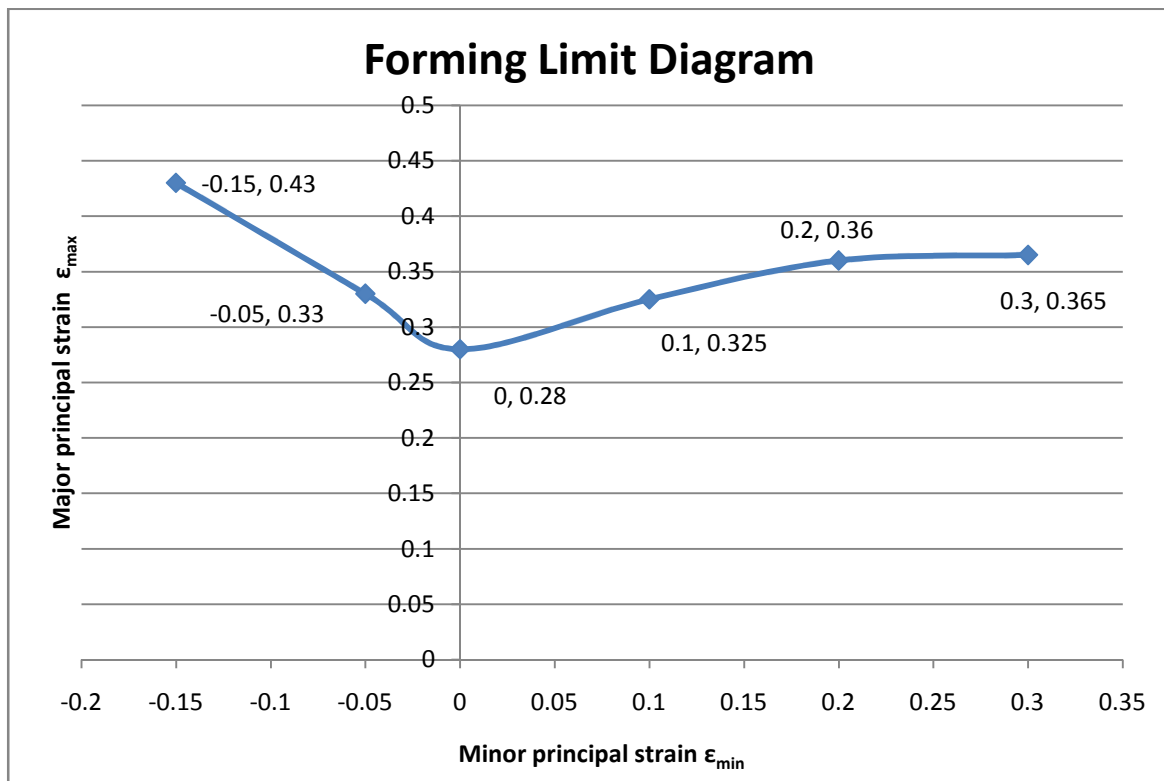


Figure 6.4: Forming limit diagram used as failure criterion.

Figure 6.4 shows the set of material properties, their values and various parameters that are used in the material card for shell elements.

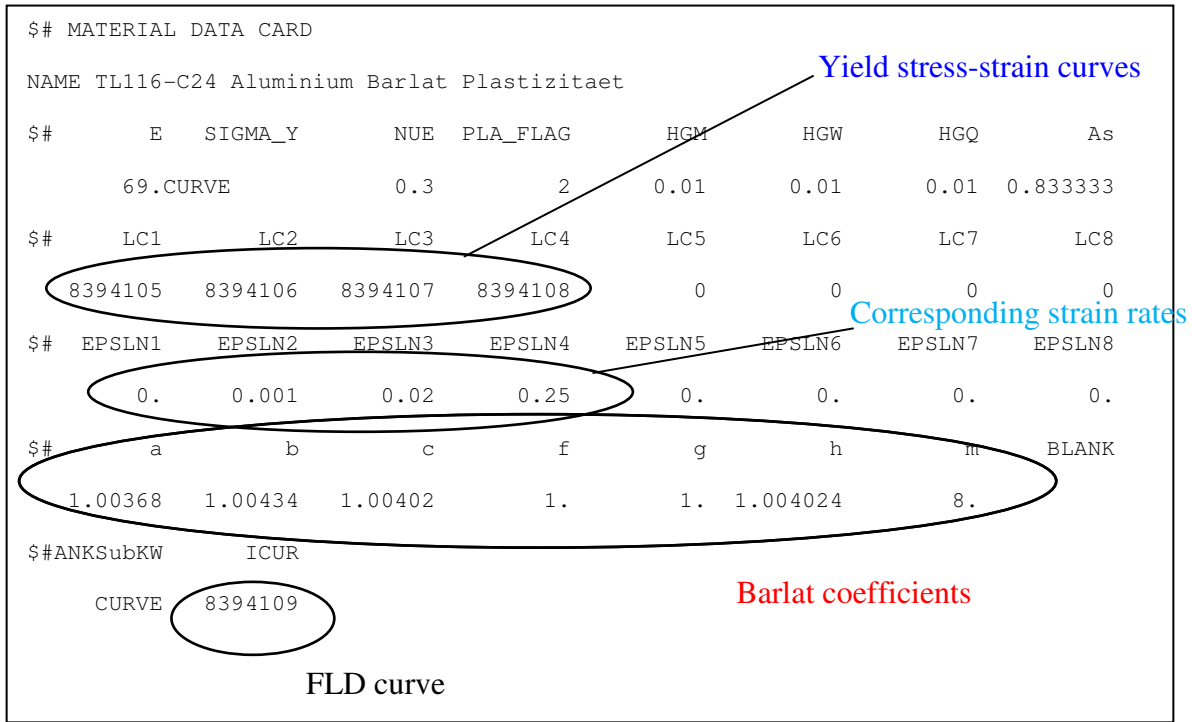


Figure 6.5: Shell element material card.

6.2 Simulation results

In the following section a series of figures are presented. These figures provide the comparison between the test results and simulation results for the shell element model of the specimens. For parallel specimen the simulation result has been extracted from the element which lies in deformation area, approximately in the middle of the specimen. In the case of other specimens this procedure is not possible because of the presence of defects.

To cater for this problem, reaction force boundary output has been applied in the PAM-CRASH model. This measures output reaction force on the fully restrained side of the simulation model and results are analyzed in the PAM-VIEWER.

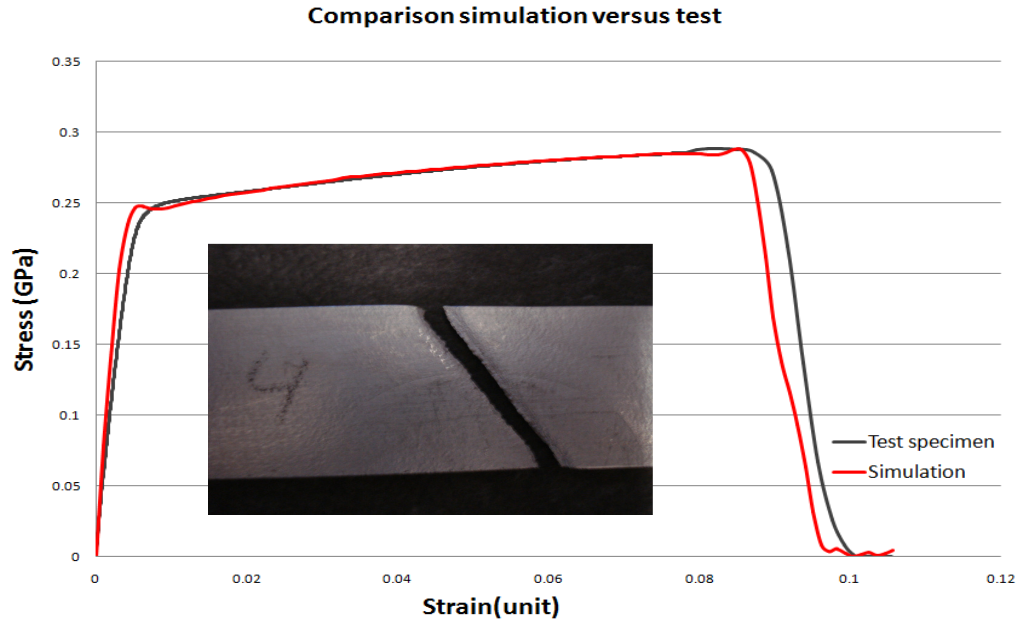


Figure 6.6: Comparison of the simulation with the experimental results for the parallel specimen with 2.4mm thickness

Figure 6.6 shows that the simulation and test results match with great accuracy. FLD diagram failure criteria working perfectly for the parallel simulation.

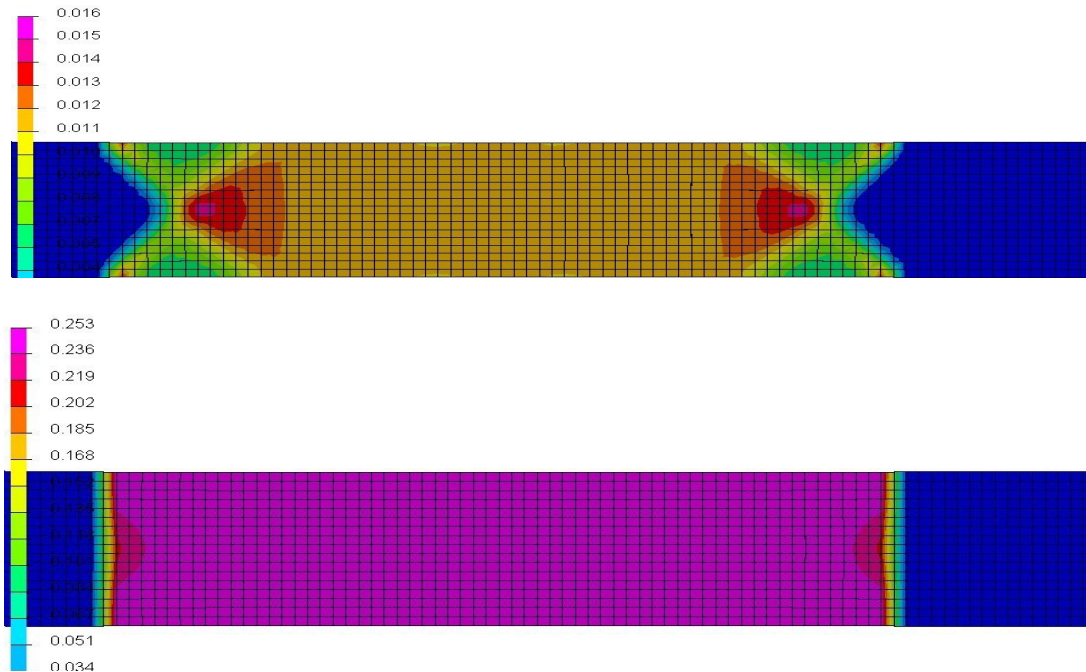


Figure 6.7: Figures of max plastic strain and max Von-Mises stress in parallel specimen

6.2.1 Notched specimens

Numerical models are used to produce simulations of three U-notched specimens and three V-notched specimens. The results of which are presented in the following figures.

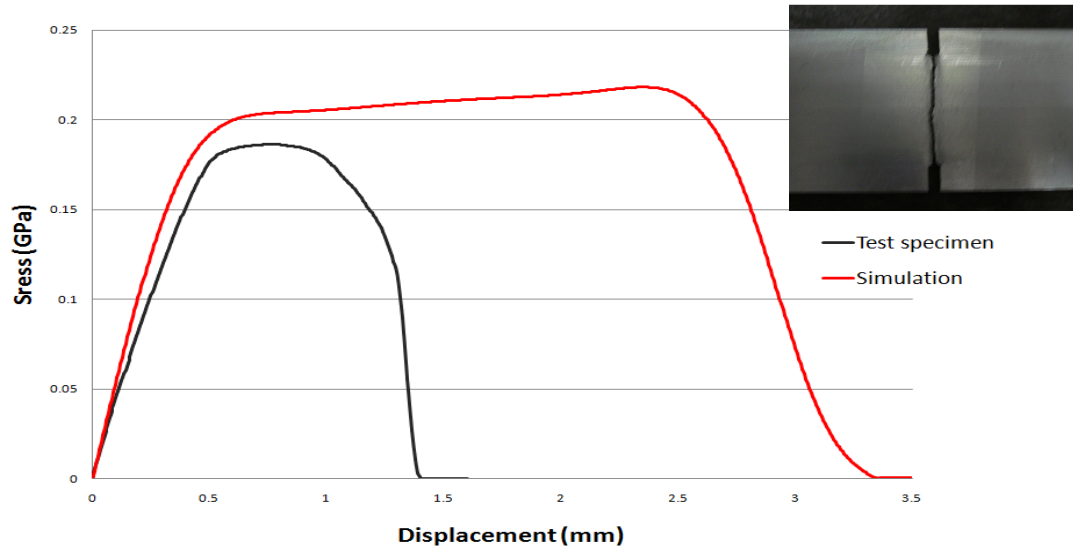


Figure 6.8: Comparison of the simulation with the experimental results for 1mm diameter slit specimen of thickness 1.8mm

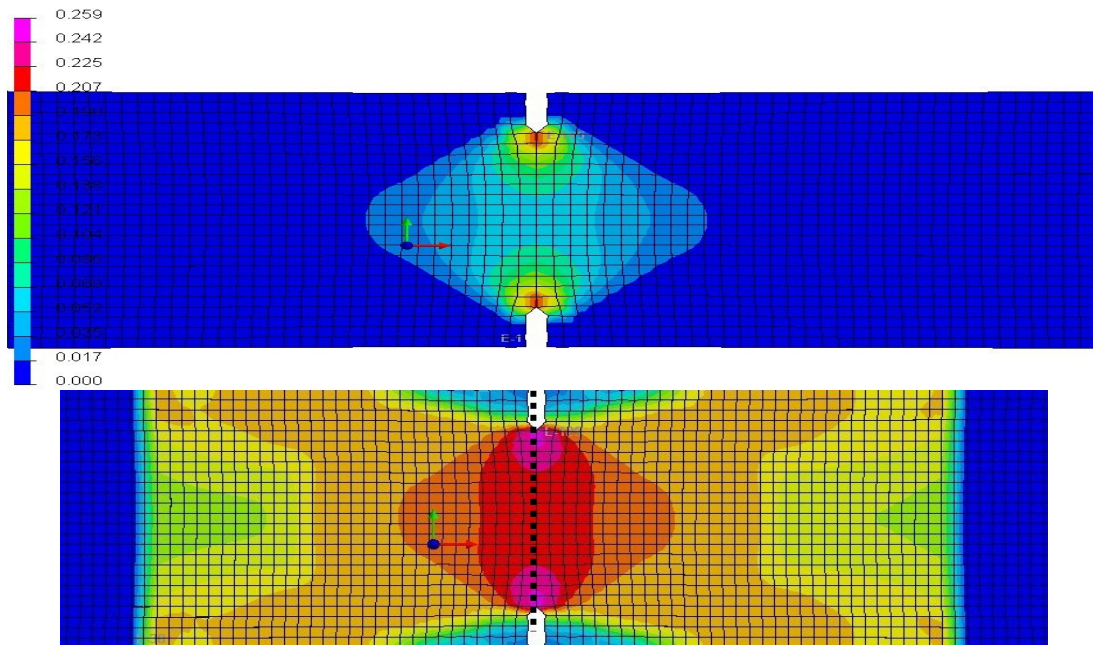


Figure 6.9: Figures of max plastic strain and max Von-Mises stress in the 1mm slit specimen before the start of crack, ---- indicates final failure path.

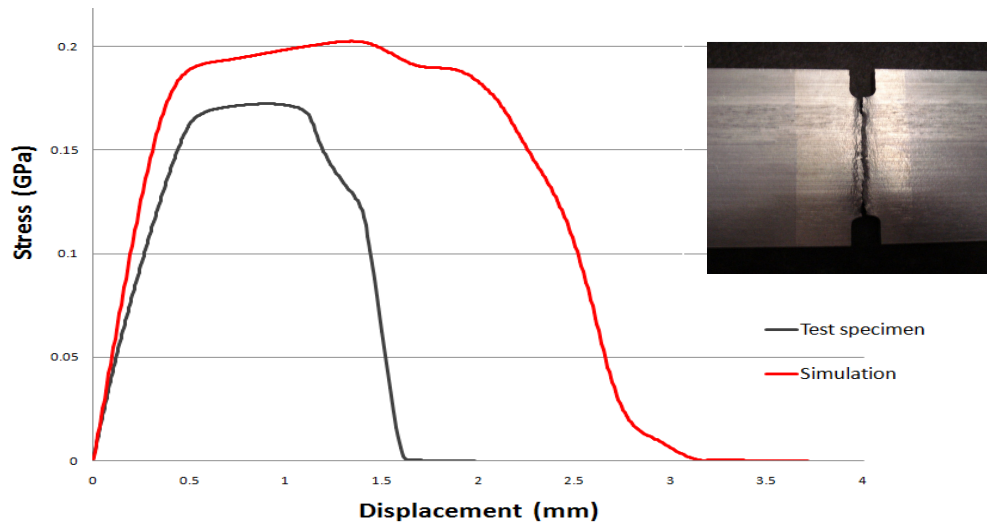


Figure 6.10: Comparison of the simulation with the experimental results for 4mm diameter U-notch specimen with 2.5mm thickness

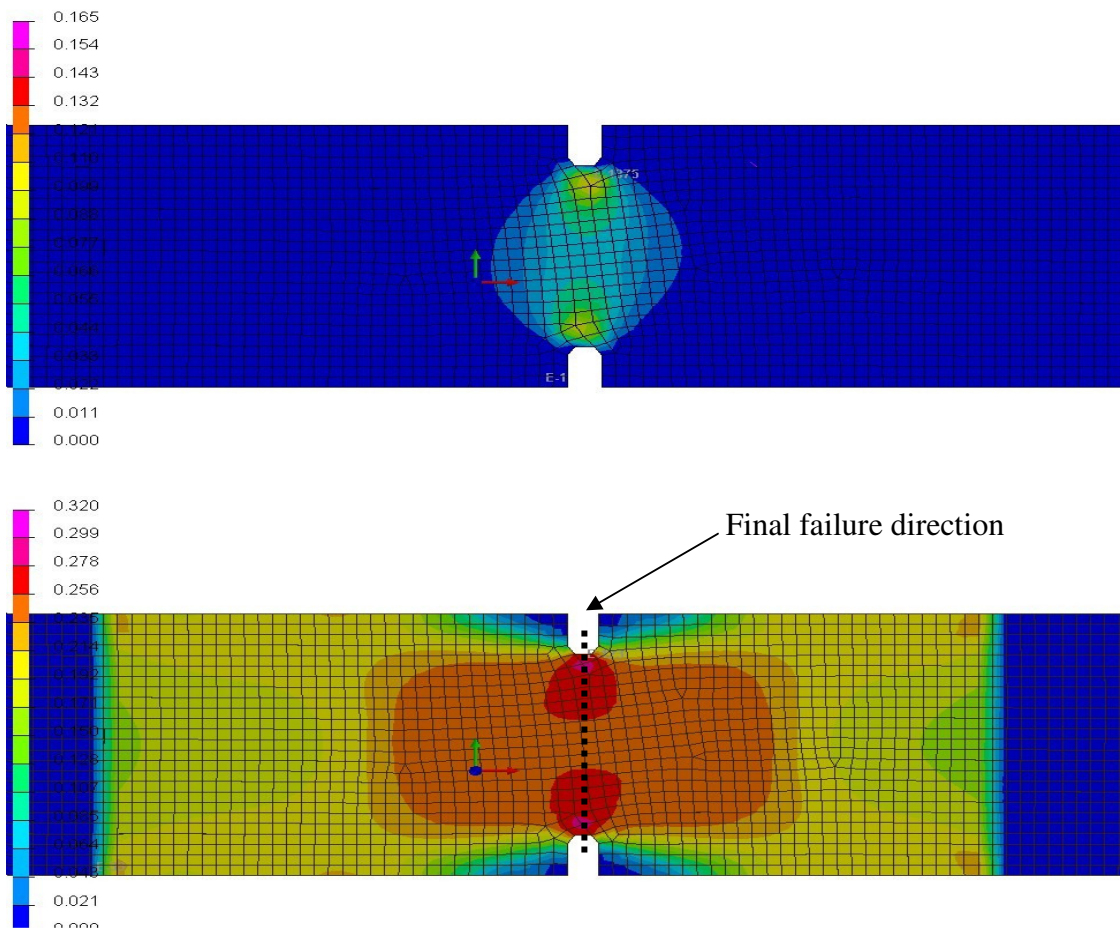


Figure 6.11: Figures of max plastic strain and max Von Mises-stress in the 4mm diameter U notch specimen, ---- indicate final failure path.

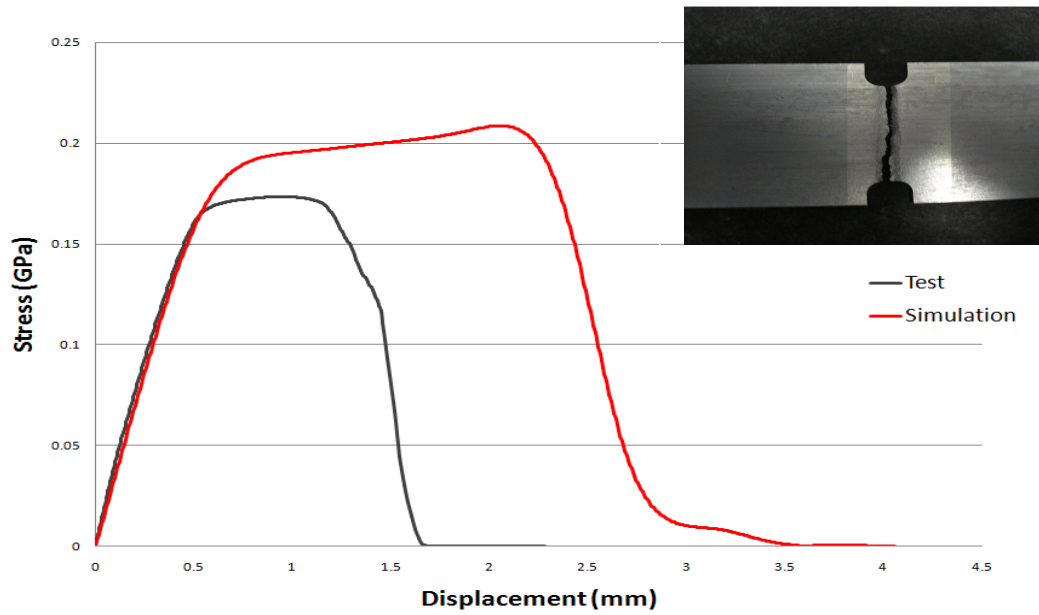


Figure 6.12: Comparison of the simulation with the experimental results for 8mm diameter U-notch specimen with 2.5mm thickness.

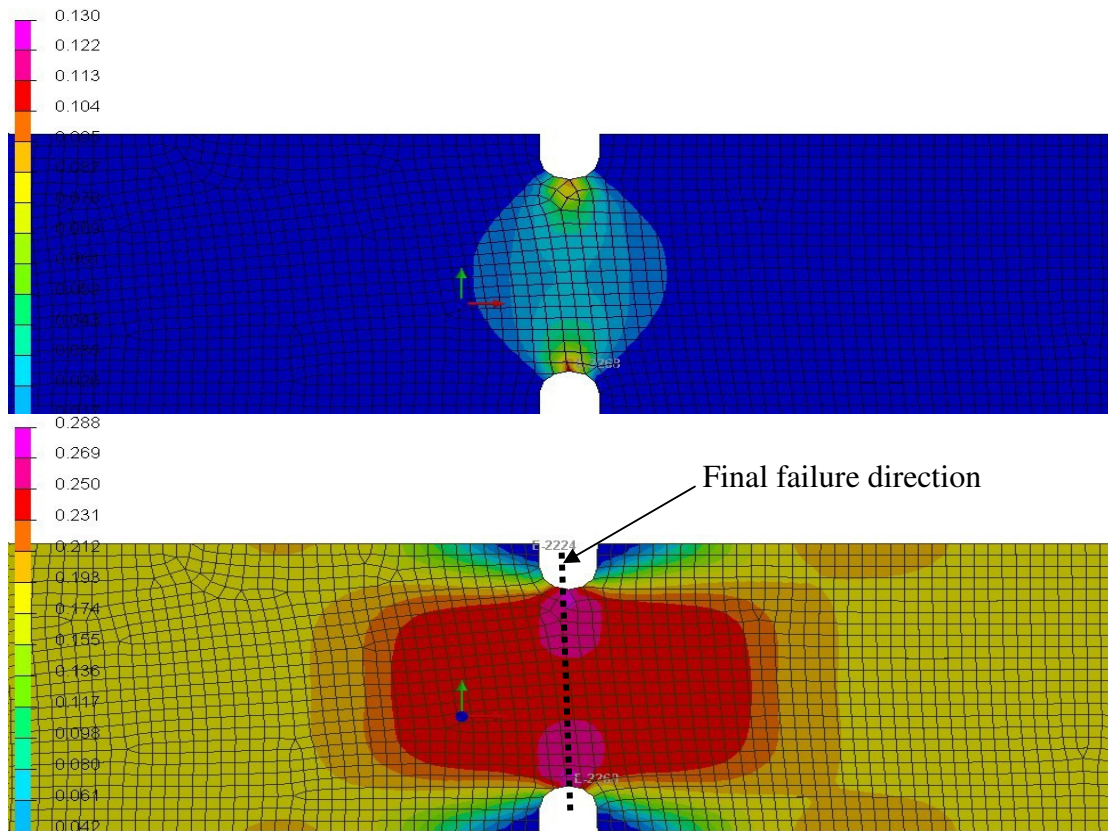


Figure 6.13: Figures of max plastic strain and max Von-Mises stress in the 8mm diameter U notch specimen, ---- indicates final failure path.

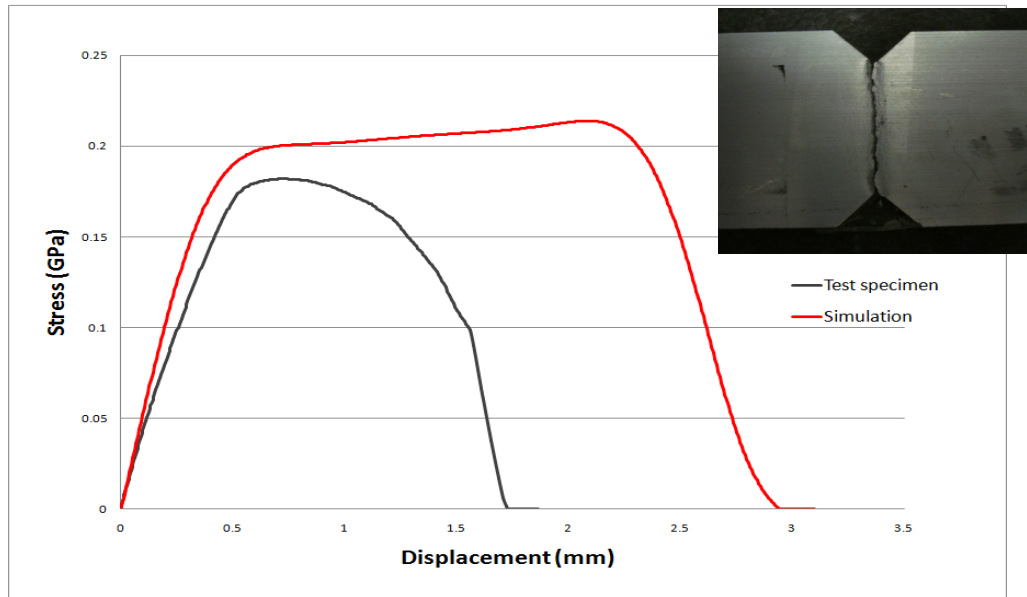


Figure 6.14: Comparison of the simulation with the experimental results for V-notch specimen aligned with 2.4mm thickness

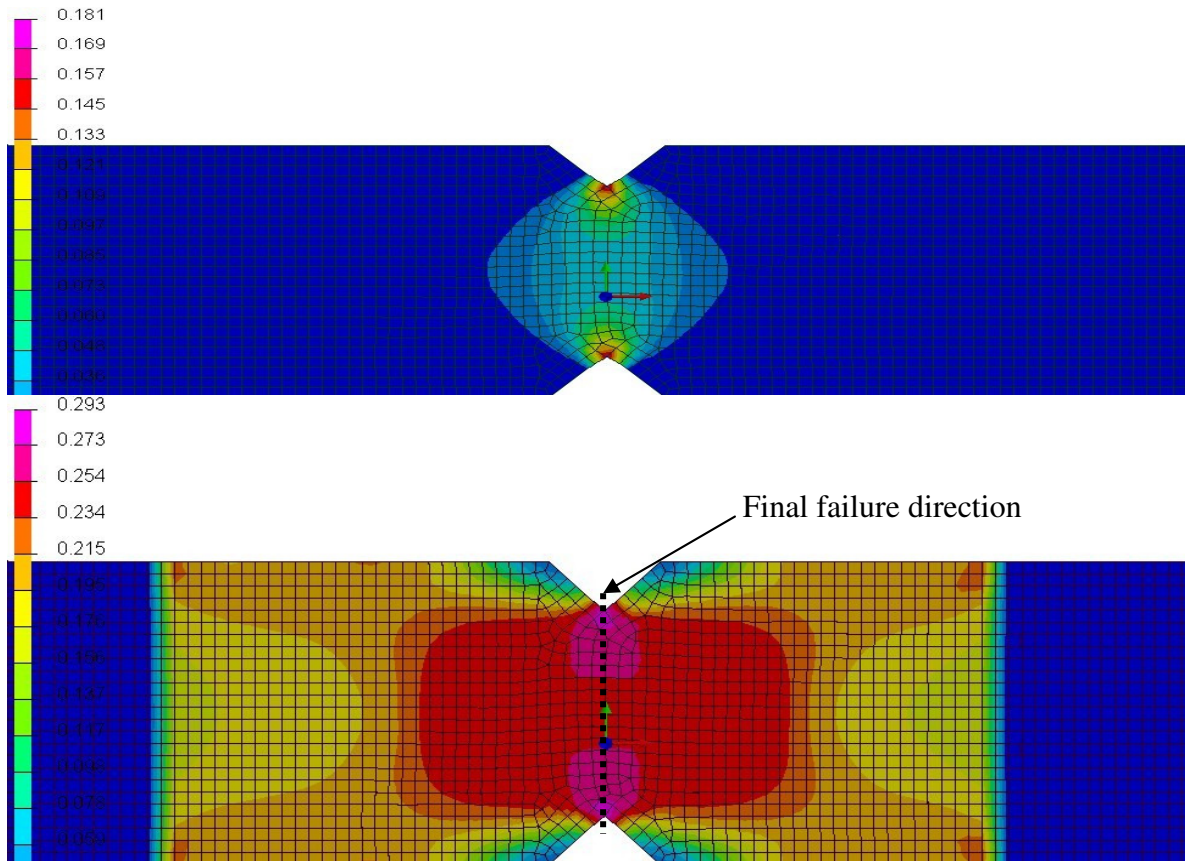


Figure 6.15: Figures of max plastic strain and max Von-Mises stress of V-notch parallel specimen, --- indicate final failure path.

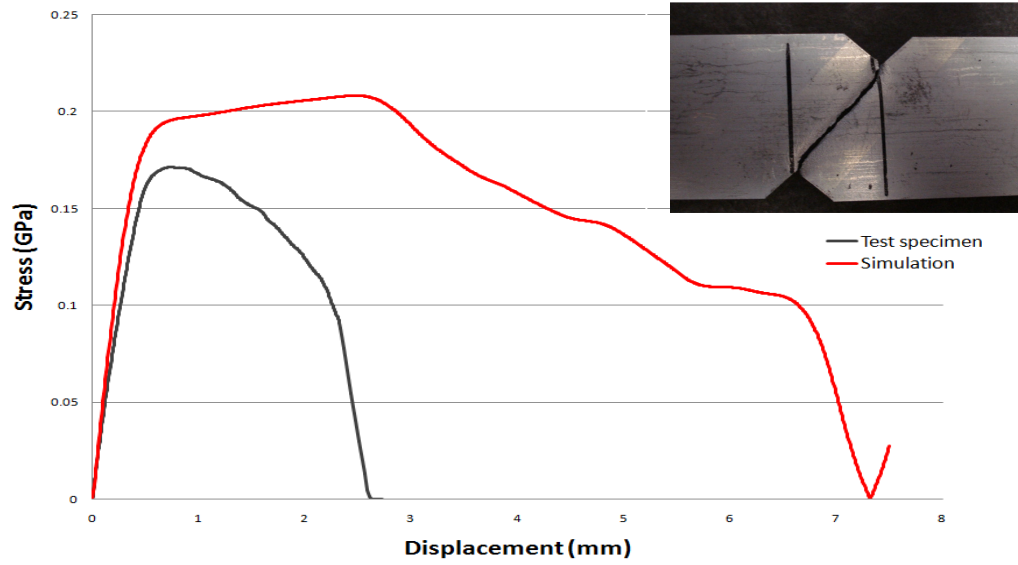


Figure 6.16: Comparison of the simulation with the experimental results for the offset V-notch specimen with 2.4mm thickness

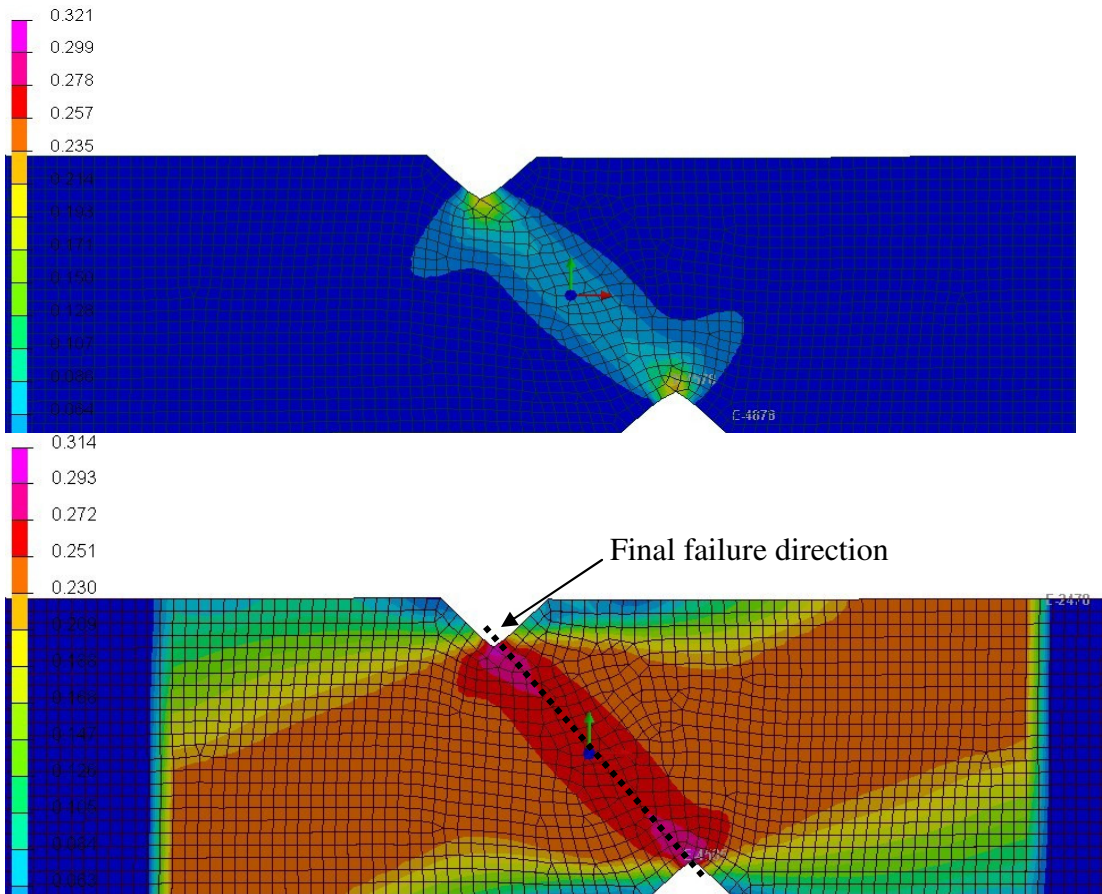


Figure 6.17: Figures of max plastic strain and max Von-Mises stress of V-notch offset specimen

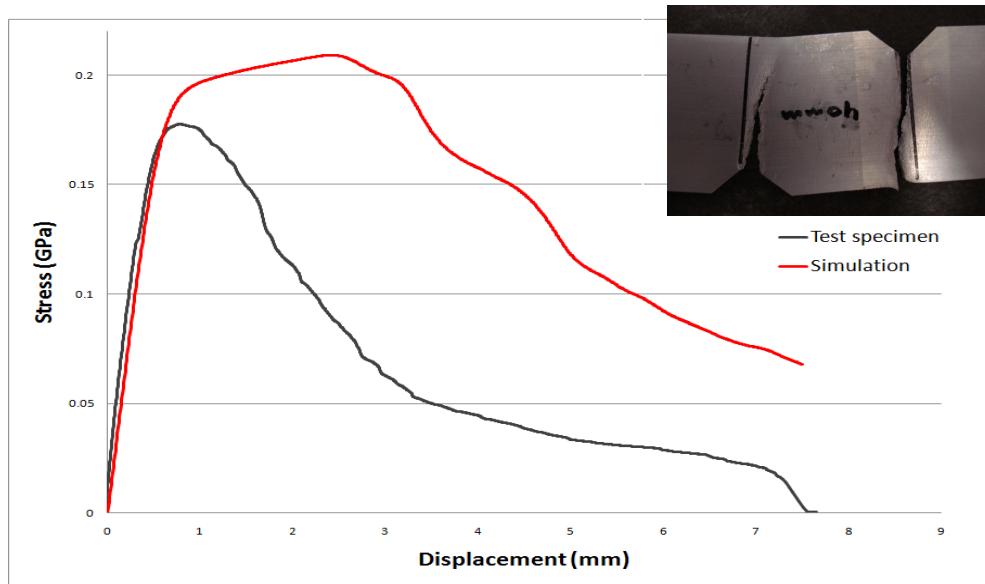


Figure 6.18: Comparison of the simulation with the experimental results for the 42mm offset V-notch specimen with 2.4mm thickness

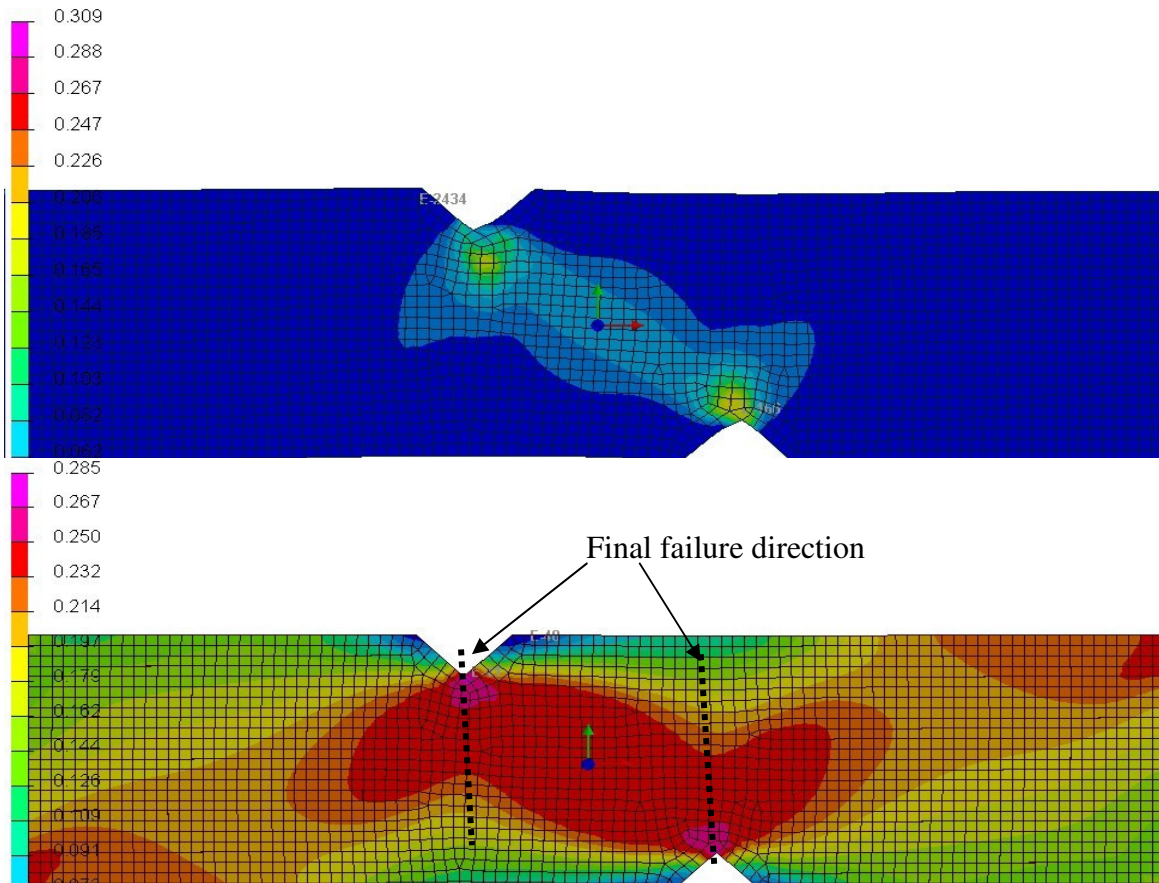


Figure 6.19: Figures of max plastic strain and max Von-Mises stress of the offset 42mm V-notch specimen

6.2.2 Holes in plate specimen

Only two out of four types of holes in plate specimens were tested because of time constrain and priority. The models of two types are simulated and the results are compared with tests. The results are shown in the following figures.

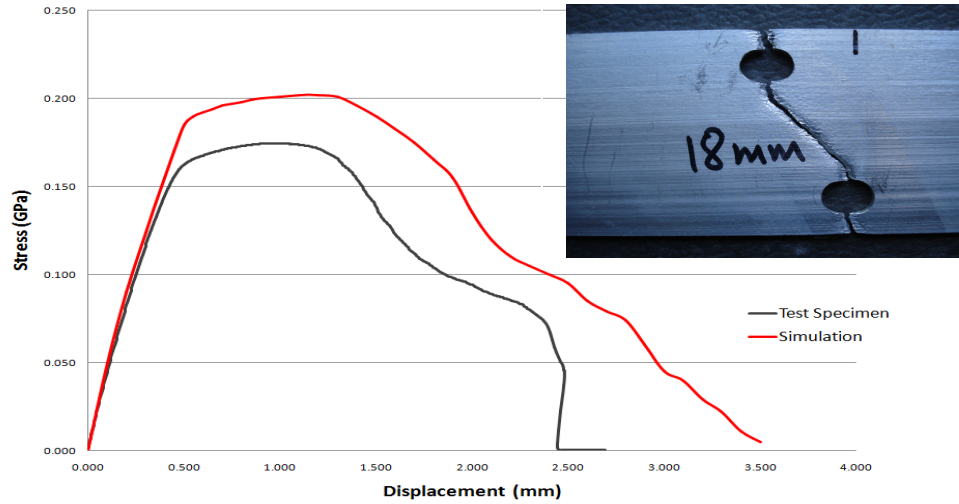


Figure 6.20: Comparison of the simulation with the experimental results for the offset Holes in plate with 2.2mm thickness

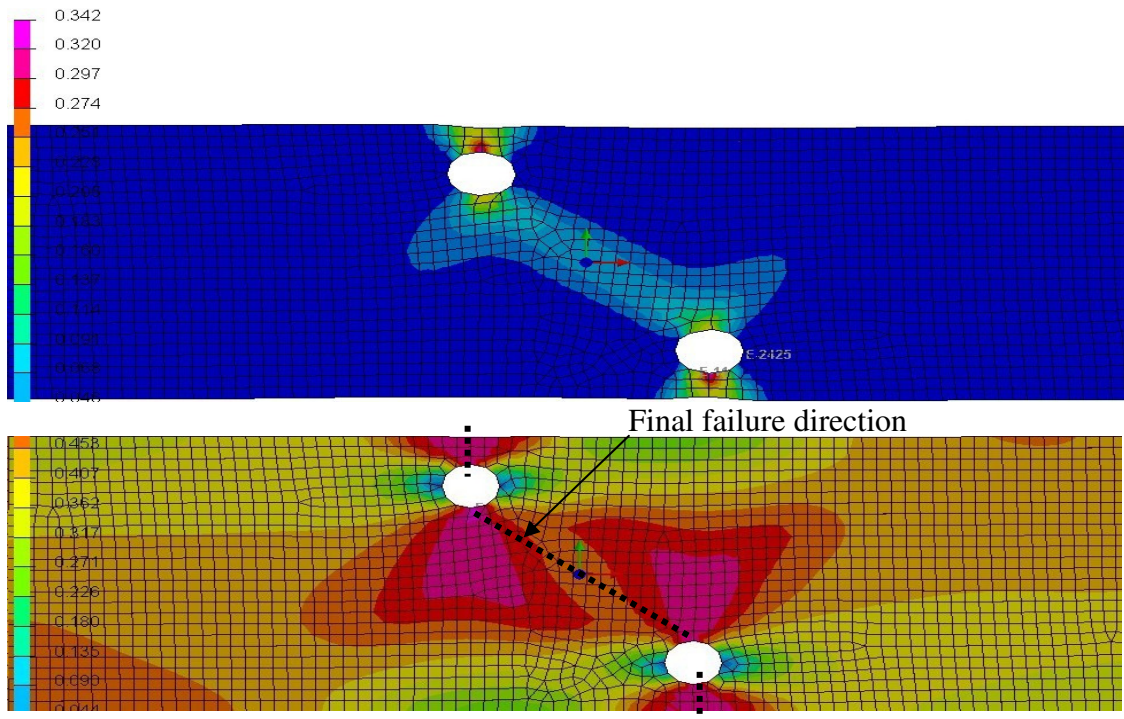


Figure 6.21: Figures of max plastic strain and max Von-Mises stress of hole in plate specimen

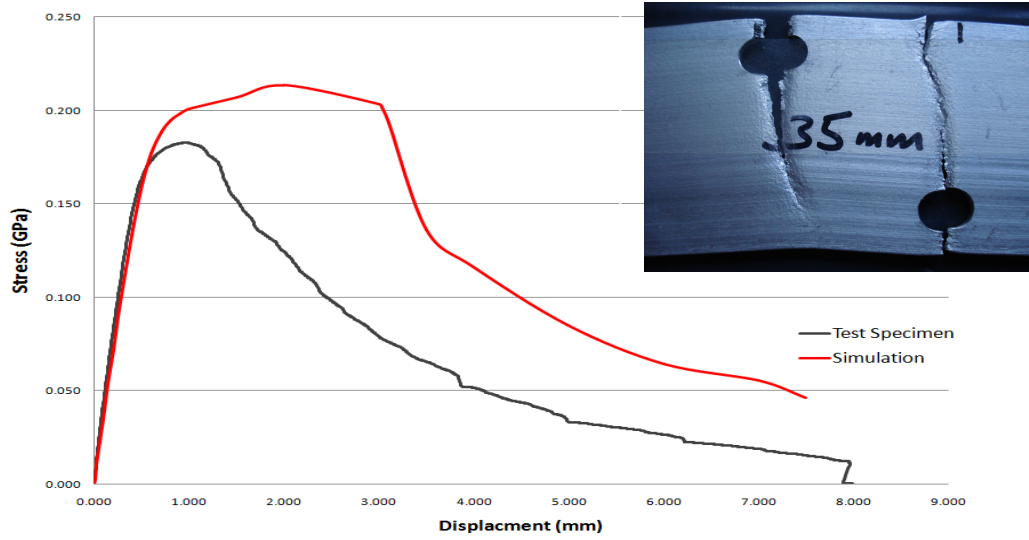


Figure 6.22: Comparison of the simulation with the experimental results for the offset Holes in plate with 2.2mm thickness

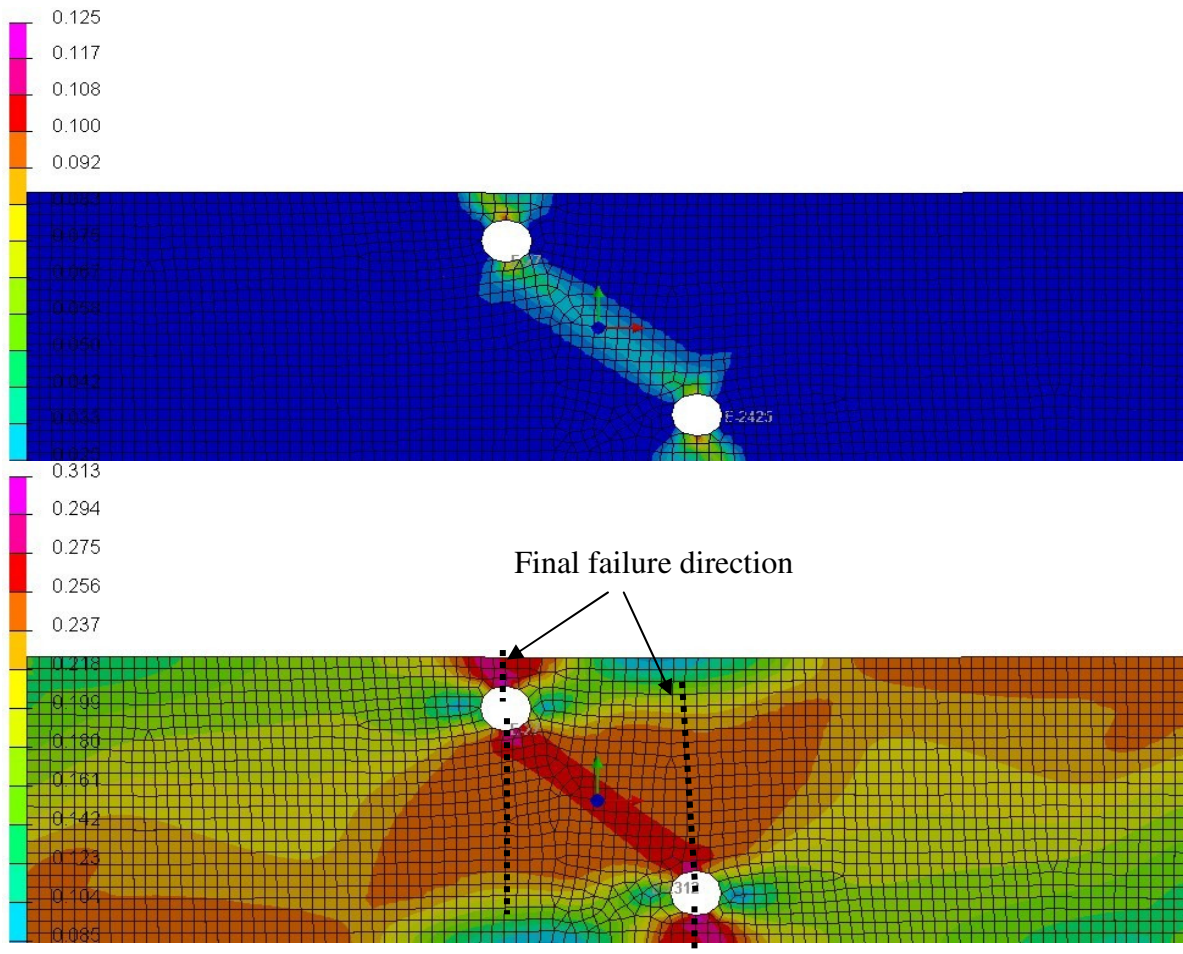


Figure 6.23: Figures of max plastic strain and max Von-Mises stress of hole in plate Specimen 2.2mm thickness

6.3 Solid element simulation

Solid finite elements can be used to discretize bulk materials. Solid elements are three dimensional elements with thickness. Each node of the solid element has 6 degrees of freedom. Several solid elements types are available in PAM-CRASH library. Figure 6.15 shows the 8-node, 4-node and 6-node solid elements that are mostly used in the finite element simulations.

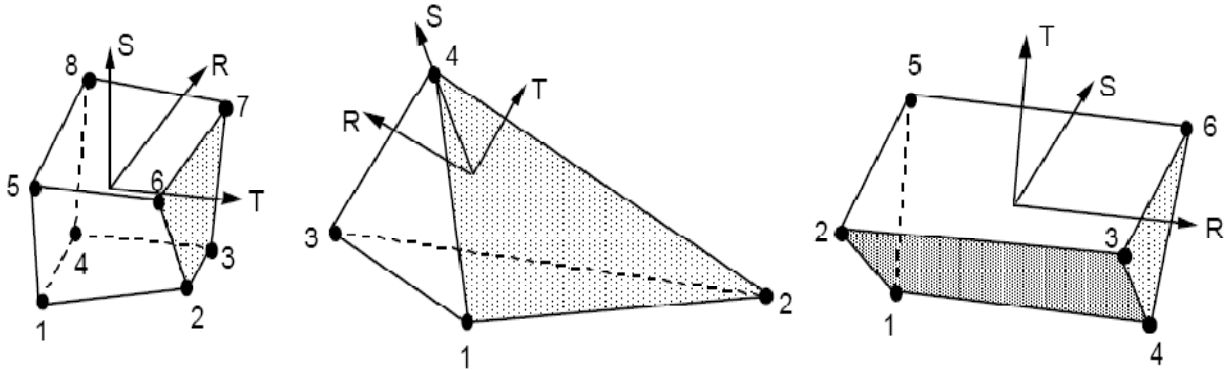


Figure 6.24: Solid elements with nodes and local coordinates system [22].

6.3.1 Methodology

Solid element model has been extracted from the shell element model with few modifications. Solid element mesh is generated using the solid mesh option. For the parallel specimen, solid mesh of full model is created. The reasons of creating this full model solid element mode being; it is smaller in size than the other specimens and secondly, it is used for calibration of the material model. Full solid element models have far more elements compared to full shell element models, this makes the computational time very large and expensive to run on a personal computer. Half solid and half shell elements models have therefore been used instead of full solid element model for the rest of the specimens. The advantage of using half solid and half shell elements is that; it saves considerable amount of computational time without affecting the results.

In order to create half solid and half shell element model, a procedure has been adopted. The area of the specimen which is critical in failure is identified. This area is already meshed with shell elements, so solid elements are created on top of these shell elements by using solid element generation module. Once the solid elements are created the shell elements below are

deleted. Now the simulation model consists of two separate solid and shell elements parts which are not joined together. The tied option is used to join the shell element part and solid element part of the complete simulation model. The shell element part is assigned as master part and solid element part is assigned as slave part of the complete model. After joining, the rest of the procedure of applying boundary conditions and material model is the same as for shell element model described in previous section. Figure 6.16 shows a half solid and half shell element model tied together.

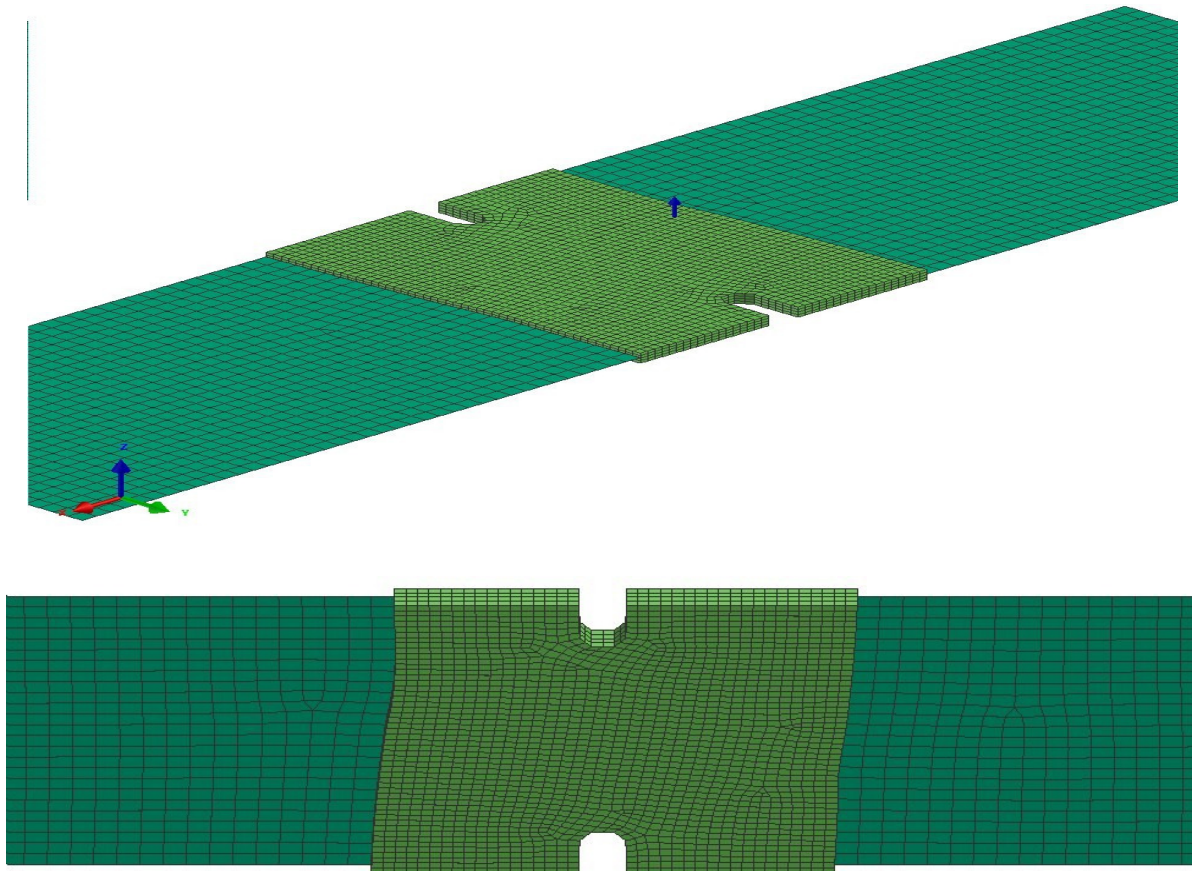


Figure 6.25: Isometric and front view of the half solid and half shell elements simulation model.

6.3.2 Mesh size and boundary conditions

Mesh size for solid element is the same as that of the shell element model, i.e. 1mm element in size. Quadrilateral and triangular planer 2-dimensional elements are used for the meshing of shell element part of the model. Since solid elements are extracted from the shell

elements, size of the solid element is same as that of shell elements with change in depth. Solid elements model mesh consists of 8 node and 6 node solid elements. In most of the models only two layers of solid elements have been used to discretize but number of layers are also increased depending up the accuracy of the results. This has been shown in figure 6.17.

As explained earlier, on left side of the model elements are applied with displacement boundary condition and nodes are restrained in all degrees of freedom. Elements on the right side of the model are also restrained in all directions except in the x-direction. A constant extension force is also applied in the x-direction on the very same right end nodes.

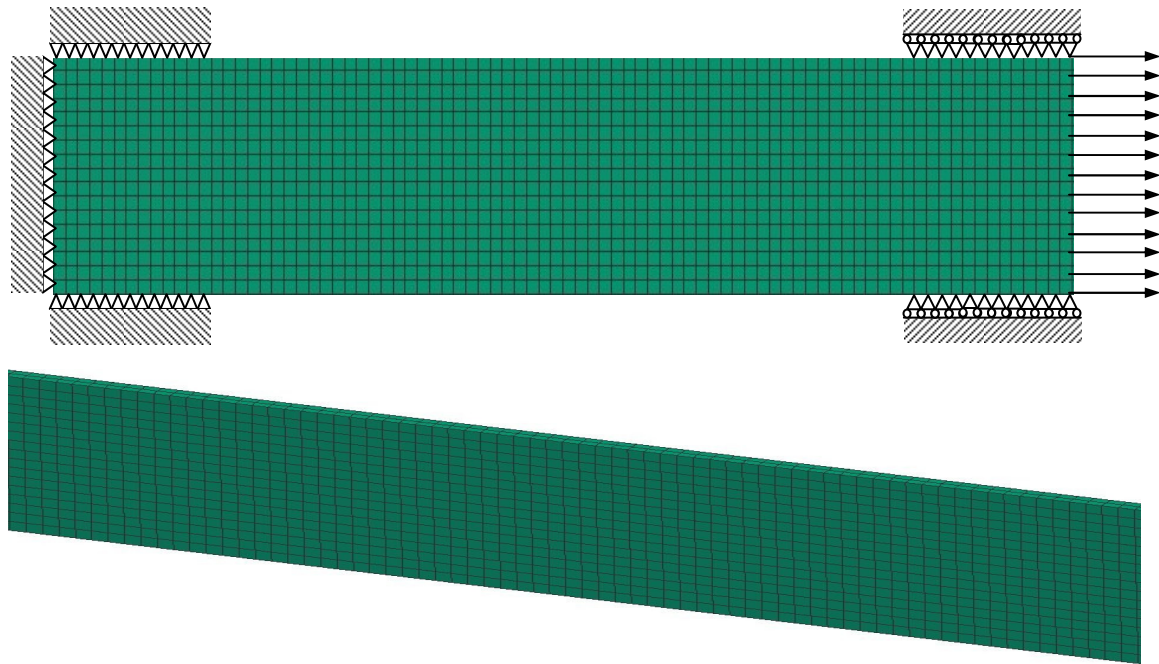


Figure 6.26: Boundary conditions of solid element model and parametric view.

6.3.3 Solid material card

Like shell elements material models, there are wide variety of solid elements material models available in the PAM-CRASH library. Depending on application, material type and material properties an appropriate solid material model must be chosen. For the simulation of solid elements with aluminium alloy properties, two types of material models have been analysed:

- Elastic-plastic material with EWK damage and failure for solid element material type 71 in PAM-CRASH material library [22].
- Elastic-plastic solid with failure material type 16 [22].

The first type of material model is based on ESI-Wilkins-Kamoulakos (EWK) model for ductile fracture that correctly predicts the fracture initiation and eventual propagation within structural components. Fracture occurs when the integrated product of the equivalent accumulated plastic strain and two functions of the local stress distribution (w_1 related to the mean tensile stress and w_2 related to the stress asymmetry) exceed a critical damage value D_c over a critical dimension R_c [22].

$$D = \int w_1 w_2 d\bar{\epsilon}_p \quad (6.3)$$

$d\bar{\epsilon}_p$ = equivalent plastic strain

w_1 = hydrostatic pressure weighting term given by $\left(\frac{1}{1+aP}\right)^\alpha$

P = hydrostatic stress

w_2 = deviatoric pressure weighting term given by $(2-A)^\beta$

$$A = \text{Max} \left(\frac{s_2}{s_3}, \frac{s_2}{s_1} \right) \quad s_1 \geq s_2 \geq s_3 \quad \text{are the principle stress deviators}$$

Further details of this model have already been explained in section 3.4.4. The coefficients for this model are calibrated using certain set of special tests. These tests constitute a systematic experimental campaign spanning smooth cylindrical and notched cylindrical specimens loaded to fracture. Audi provided the coefficients predicted by Wilkins or other for the simulation and later they have been calibrated according to the quality of results. Figure 6.18 shows the material card for EWK model. Wilkins coefficients are highlighted in the figure.

\$#	TITLE								
	NAME Elastic_plastic_solid							Wilkins coefficients	
\$#	G	SIGMA_Y	Et	BLANK	BLANK	BLANK	STRAT1	STRAT2	
26.54	CURVE		0.				0.	0.	
\$#	K	Dc	Rc	Plim	ALPH_EPST	BETA_EPSS	H		
57.5	0.3	2.	0.48	1.1	0.75				
\$#	LC1	LC2	LC3	LC4	LC5	LC6	LC7	LC8	
2	0	0	0	0	0	0	0	0	

Figure 6.27: EWK solid element material card

Once the model has been calibrated for the parallel specimen by adjusting Wilkins parameters, it is then used for the other specimens. Comparison of simulation results and test results showed poor accuracy. Because the effects of anisotropy and plasticity are not included in the material model and these could be the reasons behind inaccurate simulation results, so another model has been chosen to predict the results.

Material model type 16 is an elastic-plastic model for FEM solid element simulations. It has been designed to describe the deformation of metallic materials during forming and crash loading. It provides a variety of material phenomena such as:

- Elastic-plastic behaviour
- Yield criteria
- Hardening laws
- Failure models

The main features of the elastic plastic formulation of material model are:

- Decomposition of rate-of-deformation tensor D into elastic and plastic parts.
- Linear isotropic hypoelastic stress rate relation characterized by bulk and shear moduli (K, G) respectively
- Associative flow rule

- Yield stress dependent on effective plastic strain and effective plastic strain rate.

As explained before, the material used for the testing is anisotropic with its properties dependent on direction. The yield criteria included in the material model are Orthotropic Hill 1948 yielding functions and orthotropic Barlat’s 1991 yielding function, of which Barlat’s 1991 yielding function has been used to replicate the anisotropic behaviour.

Two different failure and damage criteria are incorporated in the failure module of the material model:

- Maximum plastic strain
- Rupture model

Both of these criteria may be combined with tabulated damage function illustrated in figure 6.19, which reduces the yield stress to equation 6.4. This curve shows that damage does not influence the elastic properties of the material.

$$Y_{damage} = Y_{undamage} (1 - d) \tag{6.4}$$

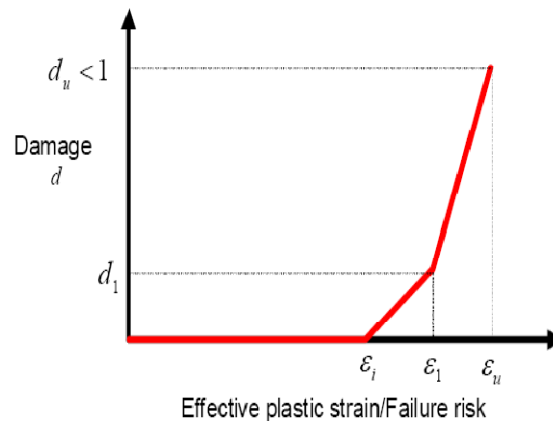


Figure 6.28: Relationship between damage function (failure criteria).

Damage calculation for the two failure criteria is different from each other. In maximum plastic strain criterion; the damage function abscissa of the above figure is effective plastic strain of the material. If no input damage function is defined then no damage is calculated. For the rupture model the damage function on the abscissa is equal to failure risk, and if no input damage function is defined then damage is calculated automatically.

Rupture model of damage and failure criterion is used to predict failure in the specimens. Elements are eliminated by specifying the final damage D_u value smaller than 1 so that elements provide some resistance to deformation in the end phase. Figure 6.20 shows the material card for elastic plastic solid material model.

RUPMO /	1	6						
NAME	Rupture model							
	0.3	2.0	0.40	1.1	0.20	0.34		
\$#	IDMAT	MATYP		RHO	ISINT	ISHG	ISTRAT	IFROZ
MATER /	2	16	2.753E-006	0	0			
\$#	TITLE							
NAME	Elastic-Plastic Solid							
\$#	G	SIGMA_Y	Et	ALPHA	BLANK	BLANK	STRAT1	STRAT2
	25.8	CURVE	0.55		2		0.	0.
\$#	K							
	55.8	1	1.00368	1.00434	1.0	1.0	1.004024	8.0
\$#	LC1	LC2	LC3	LC4	LC5	LC6	LC7	LC8
	2	0	0	0	0	0	0	0

Figure 6.29: Elastic-plastic solid element material card.

6.3.4 True stress-strain curve

During tensile testing for a ductile material the cross section area of the specimen continuously decreases until it breaks. Materials with high reduction in cross section area are highly ductile whereas brittle materials exhibit little or no reduction in cross section area. The engineering stress-strain curve calculated using the original cross section area and dimension of the specimen, do not give a true indication of the deformation characteristics of a material, as these dimensions change continuously during the test. If engineering stress-strain curve is used in the material curve it will give false results, thus a stress-strain curve which gives the measure of instantaneous deformation with change in dimensions is needed [23].

The true stress-strain curve has been produced by using engineering stress and strain calculated for the parallel specimen. The relationship for true stress and strain is given by:

$$\sigma_T = \sigma_E(1 + \varepsilon) \quad \text{and} \quad \varepsilon_T = \ln(L/L_0) \quad (6.5)$$

The other method that has also been employed to find the true stress-strain curve is by the analysis of data captured from the optical strain measurement testing. This data is processed in MATLAB and true stress-strain curve for parallel specimen is obtain as shown in figure 6.21. This curve is more reliable than calculating curve from engineering stress and strain.

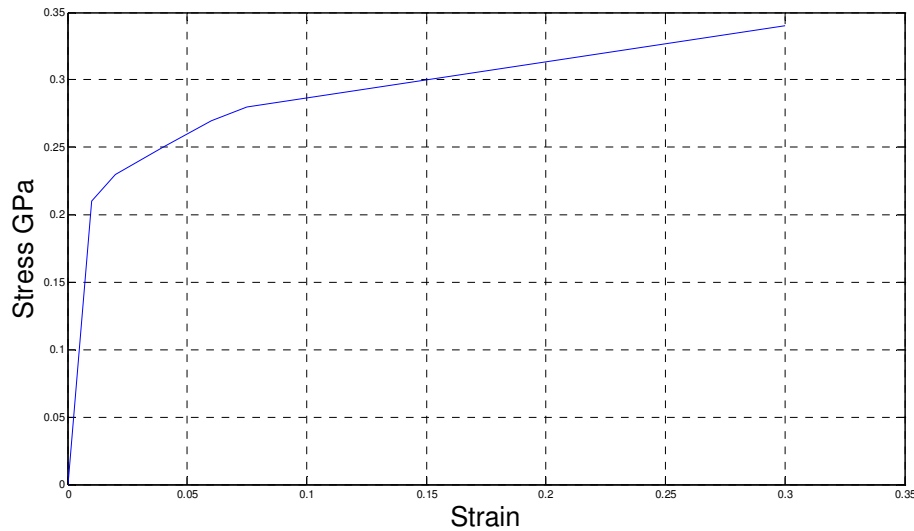


Figure 6.30: True stress-strain curve obtained from optical strain testing.

To use the curve in the material card, it is necessary to use plastic part of the true stress-strain curve while for elastic part, only Young's modulus of the aluminium alloy is needed to complete the material card.

6.4 Solid element simulation results

Models of solid element for different specimens have been created and simulations are run with PAM-CRASH. The material model used in the simulation is anisotropic plastic with EWK rupture model. As explained earlier, the output results are generated by defining the reaction force at the fully restrained end of the model and the curves are produced in PAM-

VIEWER. Later these simulation curves are compared with tensile test results. Figure 6.22 shows the comparison of simulation and tensile test result of full solid model of parallel specimen.

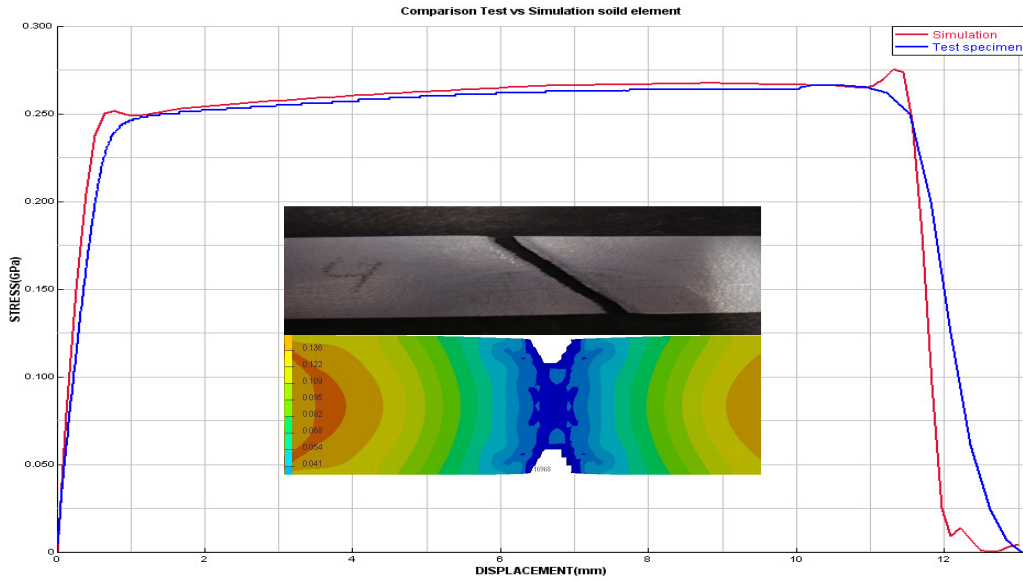


Figure 6.31: Comparison of the simulation solid element with the experimental results for the parallel specimen 2.4 mm thick

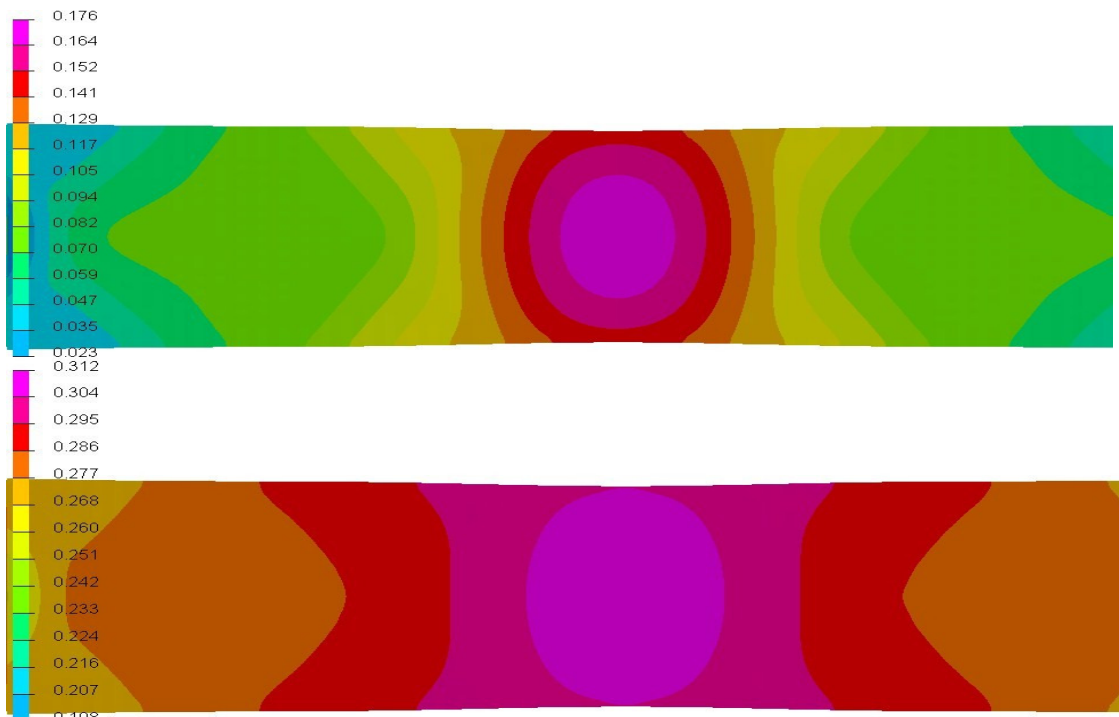


Figure 6.32: Figures of max plastic strain and max Von-Mises stress in parallel specimen

6.4.1 Notched specimens

A series of simulations have been produced for U-notch and V-notch specimens. Simulation results are generated for specimen and then compared with corresponding tensile test result of the specimen. These results are presented in the following figures.

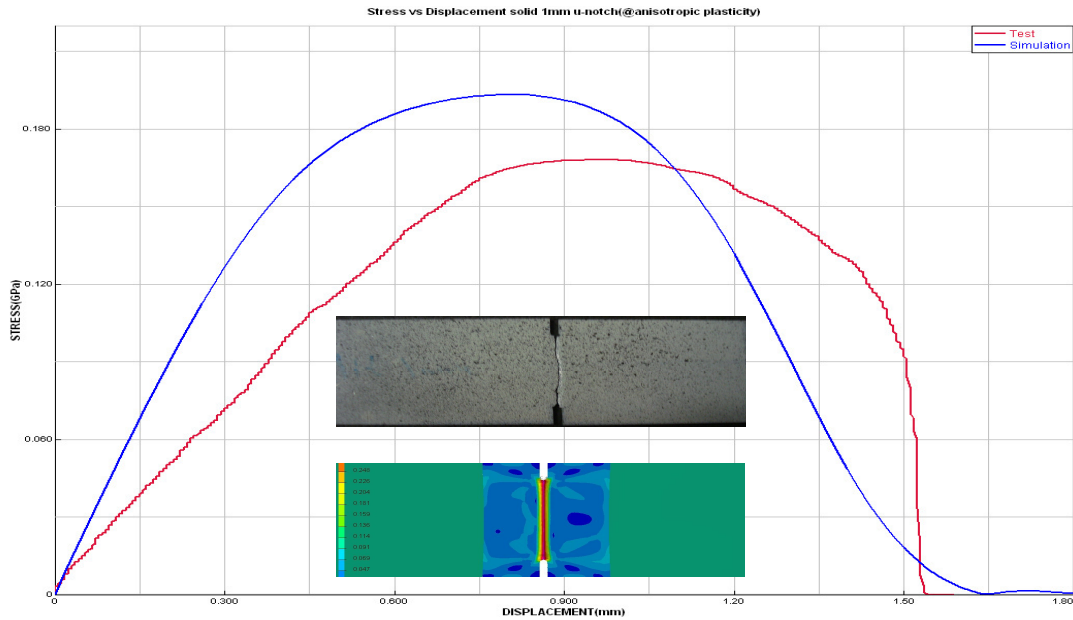


Figure 6.33: Comparison of the simulation with the experimental results for 1mm diameter slit specimen of thickness 2.5 mm

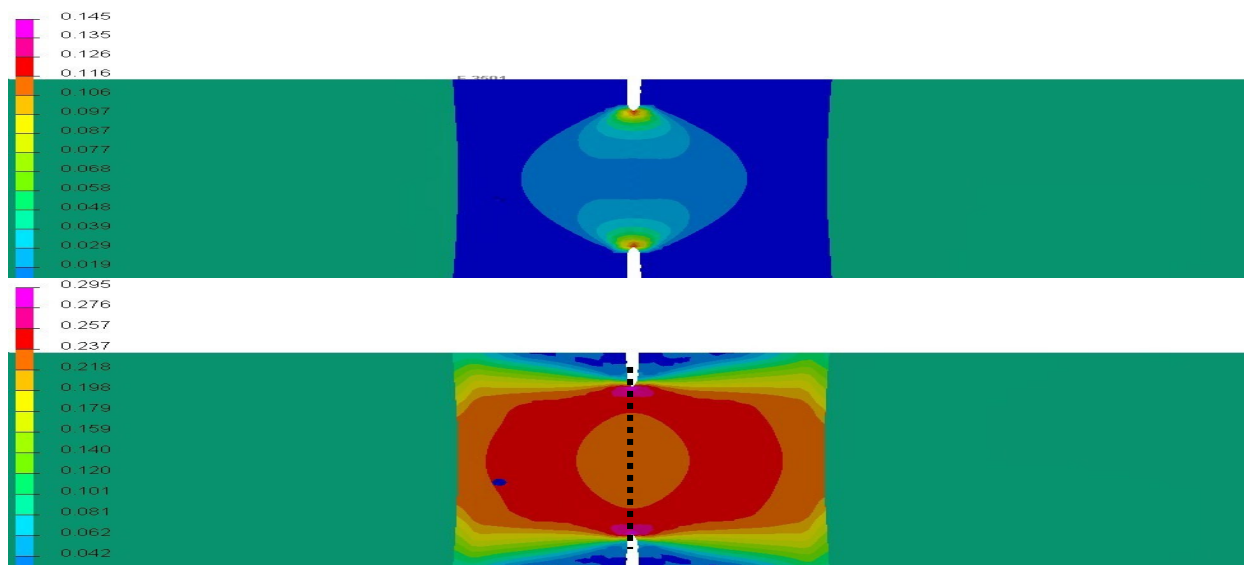


Figure 6.34: Figures of max plastic strain and max Von-Mises stress in 1mm dia-slit specimen

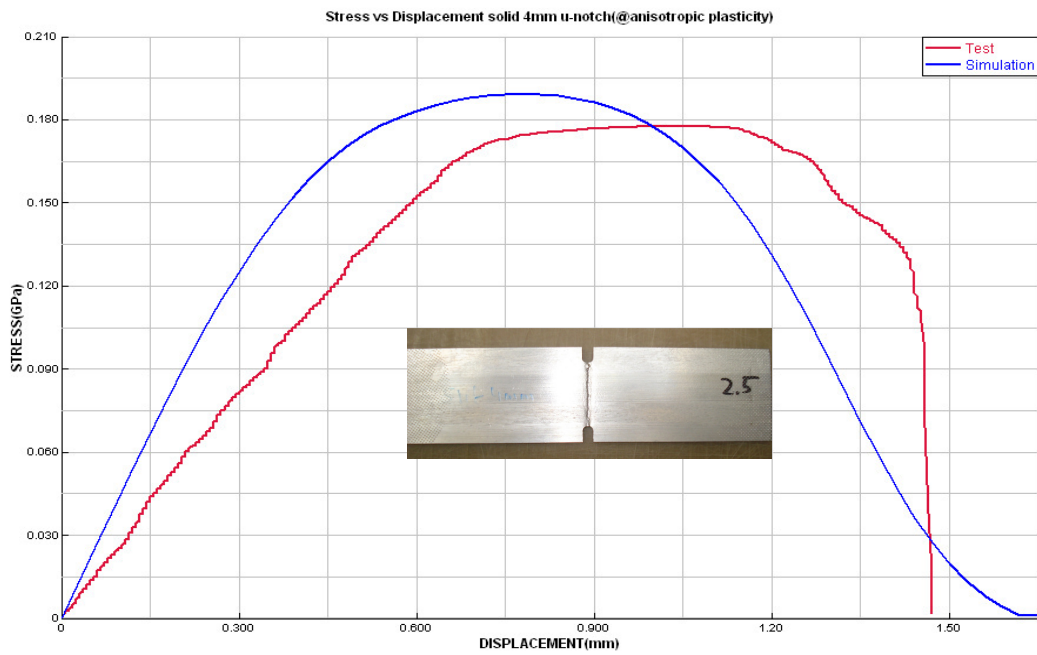


Figure 6.35: Comparison of the simulation with the experimental results for 4mm diameter U-notch specimen 1.8 mm thickness.

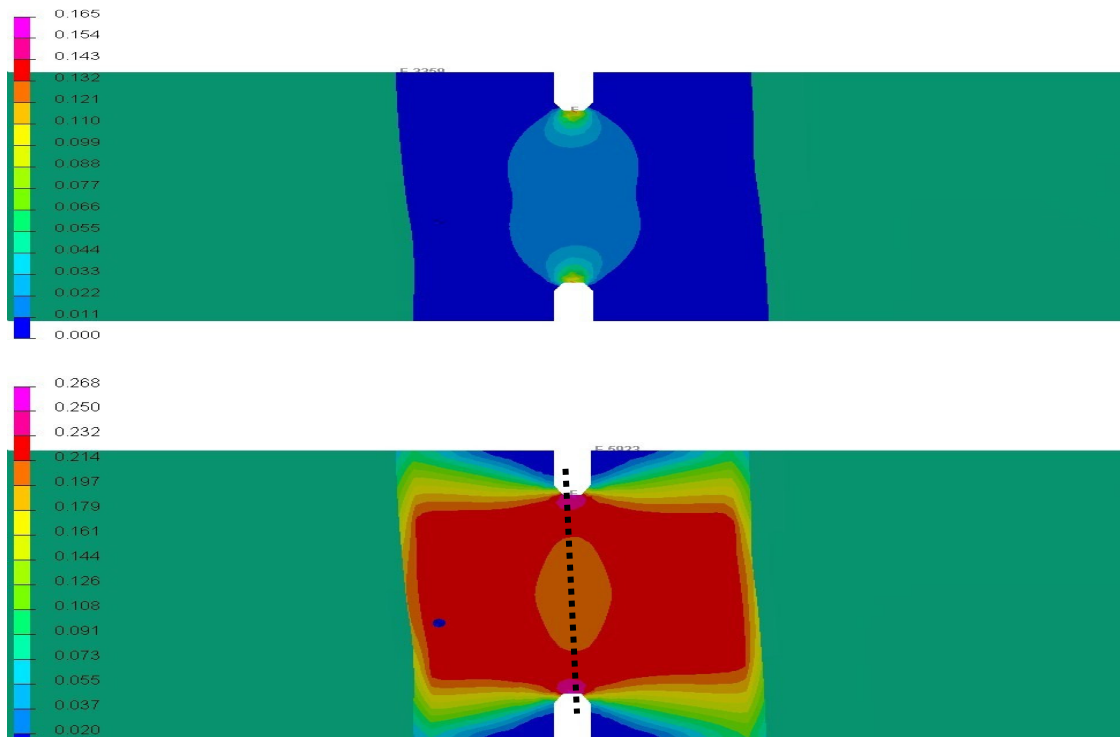


Figure 6.36: Figures of max plastic strain and max Von-Mises stress in 4mm diameter U notch specimen

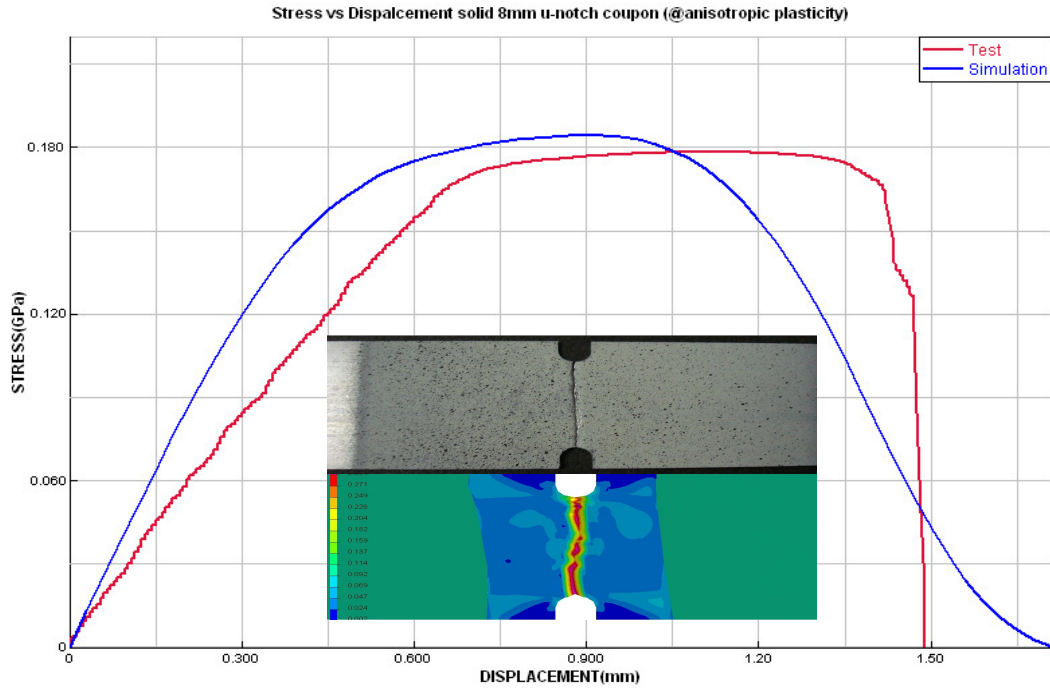


Figure 6.37: Comparison of the simulation with the experimental results for 8mm diameter U-notch specimen 1.8 mm thickness

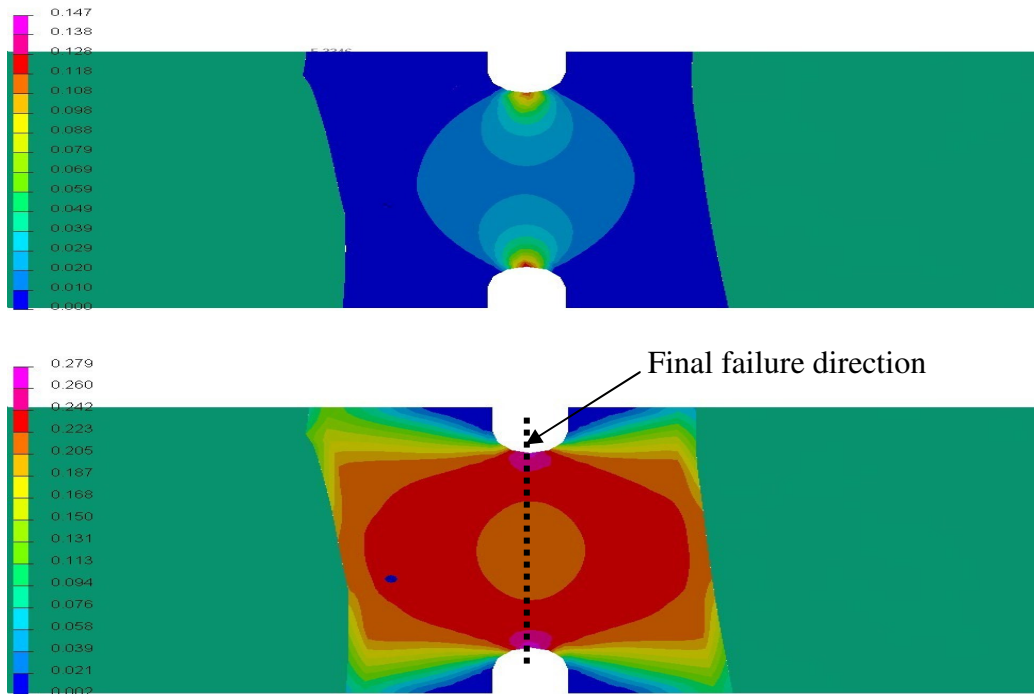


Figure 6.38: Figures of max plastic strain and max Von-Mises stress in the 8mm diameter U notch specimen

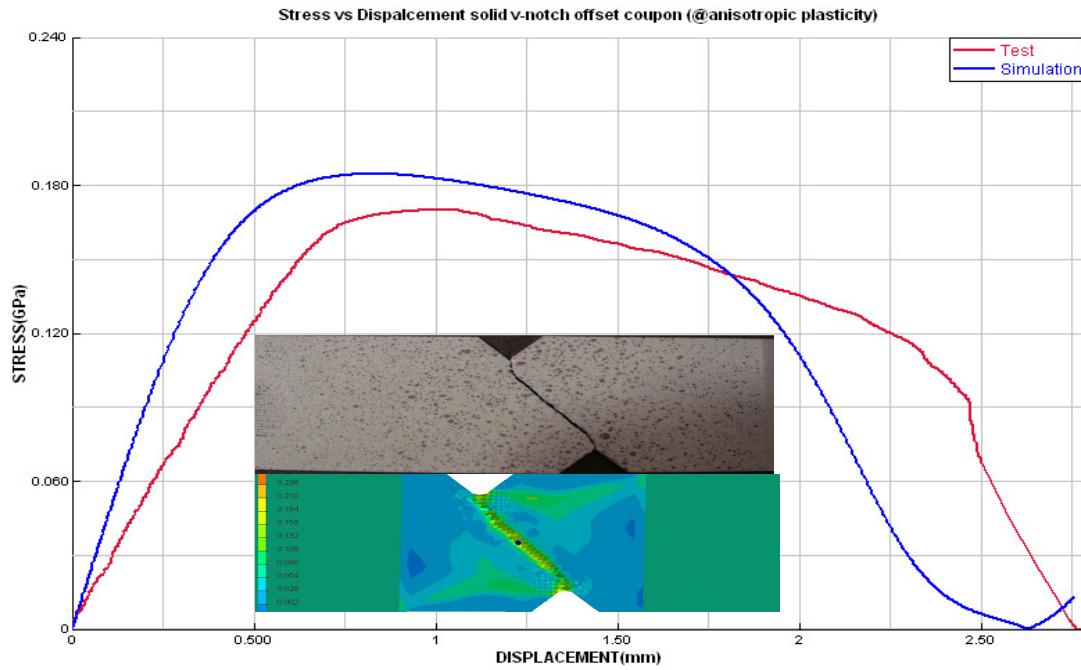


Figure 6.39: Comparison of the simulation with the experimental results for offset V-notch specimen 2.4 mm thickness

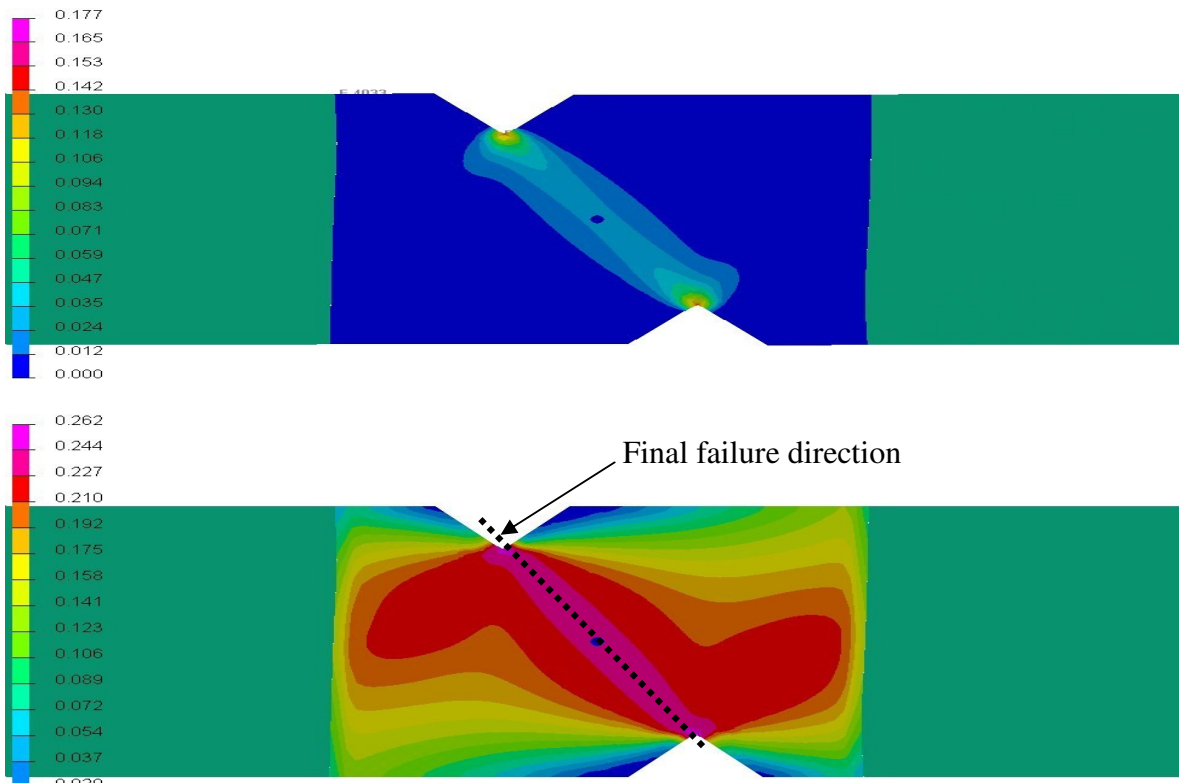


Figure 6.40: Figures of max plastic strain and max Von-Mises stress in the offset V notch specimen

6.4.2 Holes in plate

Two simulations have been generated for the holes in plate type specimens. The simulation results and tensile test results are compared and shown in the following figures.

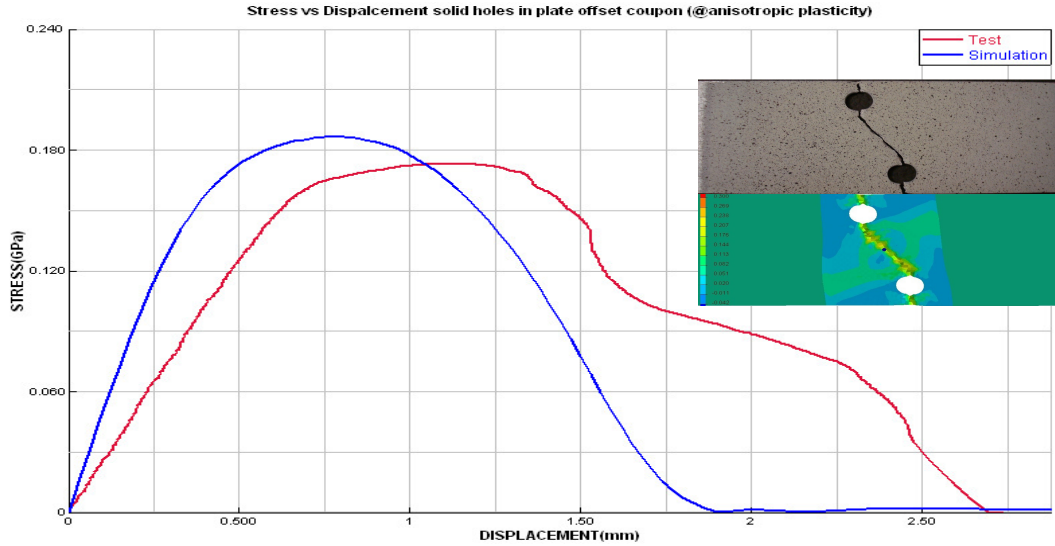


Figure 6.41: Comparison of the simulation with the experimental results for the 16 mm Offset hole in plate specimen 2.2 mm thickness

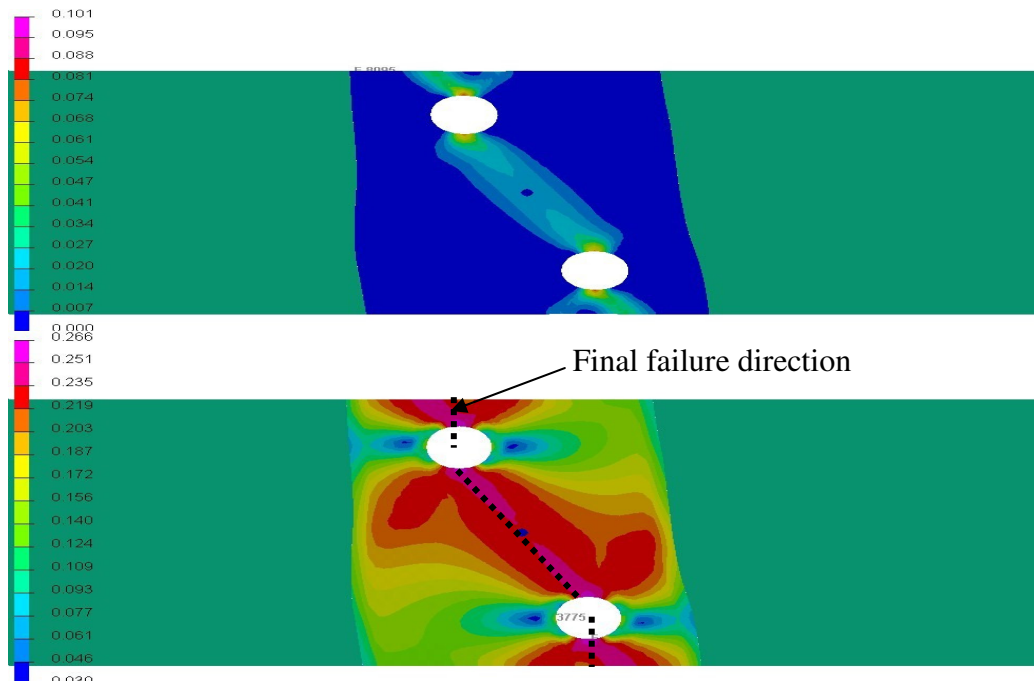


Figure 6.42: Figures of max plastic strain and max Von-Mises stress in hole in plate specimen

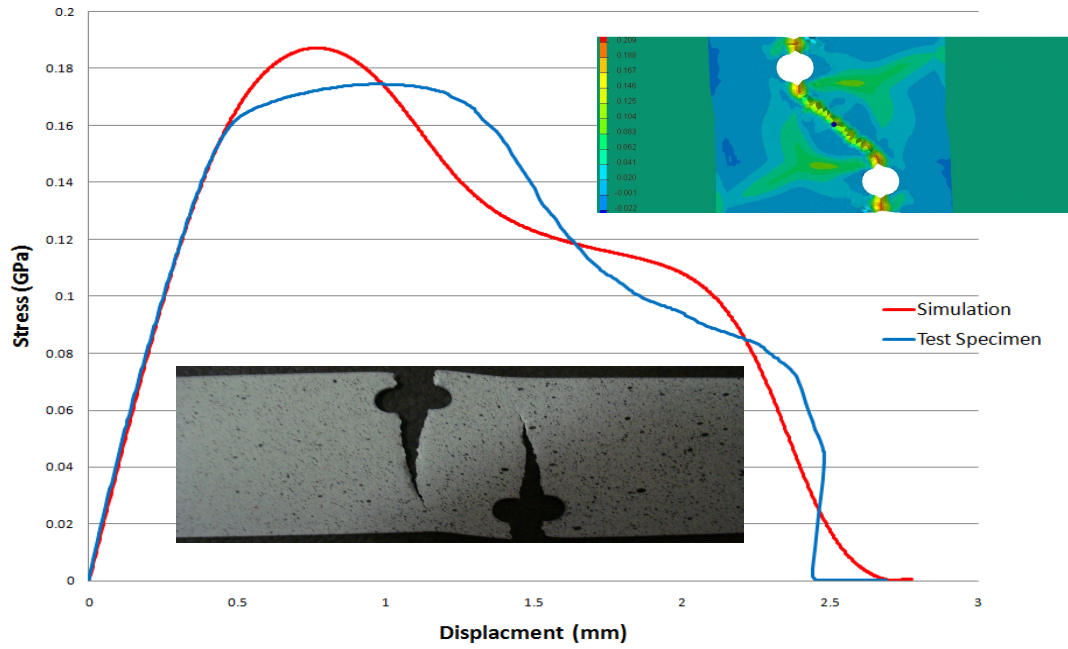


Figure 6.43: Comparison of the simulation with the experimental results for the 32 mm Offset hole in plate specimen 2.2 mm thickness

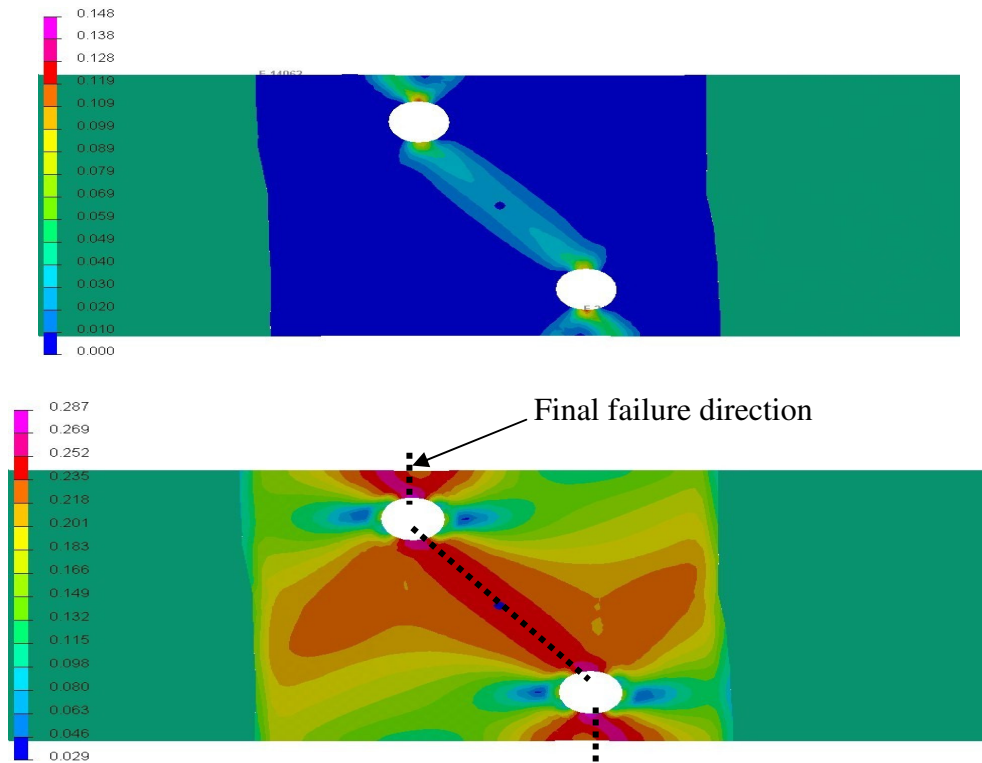


Figure 6.44: Figures of max plastic strain and max Von-Mises stress in the 32 mm Offset hole in plate specimen

6.5 Discussion of results:

Fracture of the 35 mm wide parallel specimen occurred because of a combination of diffused and localized necking phenomena. In un-notched plain specimen, where the width of the specimen is much greater than the thickness, diffuse necking will generally occur. Diffuse necking can continue until specimen fractures, but it is far more likely that a second instability process called localized necking will be initiated. This second neck is much narrower, with a width about the same as the thickness of the specimen, and usually inclined at an angle across the specimen, as shown schematically in figure 6.28 [23].

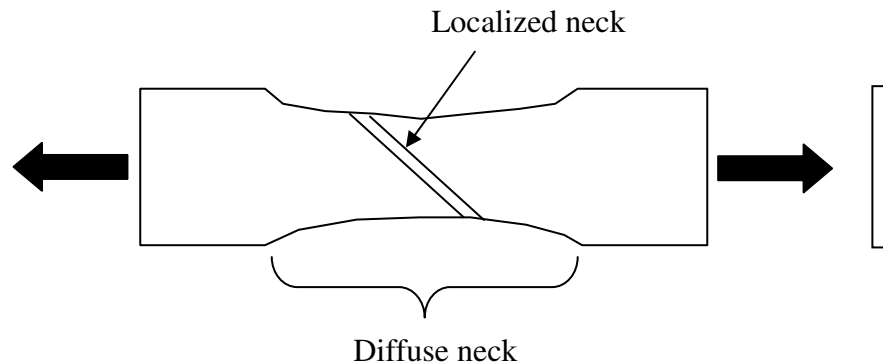


Figure 6.45: Diffuse and localized necking

In the case of the parallel specimen, diffuse and localized necking have occurred and the fracture has been caused by shear.

In the case of the notch specimen, the phenomenon for fracture is different to the parallel specimen. When the specimen is loaded in tension necking occurred in the notch area. The neck produced a tri-axial stress state in the centre of the specimen, which promotes void nucleation and growth. As the specimen is further strained coalescence of the voids will occur resulting in the formation of a local fracture. The outside edges of the specimen contain relatively few voids because the hydrostatic stress is lower than in the centre. The flaw will produce shear bands at 45° from the tensile axis. This provides sufficient plasticity to nucleate voids in smaller particles, which results in total fracture. Due to the 45° angle of fracture, failure in this region was from a combination of Mode I and Mode II loading.

The simulation results of shell element material model have been presented in section 6.2. Figure 6.6 shows the parallel specimen results demonstrating that numerical simulation result and test result match with great accuracy. This indicates that the FLD failure criterion accurately predicts the failure of the parallel specimen. The same criterion is used for notch specimen and results have been extracted. After carefully interpreting the results, it has been found that test results and simulation results do not match and show poor accuracy. For most of the specimens the displacement to failure is much larger in simulation results as compared with the test results. In some cases the maximum stress values are also higher than that of test results. Mesh size was also refined to check its dependence on the results, but was not found to have significant effect on the accuracy of the results. In a few simulations the FLD curve was modified and it showed an improvement in the results. FLD initially used has been developed particularly for the type of aluminium alloy under investigation, using a calibrated FLD to get results would be wrong for loaded areas without notches.

Solid element numerical simulation results have been presented in section 6.4. Different macro-mechanical failure models have been used to simulate solid elements model. The parallel specimen simulations was found to give very good results, and perfectly matched with tensile test results as shown in figure 6.22. Two material models have been tested for parallel specimen. The DcRc Wilkins damage model was applied for 4mm diameter U-notch specimen and results are compared with the experimental finding. It was found that the results are not accurate for numerical simulation and the model is needed to be refined for better results. The DcRc model does not consider the anisotropic plastic behaviour of the material which resulted in the deviation of results. PAM-CRASH material model library supports the EWK rupture model, this model has been developed from Wilkins damage model in combination with anisotropic plasticity as explained earlier. The same U-notched specimen was modeled with EWK rupture model to get the simulation results, the coefficients of the rupture model were modified to get reasonable results for other types of notch specimens.

The results of notch specimens when compared with corresponding test results showed acceptable pattern. With a couple of exceptions the model accurately predicts failure in notch and hole specimens. The results can be improved by using full solid mesh model and by using finer mesh.

The shell element model and the solid elements model were calibrate using specimens that failed under mixed Mode I/ Mode II loading conditions. Most of The shell element simulation model failed under the Mode I, which is the same during tensile testing. The solid element model of the parallel specimen failed in pure tensile model while the test specimen failed in the pure shear mode.

Chapter 7 : Conclusion

The prediction of failure within automotive structures is an important tool to assess the crashworthiness of vehicles manufactured from aluminium alloy. The purpose of this thesis was to study the failure and crack propagation behaviour of aluminium alloy structure based on experimental investigation and numerical simulations. An important aspect of this research was to compare the results from the experimental investigation and Finite element analysis to see if it is possible to obtain similar results. The success in this manner depends both on the evaluation methods of the experiments and accuracy of numerical model used in the FE code. A detailed study concerning different FE models with different geometries and assumptions under static loading conditions was performed. The modeling approaches and the issues related to different FE models were also studied in detail.

The results from experimental investigations enabled the failure of notched and un-notched specimens to be determined. Use of modern experimental techniques helped in studying the behaviour of failure under uniaxial loading, how a crack initiates at stress concentration (notches) and how cracks propagate through the structure. The experimental results has helped to serve as a primary step towards generation of an accurate FE model and to validate the numerical results.

The data gathered from experimental investigation helped to make precise geometric models of each specimen. It became possible to produce an accurate meshed representation of the parallel and notch specimens. Two different types of material models were created using shell elements and solid elements. The simulation results for both types of material models were obtained from finite element analysis performed with PAM-CRASHTM. Shell elements simulation is very important from commercial point of view. Shell elements simulations are popular in the automotive industry because shell elements are computationally efficient with little compromise in accuracy. Due to the importance of shell elements, a shell element model was used in this thesis with anisotropic plasticity and a FLD failure criterion. The results obtained for the parallel specimen showed good agreement with experimental findings. However, for notched specimens the accuracy of the results was poor. FLD failure criterion was unsuccessful in predicting the failure of the specimens with notches and stress concentrations.

FLD was modified for notch specimen but later it was rejected as the original FLD was particularly produced for aluminium alloy used in this project. FLD failure criterion is used for 2D model – stress concentrations at notches is a 3D effect (plastic flow, tri-axial stress distribution), primarily because of this reason FLD criterion failed for notched specimens. Another argument could be that the FLD was not produced considering all major and minor strains of aluminium alloy.

Solid elements simulation was created to investigate more advance macro-mechanical material models. Solid elements are computationally inefficient as compared with shell elements but have very high accuracy in producing results. Two material models, DcRc Wilkins damage material model and anisotropic plasticity EWK¹ rupture models were investigated independently. Both models gave very accurate results for parallel specimen. For notched specimens, it was EWK rupture model that was accurate enough to predict the failure of specimens. EWK rupture model was calibrated for all types of notch specimens and with couple of exceptions it worked with great precision. The model was successful in accurately predicting the failure in notched and un-notched specimens.

Finally, a comparison was made between shell elements and solid elements models for predicting the point of crack initiation and the path of crack propagation. It was found that both models were quite successful in predicting these phenomena. The results were verified with the experimental investigations.

7.1 Scope for future work

There is lot of room for improvement and further research in this project. The mechanical testing of the specimens has been conducted under static loading. Dynamic loading would be more relevant in order to predict the failure in context of vehicle crash. The accurate prediction of failure under different loading conditions is desirable. Testing must be carried out on specimens under different loading conditions. Effect of strain rate and strain hardening should be studied.

¹ The EWK model is a further derivation of the original Wilkins DcRc model that has been implemented in PAM-CRASHTM by ESI

In finite element modeling, mesh dependency is well known problem for failure and damage modeling due to static softening behaviour. Therefore it would be beneficial to study a particular mesh size which gives accurate results. Since the shell element FLD material model was unsuccessful in predicting the failure of specimens, other material models could also be investigated. Aluminum alloy consists of crystalline structure, study of fracture and slipping at micro level is important. Gurson model for damage and plastic flow mainly deals with the defects and dislocation in the crystalline structure of material. Further research should be carried out in this area and specimens should be analyzed using Gurson's damage material model.

EWK rupture model coefficients and Barlat's anisotropic plasticity coefficients were calibrated on trial and error basis for notched specimens. A more professional approach should be adopted by using modern optimization techniques.

Chapter 8 : References

- [1] T. SAKURAI, The Latest Trends in Aluminum Alloy Sheets for Automotive Body Panels, Aluminum Sheets Department Moka Plant, Aluminum & Copper Company
- [2] www.eaa.net , aluminium in cars, European aluminium association.
- [3] J. Hirsch, Automotive Trends in Aluminium - The European Perspective, Materials Forum volume28 - Published 2004
- [4] Prakash M. Dixit, Uday S. Dixit, Modeling of Metal Forming and Machining Processes by Finite Element and Soft Computing Methods, 2008 Springer-Verlag London Limited
- [5] Omri Rand and Vladimir Rovenski, Analytical Methods in Anisotropic Elasticity with Symbolic Computational Tools, 2007 Birkhäuser Boston
- [6] Hill, R. (1948). A theory of the yielding and plastic flow of anisotropic materials. Proceedings of the Royal Society of London A 193, pp. 281-297.
- [7] Barlat, F; Lege, D.J.; Brem, J.C. (1991). A six component yield function for anisotropic materials. International Journal of Plasticity 7, pp. 693-712.
- [8] Z. Marciniak, J.L. Duncan, S.J. Hu. Mechanics of Sheet Metal Forming, 2002 Butterworth-Heinemann oxford
- [9] E.E. Gdoutos, Fracture Mechanics an Introduction, 2005, 2nd edition, Springer Netherlands
- [10] O.Vardar, Effect of single OL in FCP. Engineering Fracture Mechanics, V-30, n-3 (1988), pp. 329-335
- [11] Sih, G.C., Some Basic Problems in Fracture Mechanics and New Concepts, Eng. Fracture

- Mech., Vol. 5 (1973), pp. 365-377.
- [12] Atkinson, B.K., *Fracture Mechanics of Rock*, pp. 534, Academic Press, London UK, 1987. Chapter 1, 2, 4.
- [13] Anderson, T.L. *Fracture Mechanics; Fundamentals and Application*. (1995) CRC Press, Boca Raton
- [14] Gross, D., Seelig, T. *Fracture Mechanics; with an Introduction to Micromechanics*, 2006 Springer Berlin-Heidelberg.
- [15] Sester, M., Schmitt, W., Zhi Sun, D. Development and application of micromechanical material models for ductile fracture and creep damage, *International Journal of Fracture* 86: 75–90, 1997. *Kluwer Academic Publishers*.
- [16] A. Barata da Rocha, P. Teixeira, A.D. Santos, F.M. Andrade Pires, J.M.A. César de Sá, Sheet Metal Formability Evolution using continuous Damage Mechanics, *Int J Mater Form* (2009) Vol. 2 Suppl 1:463–466, Springer
- [17] Wilkins ML, Streit RD, Reaugh JE. Cumulative-strain-damage model of ductile fracture: simulation and prediction of engineering fracture tests. Tech rep UCRL-53058. Lawrence Livermore Laboratory, University of California, Livermore, CA 94550; 1983.
- [18] T. Wierzbicki, X. Teng, Evaluation of six fracture models in high velocity perforation, *Engineering Fracture Mechanics* 73 (2006), pp. 1653–1678
- [19] Zienkiewicz O.C., Taylor R.L., *The finite element method for solid and structural mechanics*, 6-th edition, Butterworth-Heinemann, 2005
- [20] ARAMIS <http://www.gom.com/3d-software/aramis-software.html>
- [21] CATIA V5TM <http://www.3ds.com/products/catia>

- [22] PAMCRASH™, *ESI Software Virtual Performance Solutions*, solver notes 2009
- [23] Dieter, George E. 1988, *Mechanical Metallurgy*. McGraw-Hill Book Company (UK) Ltd

Appendix 1

Figure A1.1 is true stress-strain curve that has been developed using data recorded during optical strain measurement test for parallel coupon. Special MATLAB code has been used to process the scattered data.

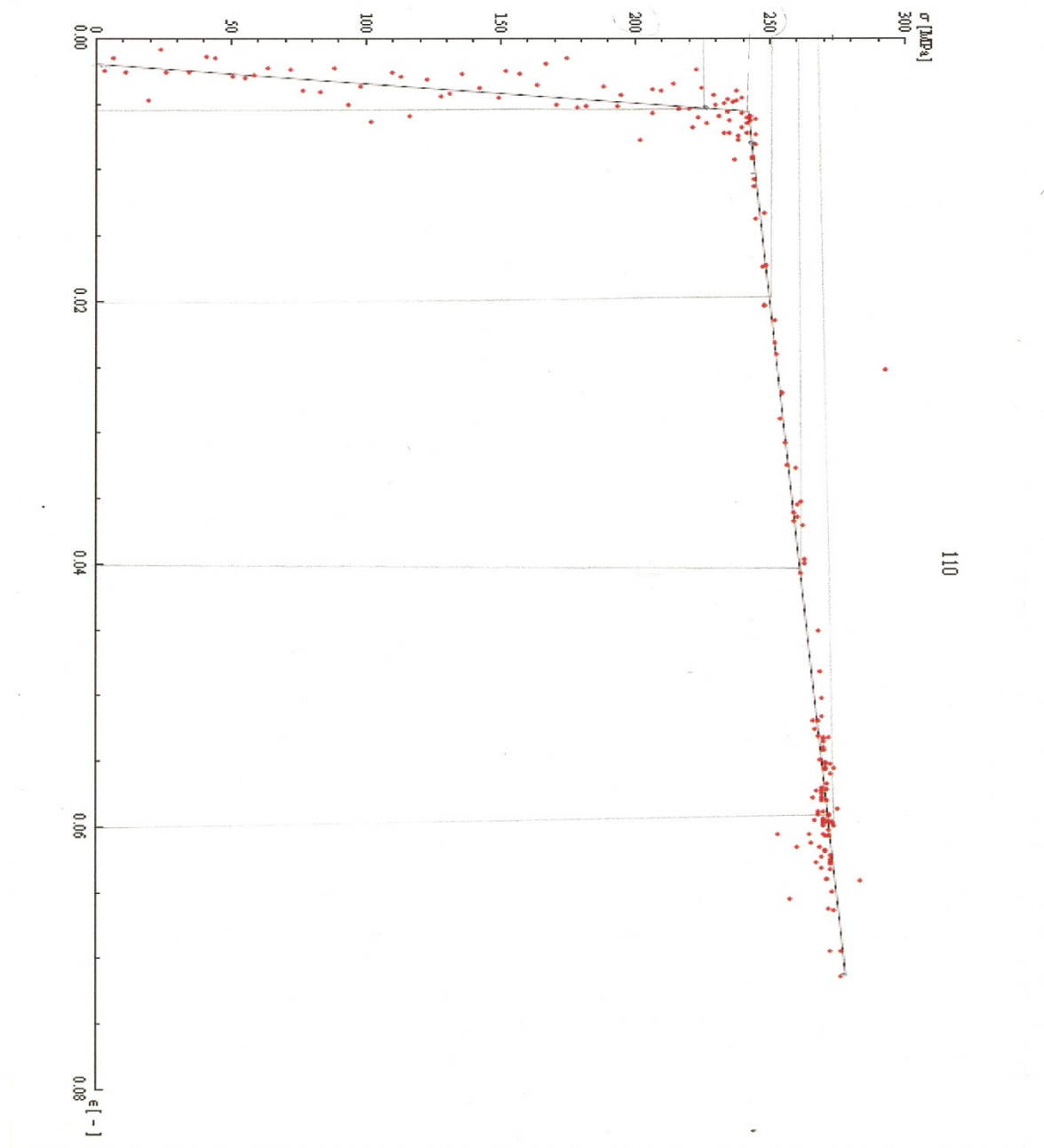


Figure A1.0.1: True stress-strain curve

Appendix 2

Complete material card of half solid and half shell element material model.

```

$#          IDPRT  ATYPE   IMAT  VA_MAT   TMAT
PART /          2   SOLID     3      0      0

$#  TITLE
NAME PART 4mm Dia U-notch

$#  DTELIM   TSCALF

$#  TCONT    EPSINI

$#RT1        XDIR1    YDIR1    ZDIR1
          1.0        .0        .0

$#RT2        XDIR2    YDIR2    ZDIR2
          .0        .0        1.0

$#
END_PART

$#          IDMAT  MATYP          RHO  ISINT  ISHG  ISTRAT  IFROZ
MATER /          3    16      2.753E-006    0    0

$#  BLANK AUXVAR1 AUXVAR2          QVM THERMAL  IDMPD
          0    0          1.    0

$#  TITLE
NAME Solid material

$#          G  SIGMA_Y    Et    ALPHA  BLANK  BLANK  STRAT1  STRAT2
          26.54CURVE          0.          2          0.    0.

$#          K
          57.5          1  1.00368  1.00438  1.    1.    1.004024  8.

$#          LC1    LC2    LC3    LC4    LC5    LC6    LC7    LC8
          2    0    0    0    0    0    0    0

$#EPSLNMAX  EPSLNi  EPSLN1    d1  EPSLNU    du  ZHI    fO
          0.18    0.    0.    0.    0.    0.    0.1    0.

$#  STRAT3  STRAT4  STRAT5  STRAT6    Q1    Q2    Q3  PFRAC

```



```

0.      0.      0.      0.      0.      0.      0.
$akp Rupture model
RUPMO /      1      6
NAME Rupture model EWK
      0.3      2.0      0.48      1.1      0.75      0.34
$# TITLE
NAME True stress-strain
$#
      X      Y
      0.      0.24
      0.02      0.258
      0.04      0.27
      0.06      0.281
      0.083      0.289
      0.3      0.34

$#      IDMAT      MATYP      RHO      ISINT      ISHG      ISTRAT      IFROZ
MATER /      1      109      2.753E-006      0      1
$# BLANK AUXVAR1 AUXVAR2 AUXVAR3 AUXVAR4 AUXVAR5 AUXVAR6      QVM THERMAL      IDMPD
      0      0      0      0      0      0      0      1.      0
$# TITLE
NAME TL116-C24 Aluminium Strangpresslegierung Barlat Plastizitaet
$#      E      SIGMA_Y      NUE      PLA_FLAG      HGM      HGW      HGQ      As
      69.CURVE      0.3      2      0.01      0.01      0.01      0.833333
$#      LC1      LC2      LC3      LC4      LC5      LC6      LC7      LC8
      8394105      8394106      8394107      8394108      0      0      0      0
$#      EPSLN1      EPSLN2      EPSLN3      EPSLN4      EPSLN5      EPSLN6      EPSLN7      EPSLN8
      0.      0.001      0.02      0.25      0.      0.      0.      0.
$#PSLNpMAX      STRAT1      STRAT2      RELIM      BLANK      EPREF
      0.      0.      0.
$#      STRAT3      STRAT4      STRAT5      STRAT6      BLANK      ZHI      FO
      0.      0.      0.      0.      0.1      0.
$#      a      b      c      f      g      h      m      BLANK
      1.00368      1.00434      1.00402      1.      1.      1.004024      8.
$#ANKSubKW      ICUR

```

```
CURVE      8394109
$$$$$$$$$$$$$$$$$$$$$$$$$$$$$$$$
$#          IDPRT   ATYPE   IMAT  VA_MAT
PART /           3     TIED     2      0
$#TITLE
NAME Tied solid-shell elements
$#  DTELIM
$#  TCONT   EPSINI
$#  RDIST   BLANK   INEXT
      1.5
$#
END_PART
```